Doctoral Dissertation
Doctoral Program in Metrology (32nd cycle)

Realization of an off-grid wireless sensor through vibrational energy harvesting

Stefano Palumbo

* * * * * *

Supervisors
Dr. Zucca Mauro, (INRiM), Supervisor
Dr. Pellegrini Vittorio, (IIT), Supervisor

Doctoral Examination Committee:
Prof. Davino Daniele, Referee, Università degli Studi del Sannio
Prof. Visone Ciro, Referee, Università degli Studi di Napoli Federico II
Prof. Ragusa Carlo Stefano, Politecnico di Torino
Prof. Gerbaldi Claudio, Politecnico di Torino
Prof. Laudani Antonino, Università degli Studi Roma Tre

Politecnico di Torino
April 17, 2020

I hereby declare that, the contents and organisation of this dissertation constitute my own original work and does not compromise in any way the rights of third parties, including those relating to the security of personal data.

. . . .
Stefano Palumbo
Turin, April 17, 2020

Summary

Recent technological advances in Micro Electro Mechanical system (MEMS), wireless communications and digital electronics have allowed the development of multifunctional, low-power appliances with a lower cost and able to communicate with each other by means of wireless technology with limited radius. These small devices, called sensor knots or mote, are made up of components able to detect physical quantities (position sensors, temperature, humidity, etc.), to process data and to communicate with each other.

To make these systems autonomous, where the power grid is not available, a power supply is needed. Commercial batteries can be a quick and easy solution but require at least an annual maintenance. The resultant periodic replacement makes such systems less autonomous and the maintenance is a cost and sometimes a problem. To overcome this restriction, it is necessary to find elsewhere an energy source capable to supply the sensor continuously for a longer period. Energy Harvesters (EHs) respond perfectly to this request since they do not need human intervention, having a lifespan of 10 or 20 years, and are environmentally friendly. These devices exploit sources generally wasted, such as mechanical vibration and heat, to generate low-power electrical energy. Theoretically, a small energy harvester having a 100μW rated performance and a 20-year lifetime (for an overall energy of 63kJ) can substitute over 50 CR2032 button cells. But this statement is true only if the harvested energy is stable and continuous all over the period. Since this condition could represent a too high constraint, in the design of the device not only the realisation of the best performance harvester but also of the coupled energy storage unit should be taken into account. Indeed, EHs require supercapacitors or rechargeable batteries having long life and small losses, to be coupled with the generator. Therefore, an EH device has a dual nature.

If on one hand the specific energy density harvested represents the peak of work, the storage element is a crucial component capable to modify the overall performance and which limit the working condition. The aim of this research is twofold. At one side, the activity is devoted to the development of a fully characterized Fe-Ga rod vibrational energy harvester. The goal of this study is to fully understand the interactions and respective influences on the overall performance of several parameters (such as mechanical and magnetic bias, stress applied and load resistance) in

order to evaluate the best working condition for a given energy source and then increase it through the design of a properly mechanical yoke for the Fe-Ga rod.
On the other side, great efforts are focused on the analysis of the interaction between graphene and silicon as anode materials for the design and realization of new and improved li-ion batteries (LIBs). The goal is to obtain a long life, high-rate and high-capacity LIB through a scalable, low cost and low time-consuming process.
At the end, a complete EH device with a Bluetooth Low Energy (BLE) sensor is assembled and tested in laboratory to demonstrate the applicability of the results obtained. The activity has been carried out among three locations: IIT Labs in Genova, Politecnico di Torino Labs and INRiM Labs in Torino.

Contents

List of Tables

List of Figures

Chapter 1

Introduction to energy harvesting

1.1 Autonomous wireless sensor

It is stated [1] that every year the information available on the net experienced an annual growth of 50 percent or more., and these are not just stream data, but entirely new ones. The information, collected from environment, buildings, vehicles, equipment, etc., enables the interaction with the surroundings and let to forecast failures as well as better understand some phenomena. The sectors involved in this revolution are the most diverse, and just as an example it is possible to list automotive, aerospace, industry, housing.

This remarkable increase of data has gone hand in hand with the progress in electronic and informatic fields, with attention to the data management. The main contribution comes from micro-electro-mechanical system (MEMS) technologies. To better understand the technological revolution in place, a practical example could be the automotive sector. Only 30 years ago the automobiles components were principally mechanical, and the sensors available to the user were limited, if not totally absent in the main basic car models. But as years go by, and with an introduction increasingly pervasive of the electronics inside the vehicles, it was possible for the user to have access to information about the fuel consuming and actual level in the tank, the closure of the doors or alert regarding the lights, up to nowadays when it is possible to know the number of the passengers, and the consequent alert for the seat belts. Today there are sensors that help during the parking, with systems able to park totally automatically, and are able to monitor the driver vigilance level.

Wiring and power supply of the sensors in a vehicle or system may not be easy, especially if one thinks of rotating parts or, in general, moving parts, such as the vehicle wheels. A simple example is the tire pressure monitoring by sensors in a car. These sensors are placed inside the tire (between the rim and the tyre) and monitor constantly the relative pressure, but their placement makes complex both their power supply and wiring. Since these sensors do not require high level of energy, a first solution could be the use of button batteries. But if on one hand this solution resolves the wiring problems, it also requests a periodical maintenance like the replacement of the battery. Battery replacement become a huge burden in large factories monitoring, where the deployment of hundred or even thousands of sensors could be required.

For the above stated reasons, it is necessary find alternative power sources able to guarantee the same power level of a battery but without the periodical maintenance, making totally autonomous the sensors. Ambient energy could be seen as a green and theoretically unlimited source, and energy harvesters (EHs) could be the perfect solution to overcome these issues. These systems are able to generate electric energy using untapped sources, like environment vibrations, light and heat from the sun, or reusing heat from the exhaust [2]. This thesis work will focus on the mechanical vibrations of the environment, but regardless of the environmental energy source, an EH system is briefly constituted by several parts, as shown in Figure 1.1.

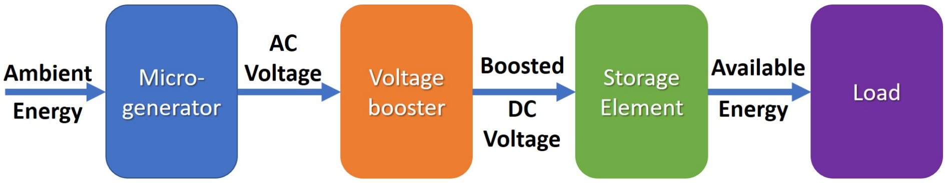

Figure 1.1: Scheme of a generic EH device: the micro-generator harvests the ambient energy, which is converted and boosted by a voltage booster and then is used to supply a load

When the EH generates an AC voltage, the latter must be rectified in order to supply a storage element. During this process, it is also possible to boost the voltage using a printed circuit or a voltage multiplier. Since the ambient energy cannot be continuous considering large periods of time, a storage element, generally a rechargeable battery or a supercapacitor, must be included. At the end, there is a load, which usually is not simply a passive load, but can be a smart system. For sake of example, when the goal is to supply a sensor, the above scheme could be completed with a little more load, as described in Figure 1.2.

In this case, the EH still produce an alternative voltage that must be rectified in order to be properly stored. The load is now represented by a sensor, a microcontroller and a transceiver. The energy storage unit must be properly designed in order to supply all these elements considering the operating cycle of the EH.

In literature it is possible to find numerous papers dealing with the working principle, design and efficiency of the harvester (generator) component [3], but very few papers like [4] show a comprehensive analysis of a complete and working device.

The aim of this thesis work is the realisation of an autonomous wireless sensor suitable to supply a Bluetooth Low Energy (BLE) sensor. The goal is obtained

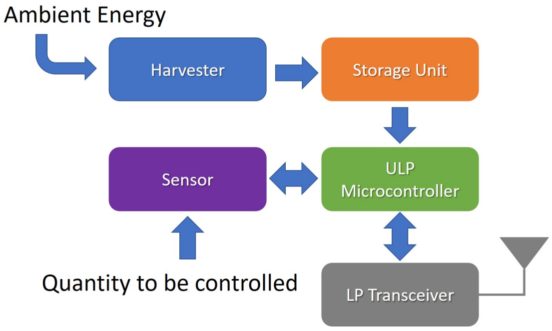

Figure 1.2: Scheme of a sensor supplied by an EH. In this case, the EH supply the sensor through the ULP Microcontroller.

focusing the attention both on the energy producer unit (the mechanical EH) as on the energy storage unit that is a rechargeable Li-ion battery.

1.2 Energy Producer Unit

Due to the wide variety of suitable ambient energy, the use of the EHs spans from industrial to biomedical application. However, the ambient energy sources can be briefly subdivided into four main types:

- mechanical
- thermal
- radiant
- biochemical

The design of an EH strictly depends on the available energy source and, at the same time, the relative power density may sensibly vary not only among different type of energy source, but also among the same type of energy source, as well represented in Figure 1.3.

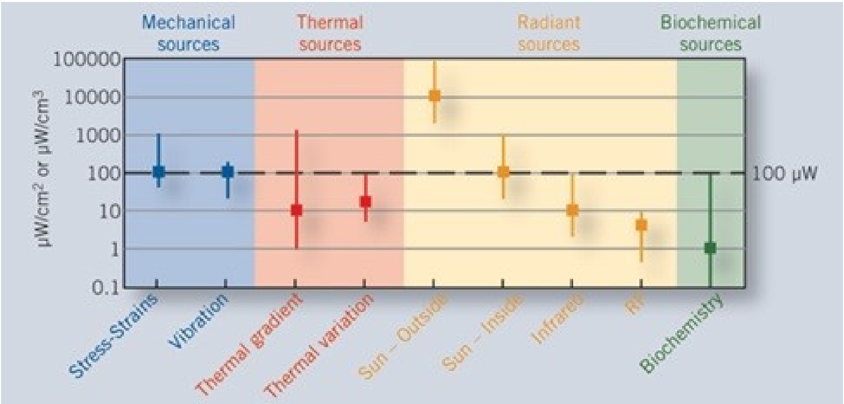

Figure 1.3: A comparison of ambient energy source (before conversion) shows each has a different power density. Thus, the source of energy to be harvested must be chosen to the local environment [5]

Easy to see, the most powerful source is the radiant energy from the sun. The inconvenience of this source is that in dark areas, such as inside or just near a machine as in a warehouse, the energy harvested reduces of more than three order of magnitude. Therefore, excluding the sun, the mechanical ambient energy source shows the highest medium power among all the other ones.

Mechanical EHs principally use, as energy source, stress-strain phenomena and vibrations. Usually vibrations are undesirable effects of mechanical motion, and the general idea is to suppress those using damping features. Vibrations can be transformed into energy using properly EHs that can be also provide a damping effect [3, 6].

Vibrations may vary in amplitude and frequency. This means that the EH must be properly designed having in mind the exact ambient energy source. An interesting example of how the vibration may vary is presented in [7], where several vibration profiles have been analysed. In this work three different sources of vibration are considered:

- vibration on a car wheel (due to the presence of potholes)
- vibration on a bicycle (comparing both cobblestone and street case)
- a vibrating conveyor

The relative time series of these three different vibrations are measured with a three-axis accelerometers and reported in Figure 1.4.

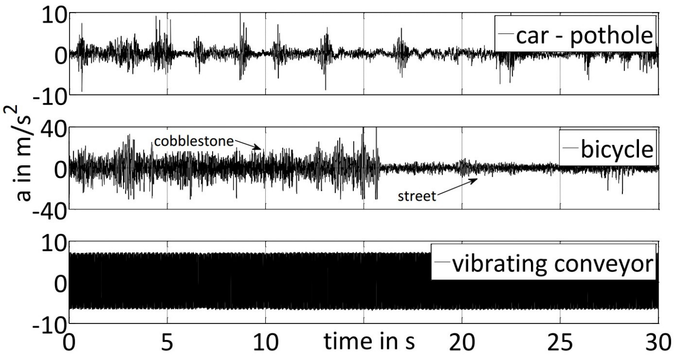

Figure 1.4: Time series of different mechanical vibrations presented in [7]

It is clear that the vibrations profile of vehicles may include unpredictable events (e.g. pothole) and strictly depend on the relative driving situation (type and condition of roads, traffic, etc.), while industrial machineries have much more periodic vibrational profile. In any case, vibrational effects represent an important source of mechanical power. Focusing the attention on the vibrational energy harvester (VEH), one can find three different types in literature [3]:

- piezoelectric
- electromagnetic
- electrostatic

To these, it has to been considered also magnetic / magnetostrictive EHs, which use mechanical stresses to generate current.
Each type of VEH has its own pros and cons, and a general comparison to magnetostrictive one is presented in Table 1.1.

Table 1.1: Summary of the comparison of the different vibrational types of harvesting mechanism. Data from [4]

Type	Advantages	Disadvantages
Piezoelectric	no external voltage source high voltages of 2-10 V compact configuration compatible with MEMS high coupling in single crystal	depolarization brittleness in bulk piezolayer poor coupling in piezo-film (PVDF) charge leakage high output impedance
Electromagnetic	no need of smart materials no external voltage source	bulky size: magnets and pick-up coil difficult to integrate with MEMS maximum voltage of 0.1 V
Electrostatic	no need of smart material compatible with MEMS voltages 2-10 V	external voltage (or charge) source mechanical constraints needed capacitive
Magnetostrictive	ultra-high coupling coefficient > 0.9 no depolarization problem high flexibility suited to high frequency vibration	nonlinear effect pick-up coil may need bias magnets difficult to integrate with MEMS

1.2.1 Vibrational Energy Harvesters

Piezoelectric VEHs A piezoelectric VEH is made of a piezo-electric material; there are two principal type of high-density material, PVDF piezoelectric polymer and PZN piezoelectric relaxer single crystal. Each material presents specific characteristics, however the synthesis of both in large volume still represents a challenge and is really expensive. Generally, they are produced as thin layer or plates, which need to be bonded to a long cantilever, with a side fixed and another one free to vibrate due to an external mechanical excitation, as shown in Figure 1.5.

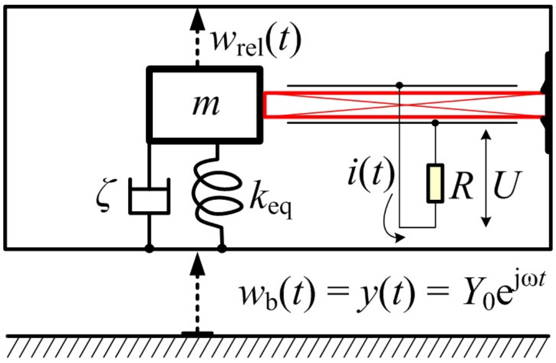

Figure 1.5: Scheme of a piezo-electric VEH.

The optimal power is obtained when the VEH vibrates with its resonant frequency, that is dependent on the dimension and the mass of the cantilever. The resonant frequency can be obtained by:

$$f_n = \frac{\nu_n^2}{2\pi l^2} \cdot \sqrt{\frac{EIl}{m}} \tag{1.1}$$

Where f_n is the n-th mode of the resonant frequency, ν_n the relative eigenvalue, l is the length of the cantilever, E the elastic module, I the area moment of inertia, m the mass of the cantilever. In order to lower the resonant frequency, and to set it properly during the installation of the VEH, generally it is attached a proof mass at the tip of the cantilever.

Electromagnetic VEH An electromagnetic VEH is presented in Figure 1.6a [8]. A magnet able to move inside a coil under the influence of one of more fixed magnets at its ends constitutes the scheme of this type of VEH. The induced voltage is influenced, principally, by the frequency and the amplitude of vibrations (1.6b), the relative position between the coil (1.6c) and the moving magnet and the resistance of the coil (1.6d).
The induced voltage is determined by:

$$V = N \cdot \frac{d\Phi}{dt} = N \cdot \frac{d\Phi}{dz}\frac{dz}{dt} \tag{1.2}$$

Where Φ is the flux of the magnetic field.

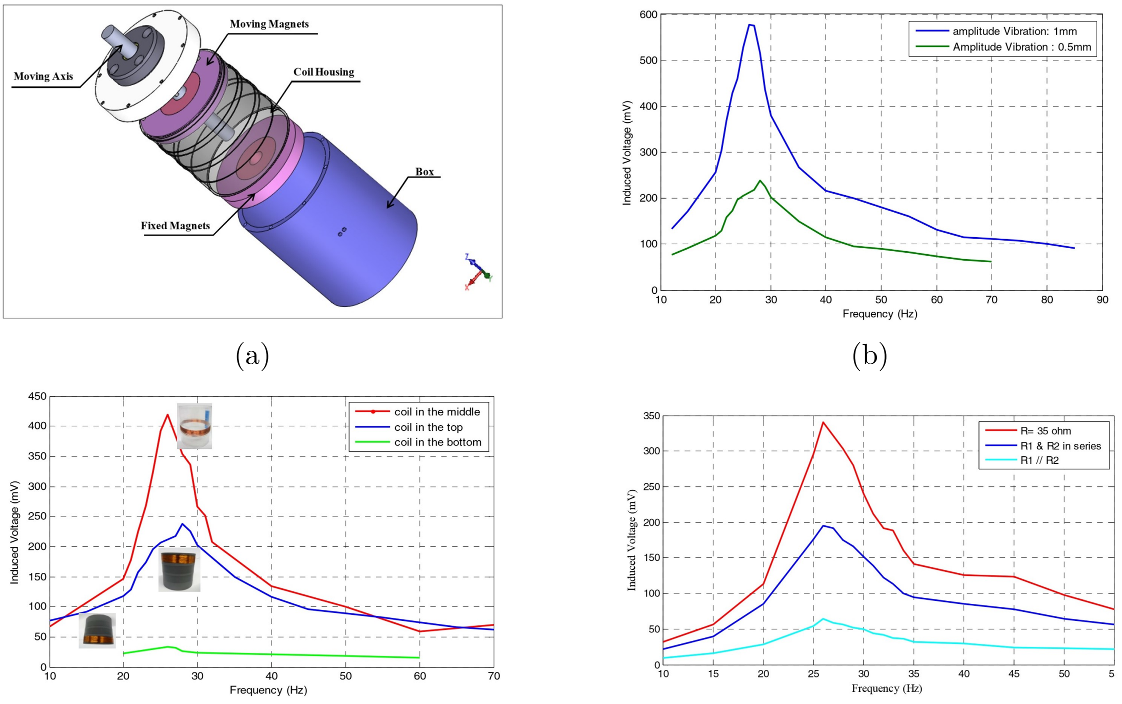

(a) (b)

(c) (d)

Figure 1.6: (a) Spare parts of an electromagnetic VEH. Results of the influence of the amplitude and frequency vibration (b), coil position (c) and use of multi-coil or single-coil (d) on the VEH performances. Images taken from [8].

Electrostatic VEHs It is possible to schematize an electrostatic VEH into a capacitor constituted by two electrodes, one fixed and one mobile, like in Figure 1.7.

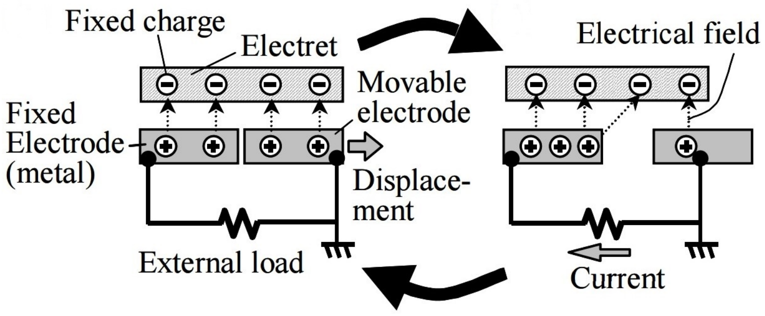

Figure 1.7: Scheme of an electrostatic VEH [9]

The fixed charges induce counterparts in the fixed electrode. With a displacement of the movable electrode, and due to the re-arranging of the charges following the Gauss's law, the charges are transferred between the fixed electrodes generating a current. The voltage inside the VEH is given by:

$$V = \frac{Qd}{\varepsilon_0 A} \tag{1.3}$$

Where Q is the charge, d is the distance between the two electrodes, ε_0 the permittivity of free space and A is the area of the electrodes. This type of generators can be designed as voltage - or charge - constrained [9]. The first ones present a constant voltage applied to the plates, so the variation of the charges depends on the changing capacitance. A typical operating cycle starts with a maximum capacitance condition, where the capacitor is charged up to a reference voltage while the capacitance is constant. Maintaining constant the voltage with a reservoir, when the plates move apart the capacitance decrease, and the excess charge flows back to the reservoir with a net energy gain of:

$$E = \frac{1}{2}\left(C_m - C_i\right) V_m^2 \tag{1.4}$$

where C_m and C_i are respectively the maximum and the instant capacitance, while V_m is the reference voltage.
The second type works with a constant charge on the electrodes, so it is the voltage that vary with the capacitance. The initial condition is the one with the maximum value of the capacitance. Decreasing the capacitance and maintaining constant the charge, the voltage increases. A reservoir should give the initial charging, where the charge returns at the end of the cycle. The net energy gained is given by:

$$E = \frac{1}{2}\left(C_m - C_i\right) V_i V_0 \tag{1.5}$$

where V_i and V_0 are respectively the instant and the reference voltage.
Obviously, it is necessary to choose carefully the voltage with respect to the circuit that have to be supplied. This means that the voltage should be regulated case by case. A constant voltage approach, if on one hand provides high energy level, on the other hand requires a control system to modify the voltage level. The charge constrained device, otherwise, even if produces less energy it is simpler to regulate since the voltage level refers to the pre-charge of the electrodes. It also exists a third possibility, which starts from a charge-constrained mode but using a fixed capacitance in parallel. In this way, it is possible to reach the same energy level of the voltage-constrained mode but maintaining a simpler regulation of the voltage level. The drawback is represented by a higher initial charge to operate.
The electrostatic VEH are useful when it is necessary to work with self-powered microsystem, such as human-based devices. *Roundy et al.* [10] list three different

geometry in which it is possible to configure an electrostatic VEH, as shown in Figure 1.8a, Figure 1.8b and Figure 1.8c.
The dark areas are fixed, for example to the substrate, while the lights areas are free to oscillate. In the first geometry, modification of the overlap areas of the finger leads to changes in the capacitance, while in the second one is the gap between fingers that is free to change. In the last geometry, the capacitance changes with changing in the gap between two large plates.

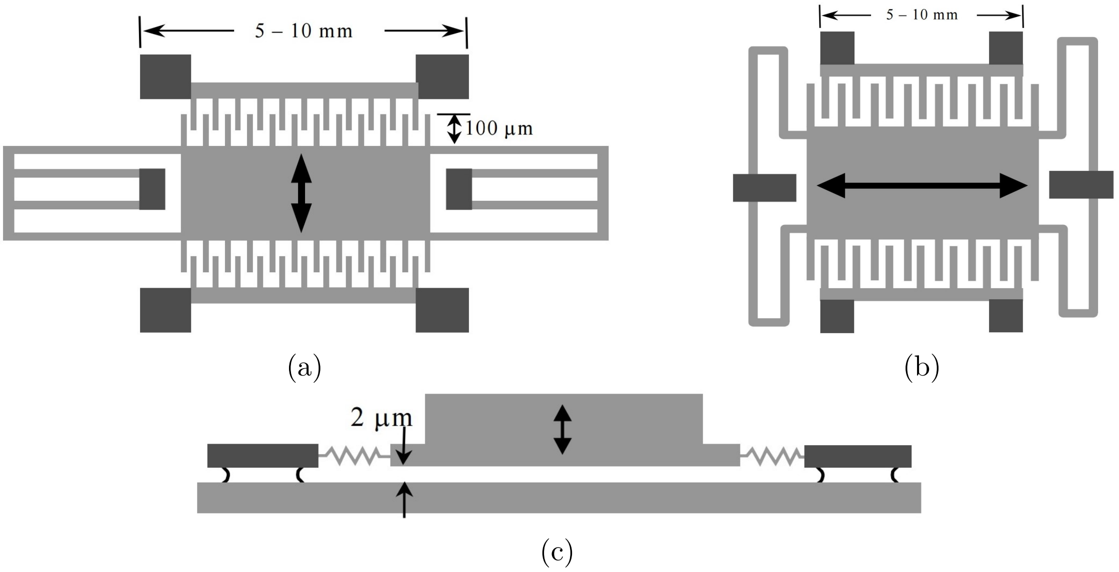

Figure 1.8: Possible configurations of an electrostatic VEH: (a) in-plane overlap geometry, (b) in-plane gap closing geometry and (c) out-of-plane gap closing geometry. Images taken from [10].

1.2.2 Giant Magnetostrictive Materials

Piezoelectric, electrostatic and electromagnetic are the most common type of VEHs.
Electromagnetic devices are the most common EH's in the market, while piezoelectric systems are the most common in smart applications due to their high compatibility with MEMS and its compact configuration. Nevertheless, as seen in Table 1.1, piezoelectric VEHs have also not negligible limitations, e.g. break due to fatigue, charge leakage, high output impedance.
Magnetostrictive materials (MsM) have been studied [12, 13, 14] to overcome these problems.
In a schematic way, as shown in Figure 1.9, the mechanical energy (i.e. vibrations) harvested from the ambient source is first transferred in the magnetostrictive material.

Table 1.2: Summary of magnetostrictive effects. Data from [11].

Direct effects	Inverse effects
Joule effect Change in sample dimensions in the direction of the applied field	*Villari effect* Change in magnetization due to applied stress
ΔE effect Magnetoelastic contribution to magnetocrystalline anisotropy	*Matteucci effect* Helical anisotropy and emf induced by a torque
Wiedemann effect Torque induced by helical anisotropy	Magnetically induced changes in the elasticity
Barret effect Volume change due to magnetization	*Nagaoka-Honda effect* Change in the magnetic state due to a change in the volume

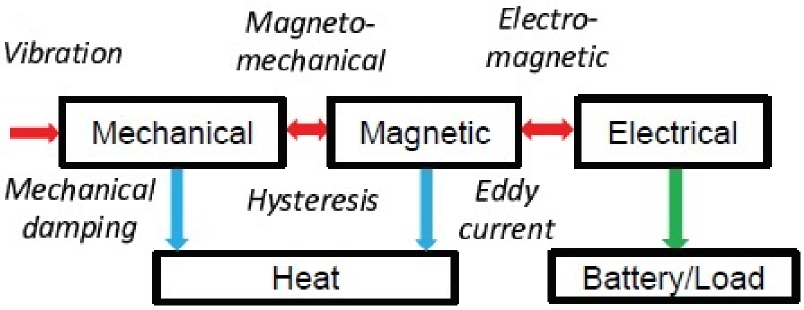

Figure 1.9: Scheme of the energy flowing within a vibration harvester. Taken from [6].

Exploiting the Villari effect, the variation of the magnetic energy induced by the vibration is converted into electrical energy to the electrical circuits.
Villari effect is an inverse effect corresponding to a change of magnetization induced by stress in magnetostrictive materials. These materials are subjected to other effects. The direct effect is a change in the material dimensions induced by the magnetization of the material. This is also known as Joule effect, or direct effect, and is exploited in the magnetostrictive actuators.
Other effects, which are inherent to the characteristics of all ferromagnetic materials and magnetostrictive materials in particular, are well detailed in the work of *Viktor Berbyuk* [11] and are summarised in Table 1.2.
More in detail, the vibration result in a time dependent change of the material magnetic state and, in a second step, a time variation of a magnetic flux inside a

coil generates a current.

A change in the magnetic state because of a deformation is referred as the Villari effect. The general scheme of the effect is presented in Figure 1.10.

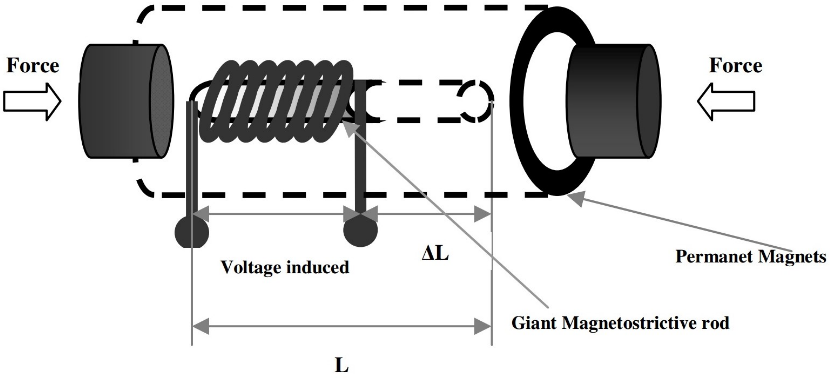

Figure 1.10: Schematic of the Villari effect. Image taken from [11].

The Stoner-Wohlfarth (SW) approximation [15] can be usefull to better understand the magneto-mechanical coupling. Here, the magnetostrictive material is described as a collection of non-interacting magnetic domains, as shown in Figure 1.11.

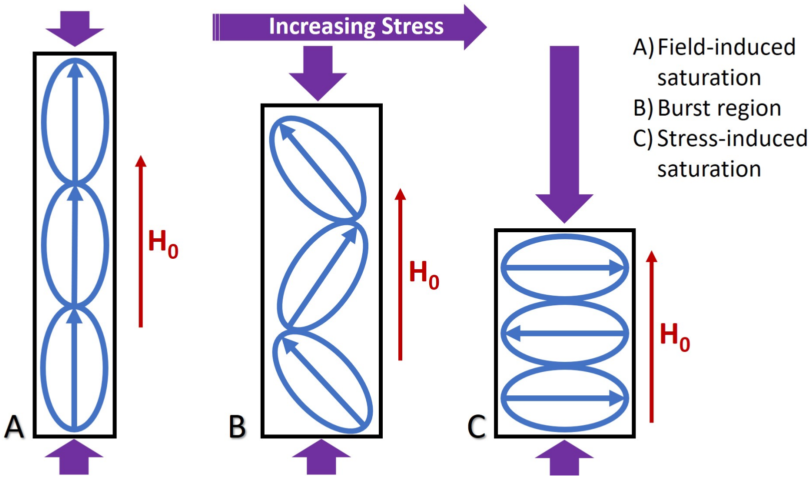

Figure 1.11: Magnetic domain rotation in magnetostrictive materials. Image taken from [6].

In this representation, each magnetic domain has its own uniformal local magnetization M_s, and the weighed sum of all the domains gives the bulk magnetization. As schematically shown in Figure 1.11, the applied stress results in a re-orientation of the local domains, which are dependant from the bias magnetic field H_0. Figure 1.11 (right) represents a zero bulk magnetization scenario. Here, the stress is dominant over the bias magnetic field, and the local domains result perpendicular to it. On the other side, represented in Figure 1.11 (left), the stress is null, the local domains are able to orient in parallel respect H_0 and the bulk magnetization reaches its maximum. This representation suggests that a periodical variation of the mechanical compression, resulting by the vibration sources, generates a time-variation of the bulk magnetization due to the continous re-orientation of the local domains. Moreover, the maximum magneto-mechanical coupling effect is obtained with a 90-degree rotation of the local domains. This condition can be reached balancing the mechanical energy with an appropriate bias magnetic field H_0, which is usually generated by permanent magnets.

In presence of small coaxial stress and magnetic field, the nonlinear magneto-mechanical coupling effect is usually represented by the following linear equations:

$$\Delta B = d\Delta T + \mu^H \Delta H \tag{1.6}$$

$$\Delta S = s^H \Delta T + d\Delta H \tag{1.7}$$

where d is the piezomagnetic constant, s^H is the elastic compliance, μ^H is the magnetic permeability, H is the magnetic field, T is the stress applied, B is the flux density and S the strain along the input direction. The symbol Δ indicates a variation of the relative parameter.

Once obtained a time variation of the bulk magnetization, it is possible to achieve the electromagnetic coupling simply installing a pickup coil around the magnetostrictive materials. From the Faraday's law, voltage is always generated in relation of a magnetic flux density change inside a coil:

$$V = -N_c A_c \frac{\partial B}{\partial t} = -d N_c A_c \frac{\partial T}{\partial t} \tag{1.8}$$

where A_c is the coil's cross section and N_c is the total number of turns.

If the time behavior of the force variation is periodic also the electromotive force (emf) or voltage V is time periodic. To charge the battery it is necessary an AC-DC converter or custom designed battery charging circuits.

All ferromagnetic materials are subjected to Villari Effect, but for most of them the magnitude of the magnetization change with mechanical stress is not suitable for energy harvesting. Specific alloys, called giant magnetostrictive materials (MsM) are suitable for EH, such as crystalline Terfenol-D ($Tb_{0.3}Dy_{0.7}Fe_{1.9-2}$), galfenol ($Fe_{1-x}Ga_x$), and amorphous magnetic laminations like Metglas ($Fe_{81}B_{13.5}Si_{3.5}C_2$). Direct force harvester represents the typical configuration, and a scheme is presented in Figure 1.12.

The harvester is represented by a rod surrounded by a pick-up coil and magnetic biased by permanent magnets. The permanent magnets may be placed either around, as in Figure 1.12 or in series (at the top and at the bottom) with the rod. In this configurations, all the driver elements are longitudinal, since the x_3 direction is usually oriented along the cylindrical axis.

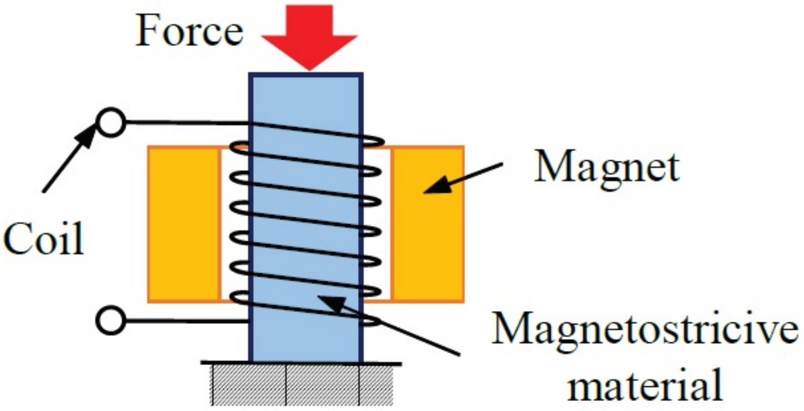

Figure 1.12: Configuration of axial-type magnetostrictive energy harvesters [11]

Therefore, the magnetostriction coefficients can be described as follow.
The piezomagnetic constant (defined at constant stress or constant field):

$$d_{33} = \left(\frac{\partial S_3}{\partial H_3}\right)_T = \left(\frac{\partial B_3}{\partial T_3}\right)_H; \tag{1.9}$$

the permeability at constant stress:

$$\mu_{33}^T = \left(\frac{\partial B_3}{\partial H_3}\right)_T; \tag{1.10}$$

the elastic compliance coefficient at constant field:

$$s_{33}^H = \left(\frac{\partial S_3}{\partial T_3}\right)_H; \tag{1.11}$$

and finally, the coupling factor:

$$k_{33} = \frac{d_3 3}{\sqrt{s_{33}^H \mu_{33}^T}}; \tag{1.12}$$

where the subscript indicate that the stress (T) or the magnetic field strength (H) are held constant. In this conformation, S_3 and T_3 (Pa) represent respectively the strain and the stress along the direction x_3, while H_3 (A/m) and B_3 are the respectively the magnetic field strength and the magnetic flux density component on x_3.
The thermodynamic meaning [9] of the magnetostrictive coefficients can be found in Appendix A.

1.2.3 Terfenol-D

Terfenol-D is the first and the main used giant magnetostrictive materials both as actuator and as energy harvester. In the late 1970's the Naval Ordnance Laboratory (NOL), now Naval Surface Warfare Center – Carderock Division, first developed Terfenol-D for marine sonar application. Terfenol-D is an alloy made of Terbium (TER) and Iron (FE), with the addition of Dysposium (-D) used to increase the magnetostrictive response of the material with lower magnetic field bias. The name is just the acronym of the material implied (TER+FE), the discovering organization (NOL) and the later element added (-D).
The main physical properties are reported in Table 1.3.
Among its properties, it is possible to find the reason of the success of Terfenol-D. At room temperature, it shows the largest magnetostriction among any known ferromagnetic material and alloy. Used as an actuator, Terfenol-D shows a magnetostriction capable to generate a strain from 4 to 100 times greater than any other magnetostrictive materials, and 2-5 times respect traditional piezoceramics. Due to its high Curie temperature (380°C), magnetostrictive performance increase over 1000 ppm from room temperature up to 200 °C and modifying the alloy composition it is possible to obtain the same results also down to cryogenic temperatures. The drawbacks of this material are principally its poor ductility, low fracture resistance and the impossibility to machine it.
Terfenol-D is a well-known magnetostrictive material widely analysed in several papers, which covered both theoretical [16] as experimental [17, 18, 19, 20, 21, 22, 23, 24] investigations. Some papers deal with modelling of magnetostrictive material properties [25, 26, 27, 28, 29, 30] while others have investigated the use of such alloy in actuators [31] and for energy harvesting (EH) devices [32, 33, 34].

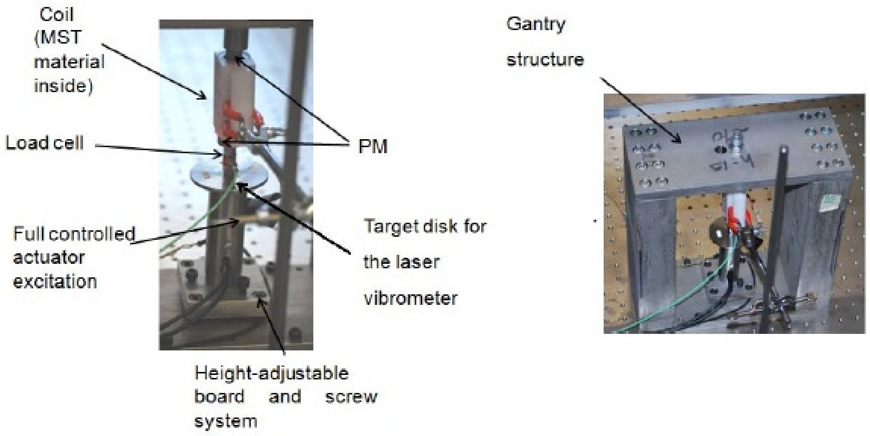

Figure 1.13: Detail and full view of the transducer and experimental setup used in [35].

Table 1.3: Terfenol-D Physical Properties.

Standard Composition	$Tb_{0.3}Dy_{0.7}Fe_{1.92}$
Mechanical Properties	
Density	9200 – 9300 kg/m^3
Young's Modulus at constant I	18 – 55 GPa
Young's Modulus at constant V	50 – 90 GPa
Bulk Modulus	90 GPa
Speed of Sound	1395 – 2444 m/s
Tensile Strength	28 – 40 MPa
Compressive Strength	300 – 880 MPa
Vicker's Hardness	650 HV
Minimum Laminate Thickness	1 mm
Thermal Properties	
CTE	11 ppm/°C @ 25 °C
Specific Heat	0.33 kJ(kg – K)
Thermal Conductivity	13.5 W/(m – K) @ 25 °C
Melting Point	1240 °C
Electrical Properties	
Resistivity	$60 \times 10^{-8} \Omega m$
Curie Temperature	380 °C
Magnetostrictive Properties	
Strain (estimated linear)	800 – 1200 ppm
Energy Density	4.9 – 25 kJ/m^3
Piezomagnetic Constant, d_{33}	6 – 10 nm/A
Magnetomechanical Properties	
Coupling Factor	0.7 – 0.8
Magnetic Properties	
Relative Permeability	2 – 10
Saturation Flux Density	1 T

Focusing on the behaviour of Terfenol-D for energy harvesting applications, the paper [35]describes an experimental setup developed in the same laboratory where a part of this thesis work has been carried out. The mentioned setup was conceived for the analysis of the quantities affecting the magnetostrictive behaviour of a bulk rod of Terfenol-D included in an EH device (Figure 1.13).

The experimental setup consists of a non-magnetic frame, which embeds the mechanical excitation (piezoelectric actuator) and transducer (Terfenol-D rod with magnets at both ends). The transducer is also bounded by a coil and is excited by

a vibrating force able to impose a force sinusoidal profile in the frequency range up to 1 kHz.
In an energy harvesting configuration, many parameters capable to affects the harvester performance can be identified. At first, the stress applied with all its element, such as dynamic load, frequency and an eventually pre-load. Then the properties of the circuit, in particular the impedance of the pick-up coil and of the load. More difficult, the analysis on how the magnetic field bias affects the harvester due the limits in the experimental device in applying different value of the magnetic field bias by means of an external coil.

Frequency and Coupled Circuit Effect The time dependence of the magneto-mechanical coupling suggests that the vibration frequency of the mechanical stress may influence the output power and current values. Maintaining constant all the other parameters, such as preload, magnetic field bias and load resistance, in Figure 1.14 is shown the output power versus the frequency, considering four amplitudes of the time varying vibrational stress.

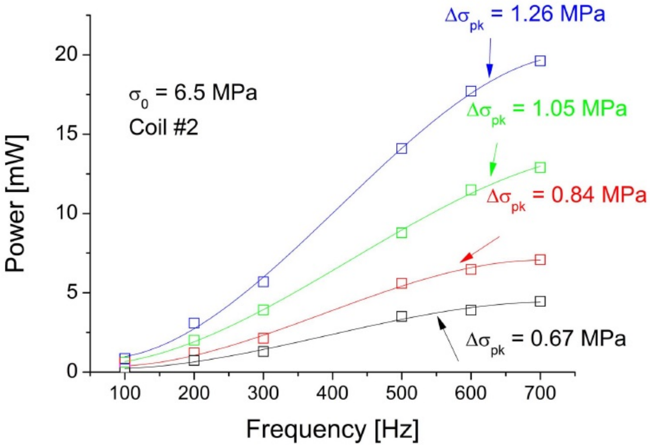

Figure 1.14: Effect of the vibration frequency on the measured electrical output power, at four different dynamic stress amplitudes, fixing the prestress at 6.5 MPa. Image taken from [35].

It can be seen that the output power increases with frequency and, due to the effects of eddy currents, tends to saturate at high frequencies.
Faraday Law 1.8 underline that the number of turns is directly related to the output voltage while it is well known that the impedance of the load circuit coupled to the harvester, which is also function of the number of turns and the section of the wire, modifies the harvester performances in terms of output power and voltage. Table 1.4 shows a comparison among 4 different pick-up coils applied to the same Terfenol-D rod at 300 Hz.

Table 1.4: Comparison on electrical and mechanical quantities. Preload 6 MPa, electrical resistive load 10 Ω. Data taken from [35].

Coil	Turn Number	P [mW]	I_{rms}	R_M [Ω]	Wire diam. [mm]
1	288	2.2	33.2	2.0	1.0
2	540	3.0	20.7	7.0	0.5
3	990	3.8	11.3	30.0	0.5
4	24300	4.2	0.53	15000	0.1

The power and current values reported in Table 1.4 are the maximum generated in the same conditions of mechanical stress and magnetic field bias. The only parameter modified is the resistive load $\mathrm{R_M}$, which was chosen to match the coil impedance. The output power versus the output current (or voltage) is a peak function when using as the driving parameter the load resistance. A family of such a curves can be obtained varying the mechanical bias or the excitation stress amplitude. To see more in detail this effect see Figure 1.15. In the figure, the values of the load resistance are reported as labels.

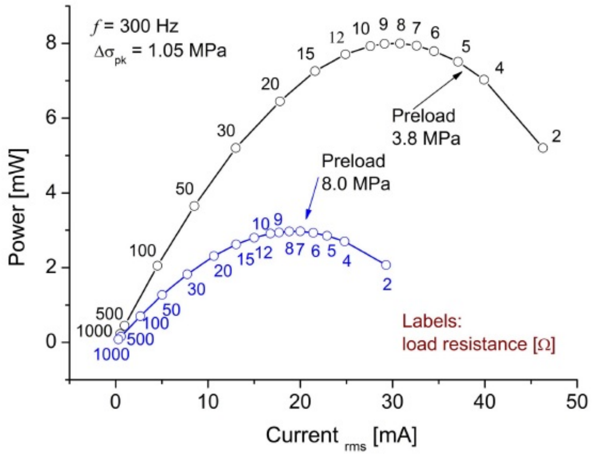

Figure 1.15: Effect of the mechanical prestress and load resistance on the measured electrical output power, at constant excitation force amplitude. Image taken from [35].

Preload Effect It has been demonstrated that in a Terfenol-D transducer the vibration stress magnitude and the mechanical bias have a combined effect. In Figure 1.16a is shown the variation of the output power varying the preload, for four different vibration stress amplitude.

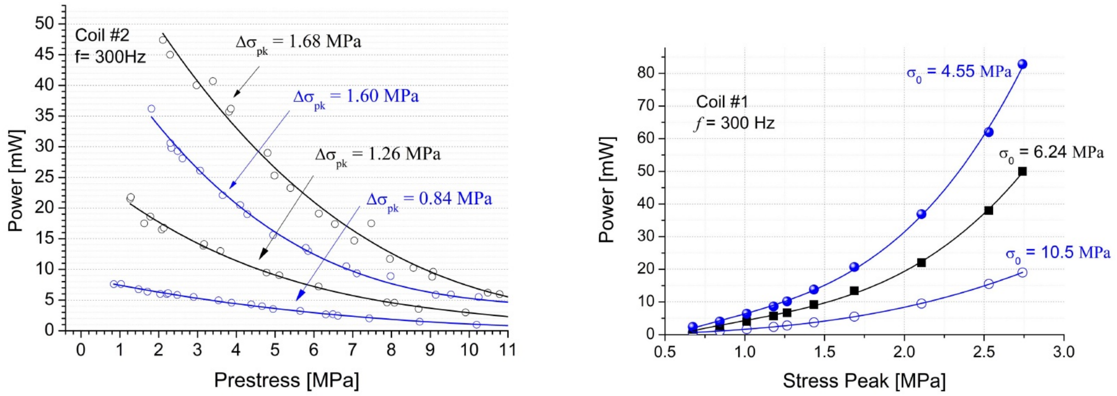

(a) (b)

Figure 1.16: (a) Curve family measured at 300 Hz. Output power versus the applied preload, measured for four different vibration stress amplitudes. Measured values are represented by circles. Solid lines interpolate the measured values. (b) Measured power versus the dynamic stress peak amplitude of the vibration, for three different preload values. Images taken from [35].

Indeed, it is well known that giant magnetostrictive materials need a suitable mechanical prestress in order to optimize their performance. Looking at the interpolating lines, it is clear that there is a match between the mechanical preload σ_0 and the dynamic stress $\Delta\sigma_{pk}$. In the case the test rig utilized in [35], the compression force that holds the rod constrained is that of preload. By applying a harmonic dynamic load, in a half-wave the mechanical stress is added to that of the preload. In the other half-wave, the mechanical stress is subtracted. Neglecting dynamic effects, when the dynamic stress is equal to the preload amplitude, in the second half-wave at the dynamic stress peak applied, the stress on the rod is subtracted from the prestress and then reduced to zero. Consequently, the rod is in an unstable situation because it is no longer bound. If the amplitude of the dynamic stress becomes progressively greater than the prestress, the instability condition lasts longer. On the contrary, if the dynamic stress is lower than the prestress the rod always undergoes a net compression and remains constantly constrained. For each curve presented in Figure 1.16a, the output power is maximized when the excitation force peak is close to the preload value. If we define the ratio r, that is the peak magnitude of the dynamic force, as:

$$r = \frac{\Delta\sigma_{pk}}{\sigma_0} \tag{1.13}$$

one may says that the maximum output power is obtained when $r \approx 1$, and decreases with r.

Figure 1.16b shows the results reciprocally, that is by maintaining constant the

preload and varying the amplitude of the vibration $\Delta\sigma_{pk}$. The effect on the output power is shown for three values of the mechanical preload σ_0.
Again, increasing the dynamic stress directly increase the output power. While, the higher values are obtained with the lower preload since it is closer to $\Delta\sigma_{pk}$.

Effect of the Magnetization Bias The SW approximation [15] shown in Figure 1.11 states that the rotation of the local magnetic domain depends both on the applied stress and the magnetic field bias, and that the maximum effect (i.e. a 90-degree rotation) would occur when the mechanical energy is properly balanced with an appropriate magnetic field bias. Focusing on the magnetic effect, the presence of a periodic external mechanical stress implies a periodic rotation of the local magnetic domains, resulting on a periodic variation of the bulk magnetization.

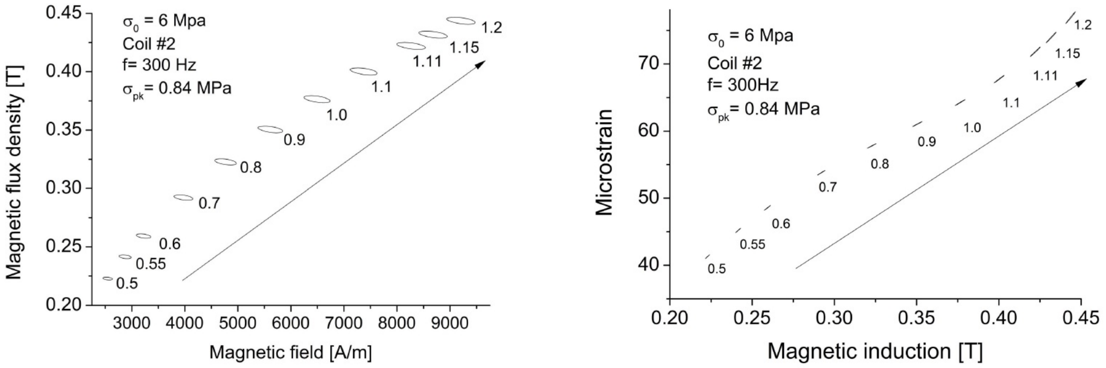

(a) (b)

Figure 1.17: (a) Vibration-induced hysteresis loops, calculated as a function of the remanence of the permanent magnet. Horizontal axis represents the total field applied to the magnetostrictive material. Each remanence value, expressed in tesla, is shown close to the corresponding cycle. (b) Vibration-induced magnetomechanical paths. Correspondent remanence of the PM, in tesla, is reported near each path. Images taken from [35].

Figure 1.17a shows the stress-induced hysteresis loops, obtained ranging only the remanence values of the permanent magnets, which determine H_0. As expected, the periodic values of the bulk magnetization results in loop on the graph. But over the form, it is important to analyse the width of the loops. Increasing the magnets remanence up to ~ 1 T, results in a loop area rises. Only after $H_0 > 1$ T the loop area remains nearly constant. This could mean that $H_0 = 1$ T is the ideal magnetic field bias for the set of mechanical force chosen ($\sigma_0 = 6$ MPa, $\quad \sigma_{pk} = 0{,}84$ MPa). The same phenomena could be seen from the strain point of view. Indeed, the strain and the magnetization are connected. The process is still the same: the vibration induce a strain on the sample, which force the re-orientation of the local magnetic

domains resulting in a magnetic flux density variation and then to the generation of an electromotive force (EMF). Unlike the loops shown in Figure 1.17a, the strain do not suffer of hysteresis, and the periodic values of the strain is linear, as represented in Figure 1.17b. Even in this case, the effects of the vibration increase for higher values of magnetic remanence up to ∼ 1 T, then remains nearly constant.
At the end, it could be interesting to analyse how the magnetic field bias effects directly the output performance, for example the output current, as shown in Figure 1.18.
In this diagram, the maximum output current is obtained for the highest value of the magnetic remanence (1,2 T). As already evidenced in [36, 37], the reaches of an optimum magnetic bias guarantees the highest production of current and power

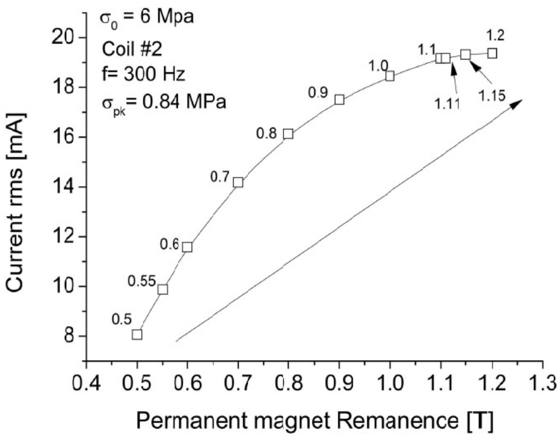

Figure 1.18: Electrical current produced by the harvester as a function of the remanence of the PMs. Remanence of the PM, expressed in tesla, is reported near each simulated point. Image taken from [35].

1.2.4 Fe-Ga alloy

In the last decade, took on more and more importance the use of magnetostrictive materials for energy harvesting applications. And, for this purpose, iron-gallium alloy demonstrates to be an interesting alternative to Terfenol-D. Galfenol, in materials science, is the general term for an alloy of iron and gallium. It is a single-phase solid obtained with a disordered substitution of single crystal iron with gallium atom, as a result of the investigation of gallium substitution in iron carried on by *Clark et al.* [38]. In Figure 1.19 is depicted a body centred cubic (BCC) a-Fe structure, where the ”a”-prefix indicates a randomly substitution with a gallium atom throughout the lattice. United States Navy (nol) researchers discovered that adding gallium to iron could amplify iron's magnetostrictive effect up to tenfold. In magnetostrictive applications, galfenol is usually recognized as the composition $\mathrm{Fe100}-_{\mathrm{x}}\mathrm{Ga}_{\mathrm{x}}$, with x between 15% and 20%. The composition x = 18.4% is the most successful on the pre-market applications up to now (http://tdvib.com/galfenol/). In the following we mainly refer to this composition, which corresponds to real samples utilized in the following of this thesis work.

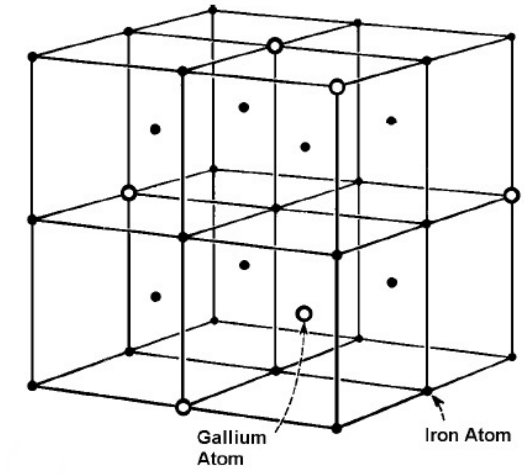

Figure 1.19: Iron BCC crystal lattice with randomly substituted gallium. Image taken from [39].

As all the ferromagnetic materials, Fe-Ga alloy exhibits two regimes of magnetostriction.
The first one, denoted by λ_0, is the spontaneous magnetostriction, in which the strain occurs upon cooling the material throught its Curie temperature, which represent a threshold for the alignment of magnetic moments. Indeed, at temperature below the Curie temperature, the local magnetic moments are collected in randomly oriented domains. But, when the temperature exceeds the Curie temperature, the thermal energy disrupts these collective oriented moments and prevents the formation of new one's magnetic moments. Therefore, passing from one state to the other one is accompanied by a spontaneous magnetostriction. As reported in Table 1.5 the Curie temperature of galfenol is n the neighborhood of 675°C [40].
The second regime of magnetostriction regards magnetization changes, occurred below the Curie temperature, due to applied external magnetic fields. In accordance with the SW approximation [15] already mentioned, the orientation of the local magnetic moment effects the crystal lattice spacing. Indeed, the crystal lattice spatially elongates in the direction of the magnetic domain magnetization vector. Accordingly, to the volume conservation, an opposite sign strain occurs in the transverse direction. The result is an asymmetrical lattice spacing in which the material's

strain is determined by orientation of the magnetic moments. The maximum strain condition, denoted by λ_s occurs when all the magnetic moments are aligned.
The magnetization and magnetostriction response are summarized graphically in Figure 1.20a and Figure 1.20b respectively.

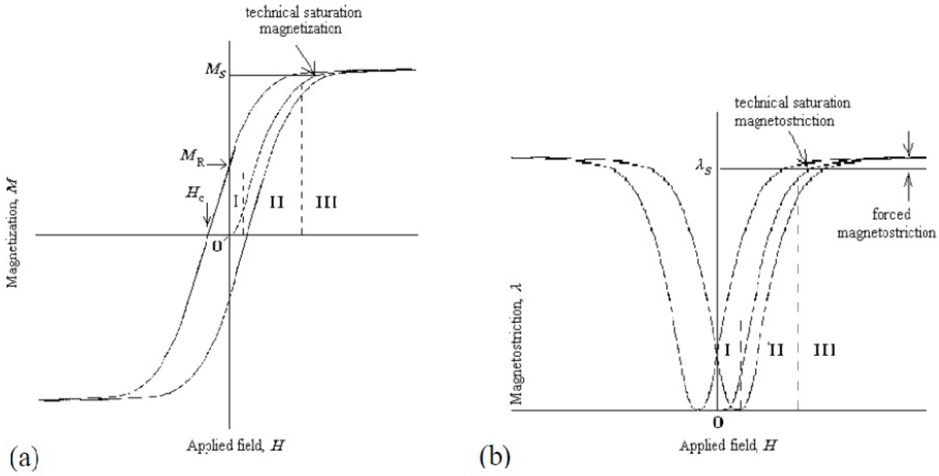

Figure 1.20: Simulated (a) magnetization and (b) magnetostriction curves of a ferromagnetic material to the initial application of an applied magnetic field H. [39].

In stage I, the reversible magnetization and the magnetostrictive strain slowly increase from zero as a result of the applied field H. Stage II is characterised by the domain wall motion, resulting in a rapid increase of the irreversible magnetization. Accordingly, magnetostriction forms the burst region throught a rapid progress. In Stage III the moments are aligned with the magnetic field, and both magnetization and magnetostriction increase at a diminishing rate having reached their technical saturation values M_s and λ_s respectively. After this first response to increasing H, a stable hysteretic magnetization and magnetostriction loops result from a cyclic field application. In the graph of Figure 1.20 it is possible to identify two key points. M_R is the remanent magnetization and corresponds to the material's residual magnetization at zero H. H_c identifies the coercive field, which is the required field to drive the magnetization to zero [41].

Physical properties of Fe-Ga alloy Galfenol represents a promising material for energy harvesting application. In order to better estimate its potential, a first comparison between the behaviours of Galfenol and Terfenol-D materials is reported in Table 1.5.
The values shown in the table cannot represent a complete and satisfactory comparison between these two magnetostrictive materials, and deeper analysis can be found in literature, as for example in the paper [42] of *Berbyuk et al.*. However,

Table 1.5: Comparison between Terfenol-D and Galfenol. Data taken from [11].

Parameters and properties		Units	**Galfenol**	**Terfenol-D**
Magnetostriction	λ	ppm	300-400	1600-2400
Density	ρ	kg/m^3	7870	9210-9250
Curie Temperature	$\mathbf{T_c}$	°C	675	375
Yung's Modulus	$\mathbf{E^s}$	GPa	30-80	10-90
Tensile strength		MPa	515 (ductile)	28-40 (brittle)
Compress. strength		MPa	/	305-880
Elastic Compliance	$\mathbf{S_{33}^{H}}$	m^2/N	$17 \cdot 10^{-12}$	$42 \cdot 10^{-12}$
Effective MS constant	d_{33}	nm/A	18	8-20
Magnetic Permeability	μ_{33}^{s}/μ_0	relative	70	2-10
Actuation field (bias)		Oe	~100	~1000
Strain-voltage hysteresis			Very low	Moderate ~10%
Coupling effect	$\mathbf{k_{33}}$		0.38-0.78	0.6-0.85
Material resistivity		$\mu\Omega m$		0.6
Sound propagation speed		m/s		1650-1950
Energy density		kJm^{-3}	2.0-3.1	4.9-25

from the data summed up in Table 1.5 it is possible to observe that Terfenol-D has better magneto-mechanical properties but shows a lower magnetic permeability. Table 1.5 clearly suggests that Terfenol-D has higher values in several parameters, leading consequently to higher output power performances. It has been highlighted how the magneto-mechanical coupling and performances of Terfenol-D make it an up to date material, currently implemented in commercial actuators. Nevertheless, in a range of mechanical vibration input frequencies between 40 and 70 Hz, research grade galfenol outperformed Terfenol-D in the energy test by at least 20% [11], while the other parameters became the same (except only for the magnetic bias). *Kellogg* [39] has found that the saturation magnetostriction strongly varies with Ga content, and a wide range of Fe-Ga composites has been studied, observing the highest values of coupling factor and of gauge factor for compressive stresses lower than 20 MPa and bias magnetic field below 5kA/m. With an alloy composition with 16-19 % of Ga, galfenol exhibits the highest energy density, magneto mechanical coupling and gage factor, and these behaviours make it an ideal material both for actuation and sensing application. As already seen for Terfenol-D,

several papers in literature faced the modelling of the alloy physical properties [42, 43, 44, 45, 46] or performed experimental analysis [47, 48, 49, 50, 51, 52, 53, 54, 55].
In this thesis work we will focus mainly on the use of galfenol for the realization of a direct force EH. This short paragraph aimed at briefly introducing galfenol and its magnetostrictive properties, besides a quick comparison with Terfenol-D. The behaviour of an EH will be analysed in detail in the following both from the modelling (Chapter 2) and experimental (Chapter 3) point of view.

1.3 Energy Storage Unit

Energy is vital to the development of society. The consumption and the production of energy, which derives mainly from the combustion of fossil fuels, increasingly influences the world economy and has an increasingly significant impact on the environment. For this reason, the demand for energy storage devices from renewable sources that are environmentally friendly and with high performance is increasing. Electrochemical Energy is an unavoidable part of a similar clean energy portfolio. Batteries, supercapacitors and fuel-cells are energy devices that are based on the principle of the conversion of electrochemical energy. The choice of the right technology becomes crucial during the design of the energy storage device, since none of them are suitable for all the real working condition of the coupled generation system. In this thesis work, the aim is to convert a mechanical vibration into electric power, which later stored, in order to realise an autonomous system. Despite a relevant part played in the renewable energies, fuel-cells represent a technology not suitable for the purpose of this work, since it requires fuel, usually hydrogen, and another chemical, usually oxygen, to work, making the entire system no more autonomous. Therefore, without any further analysis, a preliminary comparison can be carried out only between supercapacitors and batteries on the energy density, power density and charging time, as shown in the Ragone plot of Figure 1.21. However, also performance parameters, such as cost, safety and cycle life should be considered to have more detailed comparison, as described in Table 1.6

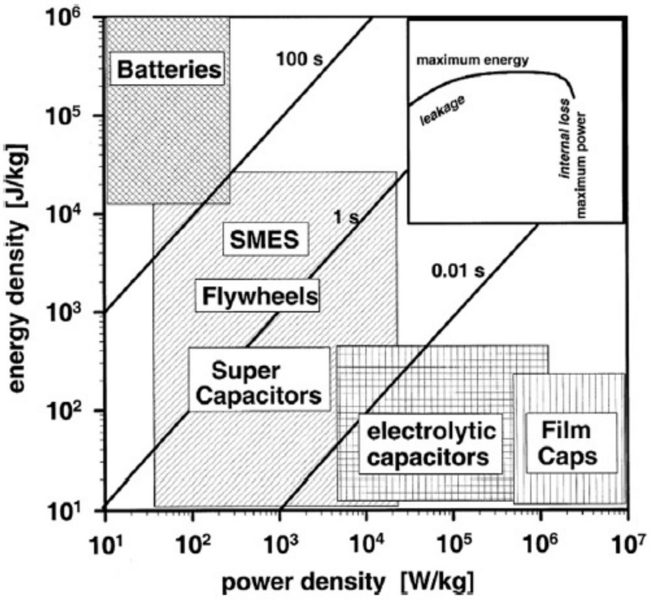

Figure 1.21: Ragone plot [56]. Internal dissipation and leakage losses cause the energy drop shown in the detail window.

Table 1.6: Comparison table among energy storage technologies. Data taken from [57].

Characteristics	Capacitors	Supercapacitor	Battery
Specific energy (Whkg^{-1})	<0.1	1-10	10-100
Specific power (Wkg^{-1})	>10,000	500-10,000	<1000
Discharge time	10^-6 to 10^{-3}	s to min	0.3-3 h
Charge time	10^-6 to 10^{-3}	s to min	1-5 h
Coulombic Efficiency	About 100	85-98	70-85
Cycle life	Almost infinite	$>$ 500,000	about 1000

The Ragone plot of Figure 1.21 and the values summed in Table 1.6 can be used to make a preliminary comparison between batteries and capacitors. It comes immediately that batteries show higher specific energy and lower specific power respect to the supercapacitors. Conversely, supercapacitors have longer cycle-life, up to 500 times higher than batteries. Which, on the other hand, required a limited operating voltage, in order to avoid the chemical decomposition of electrolytes.

1.3.1 Supercapacitor

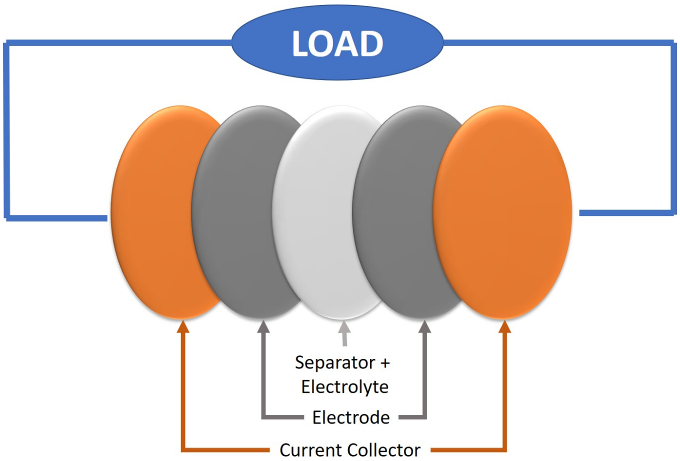

Figure 1.22: Simple scheme of a supercapacitor. The two electrode may be identical, for symmetric cells, or different, for asymmetric cells.

Supercapacitors are ideal in all those applications where a power boost is required but there is no demand for high energy storage capacity. Indeed supercapacitors, compared to batteries, can provide from hundred to thousand times higher power for an equivalent volume but they are able to store 3 to 30 times less amount of charge than a battery [58].

A supercapacitor can be simply schematised as two electrodes divided by a separator, as shown in Figure 1.22. The latter stores the electrolyte and prevents the electrical contact between the electrodes. To allow the ionic charge transfer, the separator must be realised with ion-permeable materials, with high ionic conductance, electrical resistance and low thickness. To achieve the best performance usually polymer or paper separators are coupled with organic electrolytes while ceramic or glass fibre are used together with aqueous electrolytes [59].
The electrolyte plays a crucial part in the cell, since it affects both voltage limits, and the electrolyte conductivity. For example, organic electrolytes lead to higher achievable cell voltage, around 3V against 1V of the aqueous ones. On the other hands, the aqueous electrolytes show higher conductivity [59], ideal for high power device. At the end, aqueous electrolytes can be preferred due to low cost and easiness in handling.
Supercapacitors may be distinguished on the cell configuration or storage mechanism, as summarized in Figure 1.23. The main types of supercapacitors can be distinguished in electric double-layer capacitors (EDLCs), pseudo capacitors and hybrid capacitors. For each type of supercapacitors different electrode materials can be used.

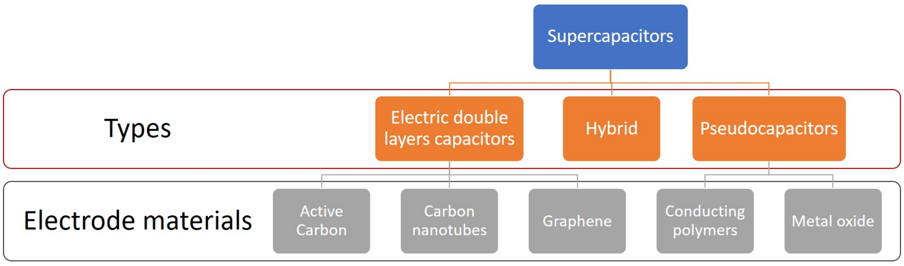

Figure 1.23: Classification of different supercapacitors. Taken from [60]

The EDLCs mechanism can be simply approximated by the Helmholtz model. In this model, when a voltage is applied to an electrochemical capacitor, it causes both electrodes in the capacitor to generate electrical double-layers. One electronic layer is in the electrode's surface while the opposite other emerges from dissolved and solvated ions in the electrolyte. The basic mechanism provides that the physical absorption of the solvent molecules on the electrode surface lead to the separation of the oppositely polarized ions and to the realisation of an idealised molecular dielectric. Between the two layers appears a monolayer of solvent molecules called inner Helmholtz plane (IHP). It is important to note how, in the process, there is no charge transfer between electrode and electrolyte. For this reason, the adhesion cannot be reconducted to chemical bonds, but physical forces, e.g., electrostatic forces. The double layer can be approximated as the dielectric layer in a conventional capacitor, albeit with the thickness of a single molecule. Since EDLCs have high specific surface area ($> 1000\ m^2 g^{-1}$) of activated carbon electrodes and extremely thin double-layer distance (0.3-0.8 nm), it arises that it shows much higher capacitance values than conventional capacitors. Due to their availability and low cost, Nano porous carbon materials are chosen as active electrode materials.

Pseudo capacitors stores electrical energy by means of reversible faradaic redox reactions on the surface of suitable electrodes. The storage mechanism is based on the electron charge-transfer between electrolyte and electrode coming from a de-solvated and adsorbed ion. Since only a charge-transfer takes place, no chemical reactions are involved between adsorbed ion and the atoms of the electrode. During the faradaic processes, the electrons enter the negative electrode and flow through the external circuit to the positive electrode, where they are not transferred to the anions forming the double-layer but remain in the strongly ionized transition-metal ions of the electrode's surface. Therefore, it comes the storage capacity is limited by the finite quantity of reagent in the available surface. The electrode active materials are usually conducting polymer or metal oxide, and sometimes functionalized porous carbons [58, 61, 62]. Pseudo capacitors can hold much higher specific capacitance values as compared to EDLCs, also 10-100 times higher, but lower power performance [63] and cycle life [64]. This important material deficiency is a result of the charge storage mechanism, which relies on fast redox reactions occurring only on the electrode surface and not in the bulk structure, like in the batteries. These redox reactions lead to a poor mechanical stability of the electrodes, which become swell and shrink, as a consequence of the mechanical changes.

Finally, hybrid capacitors, also called internal hybrids [65], are a good compromise between EDLC and pseudo capacitors, being composed of one electrode per type and combining the properties of both systems. The so-called internal series hybrids (ISHs) presents one battery-type electrode, which works at a constant potential and owns a high charge storage capacity, and a capacitive electrode, with a typical sloppy potential profile. One example is the lithium-ion capacitors (LiCs), in which the cathode material is usually an activate carbon, while the anode material consists of pre-doped carbon material with lithium ions. In such a capacitor, it is possible to combine the intercalation mechanism of a lithium-ion battery with the double-layer mechanism typical of an EDLC.

On the other hand, the internal parallel hybrids (IPHs) present coupled battery and capacitive materials in both electrodes. The presence of capacitive material in the electrode allows the supercapacitors to operate at low current, respect the typical ones for battery materials, also providing higher energy. The higher energy resulting from the higher operating voltage and capacity with respect to the symmetric system make these structures suitable for traction application, with a typical charge time less than 10 minutes [58].

Electrical Properties From a macroscopically point of view, supercapacitors devices work like capacitors. Therefore, the electrical properties of a supercapacitor can be evaluated using the same equation of classical capacitor.
The capacitance, C, depends on the dielectric constant ε of the insulator, i.e. the electrolyte, the distance d between the electrodes, the effective thickness of the double layer, and the surface A of the electrodes, as follows:

$$C = \frac{\varepsilon_r \varepsilon_0 \cdot A}{d} \tag{1.14}$$

where ε_r is the relative dielectric constant of the electrolyte and ε_0 is the dielectric constant of the vacuum. For EDL with carbons electrodes, the capacitance usually varies with the electrolyte from 5 to 20 $\mu\mathrm{F} \cdot \mathrm{cm}^2$ [66].
The energy E stored within a supercapacitor depends on the capacitance C and on the cell voltage V, as follows:

$$E = \frac{1}{2} C \cdot V^2 \tag{1.15}$$

From 1.15 results that it is possible to increase one or both the parameters to obtain an increase in the energy density of the cell.
The voltage V and the internal resistance R effects the maximum instantaneous power P_{max} delivered by a supercapacitor as follows:

$$P_{max} = \frac{V^2}{4R} \tag{1.16}$$

At the end, the current I across the supercapacitor comes from the classical definition:

$$I = C \frac{dV}{dt} \tag{1.17}$$

From the above equation, one may see that the main characteristics of devices derive from the capacitance C, the voltage V and the resistance R, which in industry are evaluate with constant current tests, as shown in Figure 1.24.
In particular, from the test it is possible to evaluate directly the voltage V, while the capacitance C comes from the integral of the area contained during the discharge:

$$C = \frac{I_{discharge} t_{discharge}}{U_1 - U_2} \tag{1.18}$$

In a supercapacitor it is possible to identify two different resistance: the resistances associated to the cell (ESR) and the equivalent distributed resistance (EDR), which takes into account the contribution both of the ESR and of the resistance in the pores. The expression of these characteristics are the following:

$$ESR = \frac{U_4}{I_{discharge}} \tag{1.19}$$

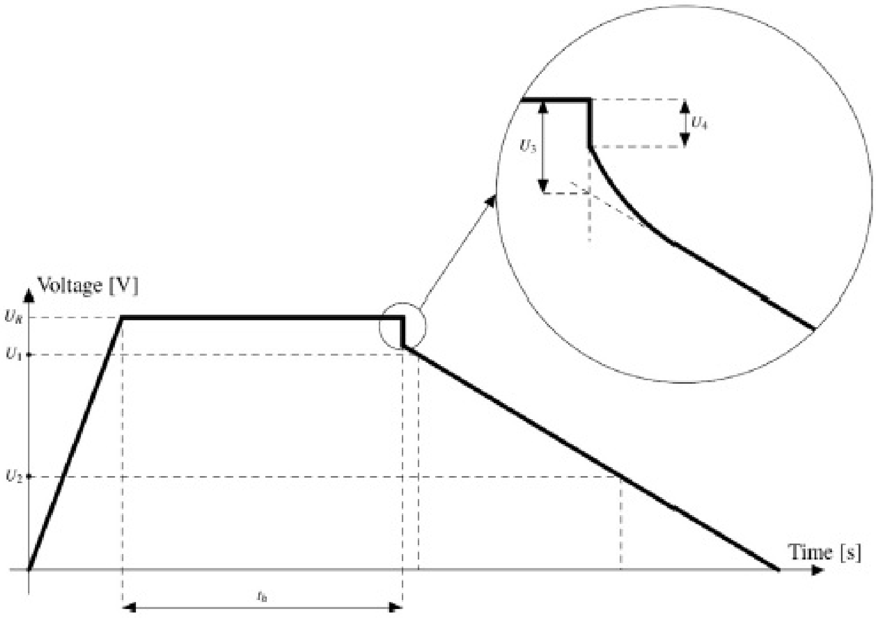

Figure 1.24: Constant current discharge supercapacitor cell test. Taken from [60]

$$EDR = \frac{U_3}{I_{discharge}} \tag{1.20}$$

The measurement of the intrinsic capacitance, a very useful characteristic of the material equal to the specific capacitance expressed in $F \cdot g^{-1}$, is another widely used test in industry. However, the performance of a supercapacitors is not affected only by the specific capacitance but also by the electrical conductivity of the material [62].

So, varying the different components of a supercapacitor, one can affect its own electrical properties.

For instance, the ESR of a supercapacitor should be as low as possible, and it is affected mainly by the contact resistance between the active material and the current collector. A surface treatment of the current collector may decrease the ohmic drop at the interface [67]. For example, when organic electrolytes are involved, usually treated aluminium foils or grid current collectors are employed. On the other hand, it is possible to control the current between the collector and the active material through the use of nanostructured current collector [68]. More broadly, the electrode fabrication requires the coating of a metallic current collector with a thin layer material (generally about 100μm) in the form of a slurry, which is obtained through the mixing with a binder.

Based on highly reversible redox reaction on surface or near-surface, pseudo capacitance is an interesting Faradaic charge storage mechanism. Different charge storage mechanism may be included in this phenomenon, such as intercalation

pseudo capacitance, under potential deposition and redox reactions of transition metal oxides [69]. In conducting polymers, pseudo capacitance can be also associated to reversible electrochemical doping and de-doping mechanism.
It is possible to subdivide the material into two types based on that the pseudo capacitance is defined intrinsic or extrinsic [70].
Ideally, the electrical response is quite the same of a classical capacitor. Since the charge changes in accordance with the potential, it is possible to consider as a capacitance the respective proportionality constant. The main difference between them is that the pseudo capacitance behaviour affects a broad range of particle size and morphology, intrinsic, or doesn't concern the bulk, extrinsic. In this second case, moreover, pseudo capacitance only appears under several conditions and only for nanosized material.
In the end, some materials can combine both capacitive and pseudocapacitive storage mechanism whereas they store a significant charge in a double layer. One example for all could be functionalized porous carbons.

1.3.2 Batteries

In a simple way, a battery is a device that through a reduction-oxidation (redox) reaction can convert the chemical energy contained in the active material directly into electric energy. Since the chemical energy is converted directly into electric energy, despite combustion or heat engines, the battery is not subject to the limitation of the Carnot cycle coming from the second law of thermodynamic. This means that batteries are able to have high energy conversion efficiency.
Among all metals, Lithium is not only the lightest, but has also the greatest energy density and the highest voltage. The story of lithium battery technologies starts with the work of Harris in 1958 [71], and nowadays lithium-ion batteries (LIBs) are dominating the market of power sources for portable electronic devices, in particular for cell phones and laptop computers [72].
Electric and hybrid vehicles represent another market in which LIBs can emerge thanks to the continuous technological development that has involved them so far [73, 74, 75, 76] in terms of power density, capacity, charging rate, cycle life stability but also safety performance and low cost. One for all, the LIBs's efficiency has been increased by 5-10 % every year for the past 25 years [77], passing from a highest energy density value equal to $\sim$ 90 Whkg^{-1} [78] in the 1990s to a currently value approaching 260 Whkg^{-1} [79]. Finally, LIBs can be used as storage units for renewable energy, such as solar and wind, and for energy harvesting. In both cases, LIBs play a decisive role in allowing energy storage in the presence of a surplus of production and a partial and/or total supply of energy in the lower production phases. For example, excess solar energy produced during the day can be stored to subsequently provide electricity at night.

Nevertheless, intrinsic theoretical limitations [77, 80, 81] of the conventional electrode materials blocks the development of LIBs able to satisfy the growing demand in terms of energy densities and fast charging times.
Lithium-ion batteries are significantly exceeding all other rechargeable batteries currently on the market [76]. Figure 1.25 clearly shows the higher energy density of lithium-ion batteries compared to several other rechargeable batteries. The only batteries with an even higher theoretical energy density are lithium metal batteries, which, however, also show less charging and increased sensitivity to mistreatment.

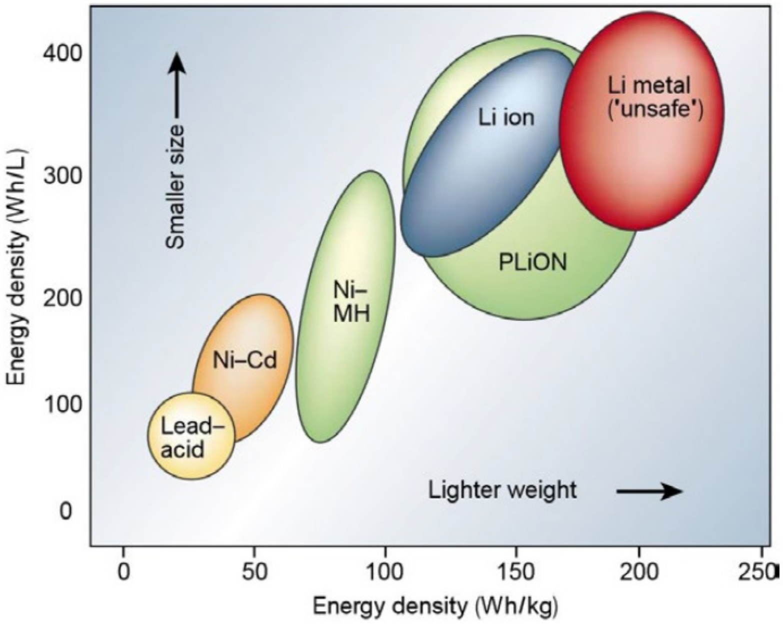

Figure 1.25: Comparison of volumetric energy densities (with volume expressed in liter) and specific energy of different rechargeable batteries. Image taken from [77].

Lithium-ion batteries will dominate the market for rechargeable batteries for at least another decade thanks to their own advantages. The design is flexible, and lithium-ion batteries can be produced in a variety of shapes and sizes to fit any device. Compared to Ni-Cd batteries, they do not suffer from memory and work at almost three times higher voltages than the typical values of Ni-based batteries. A higher single-cell voltage implies a minimized number of cells required to reach the same voltage in a battery module, with a reduced need for associate hardware and a sensible enhancement in terms of reliability and weight savings. The self-discharge rate represents another strength of LIBs. A typical figure is $< 5\%$ per month, very favourably if compared to 20–30% of Ni-based batteries.
A typical lithium ion battery consists of an anode, typically graphite-based, an electrolyte and a cathode, which contains lithium atoms generally intercalated into

a lithium transition metal oxide, such as LiCoO2 [74]. This structure is based on several studies upon fast ion conditions that demonstrate that alkali metal ions, such as lithium ones, moves faster in an electronically conducting lattice containing transition atoms. The typical energy density of conventional cells is equals to ~ 120 Whkg^{-1} [74].

In these electrochemical systems, the redox process is based on intercalation / deintercalation of lithium ions between the two layered materials [82] a mechanism that displays fundamental limitations preventing further improvements. In fact, considering the anode, for example, graphite is able to exchange only 1 Li+ every 6C atoms, achieving a theoretical specific capacity of 372 mAhg-1 [83, 84]. Alternative processes such as alloying [85] or conversion [86] are exploited to overcome these limitations, leading to higher capacity values, which consequently increase the energy density of the currents LIBs [87, 88].

Basic of LiB Also if the “battery”is the term often used, it would be more correct refers to the term “cell”. Indeed, while a battery could consist of one or more cells, a cell is the basic electrochemical unit providing electrical energy. A battery can be realized connecting basic cells in parallel (to increase current) or in series (to increase voltage), or also combined configurations. A combination of battery cells forms a module, and multiple modules constitute a battery pack. For example, 7104 cells are necessary to realise the 85 kWh battery pack inside a typical Tesla car (`https://electrek.co/2016/02/03/tesla-battery-tear-down-85-kwh/`).

As anticipated before, the structure of a unit cell includes:

- an anode (or negative electrode)
- a cathode (or positive electrode)
- an electrolyte.

The negative electrode is the one that gives electrons to the external circuit while it is oxidized. The cathode, instead, accepts the electrons by the external circuit and it is reduced. And the electrolyte provides the medium for the transfer of the ions but not electrons. The two electrodes, through a mechanical separator, are not directly in contact in order to prevent internal short-circuit. However, the separator is permeable to the electrolyte, which can be liquid, polymeric, gel and also ceramic.

In Figure 1.26 are shown the basic operating principle of a typical Li-ion battery cell, which is still the same as those ones commercialized over two decades age by Sony.

At first, the cells are assembled in discharged state. When the two electrodes are connected externally to an electrical supply, the electrons move externally from the supply to the anode, and the lithium ions follow the same direction, but internally, from the cathode to the anode through the electrolyte. In this way, the two

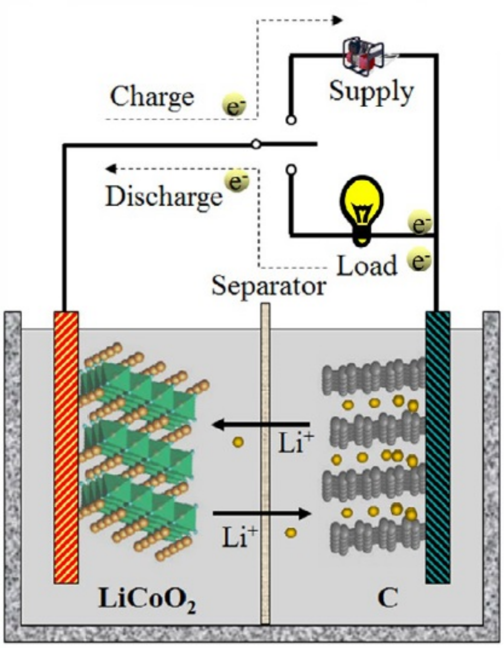

Figure 1.26: Illustration to show the basic components and operation principle of a Li-ion cell. Image taken from [75].

electrodes will be at different chemical potentials, with a resulting electrochemical energy stored in the battery. When the battery is connected to an external load, a reverse reaction occurs which releases electrons in the external circuit, while the electrolyte let the transfer of Li ions through the separator.

This mechanism is sometimes referred as “shuttle chair”, since the Li ions shuttle between the two electrodes all the times.

The selected electrode material determine the total Gibbs free energy change, which is related to the electrochemical reactions on the two electrodes. The theoretical cell voltage ($\Delta E = -\Delta G/nF$) is then evaluated starting from the overall electrochemical reaction and charges transferred.

The comparison between different Li-ion batteries can be carried on several parameters, such as:

- specific energy
- volumetric energy
- specific capacity
- cyclability
- safety

- abuse tolerance
- dis/charging rate
- cost
- process scalability
- time consuming

With the gravimetric specific capacity (Ah/kg) is indicated the amount of charge reversibly stored per unit mass. Multiplying it with the battery voltage (V) gives as results the specific energy density. Gravimetric energy (Wh/kg) and volumetric energy (Wh/l) densities represent the amount of energy stored respectively per unit mass and volume.

Cycle life stability measures the reversibility of the Li-ion insertion and extraction processes, in terms of the number of charge/discharge cycles before the battery loses energy. Practically, to evaluate the cycling life of Li-ion batteries, parameters as depth of discharge (DOD) and state of charge (SOC), operating temperature, have to be taken into account. Regardless the chemistry of the system, cycle life usually can be prolonged by the applying of not deep DOD cycles and SOC and avoiding high temperature. Li dendrite formation on graphite anode can occur at low-temperature charge which should be avoided [89].

Theoretical capacity of active electrode materials can be estimated based on electrochemical reactions involved. For example, electrochemical reaction for the anode of graphite that can intercalate reversibly with lithium to form LiC6, the reaction is:

$$Li^+ + e^- + C_6 \leftrightarrow LiC_6 \tag{1.21}$$

The theoretical specific capacity (mAh/g) of anode graphite can be estimated as follows:

$$C_{specific} = xF/nM = \frac{1 \times (96485\ \mathrm{C/mol})}{6 \times (12\ \mathrm{g(mol)}} = 372\ \mathrm{mAh/g} \tag{1.22}$$

where x is the number of electrons transferred in reaction (1), $F = 96485C/mol$ is Faraday's constant, n is the number of moles of a chosen electroactive component that take place in the reaction, and M is the molecular weight of the same electroactive component. The cathode reaction for LiCoO2, with 0.5 as the practical number of electrons transferred, is

$$LiCoO_2 \leftrightarrow 0.5Li^+ + 0.5e^- + Li_{0.5}CoO_2 \tag{1.23}$$

The theoretical specific capacity can be estimated similarly

$$C_{specific} = xF/nM = 0.5 \times (96485\ \mathrm{C/cmol})/1 \times (98\ \mathrm{g/mol}) = 137\ \mathrm{mAh/g} \tag{1.24}$$

In practice, to evaluate specific capacity of a Li-ion battery cell, one not only has to take into consideration the integration of cathode and anode materials but also other essential components, such as binders, conductive enhancers, separators, electrolyte, current collectors, case, tabs, as well as BMS.
Therefore, the practical energy density is always less than that estimated based on the battery chemistry.

Electrolyte Nowadays, Li-ion battery commercially available usually imply liquid electrolyte based on a solution of lithium salts in organic solvents. Among all the organic solvents widely explored, it is possible to remember dimethyl carbonate, diethyl carbonate, ethyl methyl carbonate, propylene carbonate, ethylene carbonate, diethoxyethane, dioxolane, γ-butyrolactone, and tetrahydrofuran. Between the lithium salts, the choice usually includes LiPF6, LiBF4, LiAsF6, LiClO4, and LiCF3SO3. Simple anions of Cl-, Br-, and I- are generally not considered in order to avoid the oxidation of the charged surface of cathodes.
The success of commercial Li-ion batteries could be ascribed to the industrial scale availability of high-purity LiPF6, which guarantees minimum amount of water. LiPF6 outstands all the other lithium salt in terms of safety, conductivity and balance between ionic mobility and dissociation constant [89]. The commonly used electrolyte is 1M LiPF6 in a 50:50 w/w mixture of ethylene carbonate (EC) and diethyl carbonate (DEC) or dimethyl carbonate (DMC) (1.27).

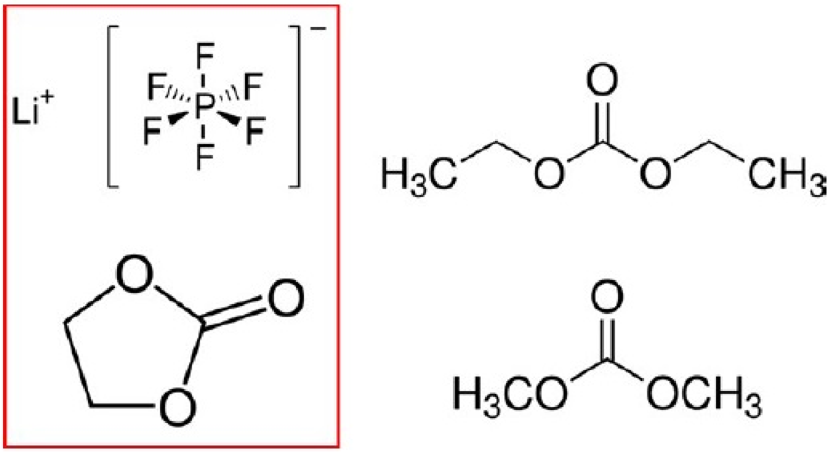

Figure 1.27: Chemical structures of common components in commercial electrolyte: LiPF6 as the lithium salt and ethylene carbonate as the solvent are present in almost all commercial electrolyte; whereas diethyl carbonate or dimethyl carbonate are also present to reduce viscosity to promote ion transfer.

Even though the formulated electrolyte offers reasonably good stability, commonly additives are added to further enhance the electrolyte stability [90]. Polymer, gel

and ceramic electrolytes are other types of electrolyte under study. Using high molecular weight-based polymers with dissolved lithium salts, polymer electrolytes represents an interesting solvent-free choice [91].
The advantages of polymer electrolyte over liquid electrolyte are:

1. improved safety properties due to low volatility;
2. design flexibility (cylindrical, coin, prismatic, flat cells and other configurations [92, 93]);
3. potential to eliminate separators.

Poly(ethylene oxide), coupled with various lithium salts (such as LiCF3SO3 and LiClO4) represents one of the most widely studied polymer, in which the ion conduction mainly occurs at amorphous phases. The semirandom motion of short polymer segments are responsible of the ion transportation.
The conductivity is typically about $10 - 8$ S/cm, which is significantly lower than that of liquid electrolyte in order to maintain a good mechanical stability.

Cathode There are a number of candidates that have been explored as cathode materials for Li-ion batteries. The cathode materials can be categorized based on voltage versus lithium.

Table 1.7: categorization of cathode materials based on voltage versus lithium

Voltage vs Lithium	Cathode Materials
2-Volt	TiS2 and MoS2 with 2-D layered structure
3-Volt	MnO2 and V2O5
4-Volt	LiCoO2, LiNiO2 with 2-D layered structure
	3-D spinel LiMn2O4 and olivine LiFePO4
5-Volt	Olivine LiMnPO4, LiCoPO4
	Li2MxMn4-xO8 (M = Fe, Co) spinel 3-D structure

Usually, high cathode voltage (such as 5-volt cathode materials, see Table 1.7) looks desirable being the energy stored proportional to the cell operating voltage. Therefore, it shouldn't surprise that currently, in commercial Li-ion batteries, LiCoO2 and LiFePO4 (both categorized as 4-volt cathode materials in Table 1.7) are most widely used. In addition to its cycle life (>500 cycles), LiCoO2 can be easily manufactured in large scale and is stable in air, but its practical capacity ~ 140 mAh/g turns to be quite the half of its theoretical capacity of 274 mAh/g upon full charge, appearing as a noticeable disadvantage of the LiCoO2, together with the high material cost and the toxicity of cobalt. Contrary, LiFePO4-based cathode materials have low cost and low environmental impact, and for this reason are being more and more attractive. LiFePO4 has also other advantages over LiCoO2, such as stability, excellent cycle life, and temperature tolerance (-20 to 70 °C). The one-dimensional channels for lithium ion diffusion, easily lockable by defects and impurities, is an issue. However, a relatively low capacity, in addition to a poor electronic and ionic conductivity (at 10^{-10} S/cm and 10^{-8} cm^2/sec respectively) represent the major issues [94], which are usually faced through ions doping and carbon coating [94, 95].

Structural and electrochemical analysis reveal how the doping affects the LiFePO4 performance reducing the lithium miscibility gap, increasing phase transformation kinetics and expanding Li diffusion channels [95]. For example, *Chaing* et al. [94] reported a factor of 108 of electronic conductivity increase in LiFePO4 due to a cation doping. As reported by *Kang et al.* [96], the electrical conductivity and the lithium ion diffusion velocity strictly depend on the doping amount. In nanocrystalline LiFe1-xSnxPO4 ($0 \leq x \leq 0.07$), the highest capacity at all rates is reached with a doping amount of about 3 mol%. Also cycling is affected by doping. In a LiFe0.9M0.1PO4 for (M = Ni, Co, Mg) doped electrode, the enhanced conductivity and mobility of Li+ ions lead to an improvement on rate performance and cyclability [97], passing from a capacity retention of only 70% up to a 95% capacity maintained at 80-90 mAh/g (corresponding to a 10 C rate).

LiFePO4 off-stoichiometry design (e.g., LiFe1-2yP1-yO4-δ) represents an alternative to Fe-site doping. Ceder reports an impressively simple process, ready to be easily carried out in manufacturing process, to achieve high lithium bulk mobility [98], realizing a fast ion-conducting surface phase of glassy lithium phosphate containing Fe3+.

The production of high-power Li-ion batteries, based on LiFePO4, is possible through the combination of doping and nanoscale size.

In addition to doping, LiFePO4 carbon coating demonstrates to improve the relative electrochemical performance [99], even realizing a high power and high energy electrode with a simple dispersion procedure of LiFePO4 nanoparticles in a nanoporous carbon matrix [100]. In particular, the conducting nanoporous 3D network, which serves as an electrolyte container for high-rate operation, leads each LiFePO4 particle to achieve full utilization of the active material. The very simple preparation procedure, based on a sol-gel method followed by a solid-state reaction, could be implemented for industrial scale production in the future.

LiFePO4 carbon coating, through a vapor deposition process, is another interesting technique due to the formation of few monolayers of carbon film on the olivine particles surface coupled with carbon deposition inside the pores of the particles [101]. Due to the dramatically improved conductivity, C-LiFePO4 is considered very promising to replace those toxic transition metal oxide-based cathodes.

Finally, it's worth mentioning the conductivity enhancers process based on the preparation of LiFePO4 thin films with uniformly dispersed highly conductive silver [102], achieving impressive electrochemical performances in terms of specific

capacity, cyclability, and charging rate.
However, LiFePO4 still presents challenges. If on one hand, the introduction of nanoscale structure may increase its rate performance or power, on the other one relatively moderate specific capacity or energy (by mass) of LiFePO4 associated with its chemistry does not provide much space for further improvement.
A completely different cathode material is the layered lithium nickel cobalt manganese oxide (with average composition of Li[Ni0.68Co0.18Mn0.18]O2) microparticles [103]. The cathode materials is unique in the way that the microparticles have concentration gradient, where the core is rich in Ni, and the outer layer is rich in Mn with decreasing Ni concentration and increasing Mn and Co concentrations at the surface (1.28).

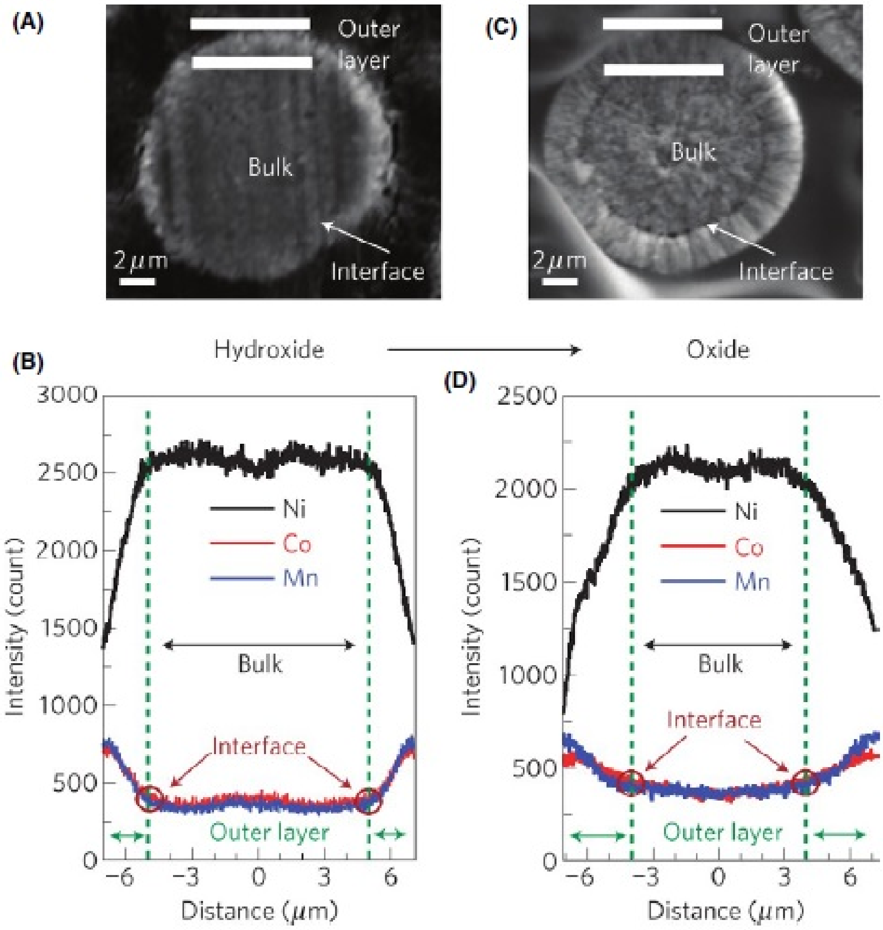

Figure 1.28: SEM images of (A) the precursor hydroxide obtained by coprecipitation, and (B) the final concentration-gradient lithiated NCM oxide; (C) and (D) are the corresponding electro-probe X-ray microanalysis line scans for (A) and (B), respectively. Image taken from [104].

The bulk core of Ni-rich cathode provides high capacity. The concentration-gradient outer layer and the surface improve the thermal stability. The cathode materials demonstrated impressive high reversible capacity of 209 mAh/g and good safety characteristics. It should be noted that the materials preparation procedure based on coprecipitation in aqueous solution followed by calcination at 780 °C is very simple and scalable, which is suitable for industrial scale production. This high-capacity concentration-gradient cathode material is promising to be produced on a large scale and used in next-generation commercialized Li-ion batteries.

Anode Since the very first commercialization, the market is still dominated by graphitic carbon, which layered structure improve the movement of lithium ions in and out of its lattice. The direct consequence is a minimum irreversibility, which leads to an excellent cyclability [105]. On the other hand, carbon anodes are approaching their theoretical maximum capacity of 372 mAh/g and seems to be no more able to increase it. In order to meet the demands on energy and power density [94], the investigation on anode materials did not end but addressed to carbon alternative with high-energy density.
Many elements are known to alloy with lithium. These can be classified into three main types referring to the reaction mechanism of lithiation and delithiation:

- insertion/extraction;
- alloying/dealloying;
- conversion mechanisms.

Anatase TiO2 belongs to the first category [49], such as most of cathode materials with layered or spinel structures. TiO2-based anode materials have been extensively explored. However, its practical capacity is not comparable to that of carbon anodes due to the voltage (versus Li/Li+ couple) at which the lithium insertion takes place: it is respectively about ∼1.5 to 1.8 V in Ti=2 respect the low voltage close to 0 V of carbon anodes. Another notable difference is that SEI could not form on TiO2 in the potential window, while the SEI formation on carbon causes the first-cycle irreversible capacity loss issue.
In the second category, Silicon takes the lion's share and represents in general a promising candidate to replace carbon.
Silicon has a high theoretical capacity of 4200 mAh/g (lithiated to Li4.4Si) or 3572 mAh/g (based on Li3.75Si) which is about 10 times with respect of that of graphite and almost four times compared to that of many metal oxides.
But, if on one hand silicon can alloy and de-alloy with lithium at room temperature, on the other one these processes are accompanied by substantial variations in the specific volume (about 400 %) upon cycling. The consequence is an induced huge mechanical stress, which leads to the destruction of the crystal structure together

with the disintegration of the active material and current collectors within a few cycles. This condition makes practically difficult the use of a bulk silicon anode. Silicon nanostructured anode materials represent an interesting option, also if a large-scale production of a semiconductor in nanoparticles is more difficult with respect to metallic anodes.

A simpler approach, based on silicon/carbon composite anode materials, can be adopted to face the following poor cyclability problems. The existence of a huge number of combinations involving silicon and carbon [95] represents the success of this approach. In these composites, carbon functions as a stress absorber whereas silicon provides the boost in capacity. Nowadays, however, commercial Si-based electrodes contain a significantly high percentage of carbon and only a small percentage of Si.

With a theoretical capacity of 781 mAh/g, which is about two times higher than graphite, another anode candidate promising to replace carbon anodes is the SnO2-based anode. In its first cycle of lithiation, SnO2 is converted to Sn, and subsequently, the Sn phase could store and release Li ions according to the Li-Sn alloying and dealloying reactions. As silicon, also SnO2 suffers of poor cyclability, and nanostructured SnO2 has been proposed as a possible solution [97, 101, 102, 103, 106, 107, 108].

Although metal oxides are generally poor in conductivity, this choice represents another family of anode material with high capacity [109].

For the realisation of the energy storage unit, in this thesis work it was realised a Li-ion cell composed by a commercial cathode (NMC111) and a Si-graphene based anode. In Chapter 4 will be discussed the methods to realise the anode composite together with the chemical-physical characterization and SEM-TEM imaging. In Chapter 5, the electrochemical characterization of the anode and of the Li-ion cell will be presented. Finally, in Chapter 6, the Li-ion cell will be implemented in a fully-working vibrational harvester as the storage unit. It will be demonstrated both the ability of the Li-ion cell to be charged by the harvester and to supply a BLE wireless sensor.

Chapter 2

Computational model

2.1 Sally2D software

MSMs generally can be described by the constitutive magnetostrictive equations:

$$\begin{cases} T = \frac{1}{s^B}S - \lambda B \\ H = -\lambda S + \nu^S B \end{cases} \tag{2.1}$$

where T is the stress and S is the strain, with B as the magnetic flux density and H as the magnetic field. The superscript S or B indicates respectively a constant stress or magnetic flux.

A thermodynamic demonstration [9] of 2.1 can be found in Appendix A.

In the early 90s models of magnetostrictive material were simply considered as a nonlinear element neglecting the magneto-elastic coupling [110, 111, 112, 113] and the field distribution within the device was evaluated through a finite element field analysis.

Starting with these early work, more and more detailed models have been developed over time [114, 115], also with the integration of advanced hysteresis models [25, 116, 117, 118, 119].

Focusing the attention on the models based taking into account hysteresis, one may see that in [120] it was presented one of early models of a magnetoelastic rod. The model, being coupled with a finite element field solver (formulated in the frequency domain) was capable to taking also into account the eddy currents in all conductive elements. Anyway, due to the simplified hypothesis of a steady-state working condition, the model did allow the analysis only for simple supply patterns, enough for the study and design of new devices, resulting in this way inadequate in applications for real-time control of mechanical vibrations. The issue was solved later, in other papers like e.g [121] where the MST rod behaviour is studied together with the excitation magnetic circuit through a field - circuit formulation including the model of the material behaviour. The so formulated finite element – magnetoelastic

model in the time-domain, allows the analysis under arbitrary supply conditions, also taking into account dependence of mechanical stress on time.
The computational code utilized in this thesis work implemented the model above mentioned. The approach is two-dimensional, where axis symmetric 3D geometries can be studied. The software is based on the Finite Element Method (FEM), and is constituted by three main modules:

- pre-processing
- solver
- post-processing

2.1.1 Pre-processing

The pre-processing phase has the aim to define on one side all the data needed to define the rigidity matrix and, on the other one, the known terms of the algebraic system associated to the method. These data may include:

- structures geometry
- domain subdivision into finite elements
- materials characterization
- sources description
- contour conditions

The global domain is described through a discrete number of master nodes, geometrical points already provided of the respective space coordinates. An ordered succession of master nodes constitutes a region, which is the basic structure used to subdivide the different structure components. Each side of a region is identified by the master nodes that constitute the ends, plus supplementary information such as the side shape (straight, curvilinear, etc.), the number of wanted subdivision and the distribution of the master nodes on the side.
Then each region is cross-linked following the Delaunay mesh condition. At the end, each region is associated to a material through a code-number.
The mesh generation can be semi-automatic or automatic.
In the first case, usually adopted for triangular or quadrangular regions, the user control directly the formation of the basic triangles. It indicates the number of stripes which subdivide the region and also the most appropriate algorithm to generate the triangles. In order to achieve results with the required accuracy, it is possible to follow the above general criteria to design a good mesh:

1. The mesh must be thickened in regions where field sizes vary quickly; vice versa regions in which a uniform distribution of the field quantities is expected, may be represented with relatively large elements, regardless of the value of the field quantities themselves.
2. Equilateral triangles guarantee a better accuracy; triangles with obtuse angles greater than 170° must be avoided.
3. The mesh must respect, as far as possible, the geometric symmetries present in the problem under analysis.
4. The mesh must be made thicker in regions where the structure under examination forms angles greater than 180°, or elements with singularity must be included.
5. One may avoid creating triangular elements where all vertices have the required nodal values at the same value.
6. In axisymmetric problems, with the same accuracy, the mesh must be thickened as one moves away from the axis of symmetry. However, if the axis of symmetry is included, the mesh must be kept sufficiently thick around the axis.

In the second case, the mesh generation is totally entrusted to the software.
The automatic patter generation can be schematize as follows.

First attempt mesh The software generates a first-attempt mesh, starting from a polygon which sides contain the master nodes. For example, a first triangle may be constructed having three consecutive master nodes (clearly, the so formed triangle does not have null area or be outside the polygon). Once this operation is successfully concluded, the form of the polygon is modified, discarding the two side is linked to the internal node. This operation is repeated until the entire polygon is subdivided in triangles.

Evaluation and improvement of the triangles quality The software then evaluates and improves the quality of the triangles. Indeed, the calculus precision significantly decreases when the triangles present an inner corner near 180°. So, it is necessary to introduce some criteria to evaluate the quality of the triangles. The ideal triangle is the equilateral triangle. For this reason, the triangle quality factor is introduced, and is defined by the following relation:

$$q = \frac{8}{(s-a)(s-b)(s-c)}abc \tag{2.2}$$

where a,b,c are the length of the sides and s is the semi-perimeter. In above relation, the factor quality q represents the ratio between the inscribed circle diameter and the circumscribed circle radius. It is always a positive number, with a maximum value equal to 1 in the case of an equilateral triangle.
It is also possible to compare the quality factor of a couple of triangles through the equation:

$$q_{1,2} = \frac{2}{\frac{1}{q_1} + \frac{1}{q_2}} \tag{2.3}$$

This parameter is employed by operational techniques in order to subdivide the mesh into triangles as like as possible to equilateral ones. One of these techniques is the Delaunay criterion.
It is based on the examination of the quadrangular formed by two adjacent triangles. The shared side represents the one of the internal diagonals of the quadrangular. According to this approach, are assessed the effects of the diagonal exchange (swapping) of the quadrangle on both the quality factor of the two new triangles generated with this operation. That is, after having verified that the quadrangle in question is convex (in a concave quadrangle the swapping is not possible), the quality factor of each of these pairs of triangles is calculated and the solution that provides the highest value of the quality factor itself is chosen.
The procedure is repeated several times, until no more quadrangles are found in which it is possible to carry out the swapping.
Alternatively, or in addition to swapping, it is possible to look for improvements in the mesh also moving single nodes, whose position is not constrained by reasons of congruence. The effects of this operation are evaluated with the quality factor referred to all the triangles affected by the movement of the node, through the equation:

$$q_M = \frac{N}{\sum_{i=1}^{N} \frac{1}{q_i}} \tag{2.4}$$

Mesh refinement The mesh can be thickened by inserting new nodes on a basis of geometric characteristics. The algorithms used for this function (error estimators) are based on errors estimations made with a posteriori technique, using numerical solutions to the problem. In other words, one tries to express in a normalized quantitative form the deviation of the calculated solution exact solution (physical properties, symmetries, etc.). The error estimator must then provide a function that is the distribution of the error in the crosslinking.
The increase of nodes in the most critical areas can be carried out in various ways. Usually a new node is inserted into a triangle which is thus divided into three triangular elements, without having to change the connections of the elements surrounding. It is also possible to insert the new node directly on one side of the triangle (usually the longest) which is thus divided into two elements; in this case,

however, the triangle sharing the same side must also be subdivided to maintain the congruence of the reticulation. After the insertion of new nodes, it is convenient to repeat the operations for the improvement of the mesh quality.

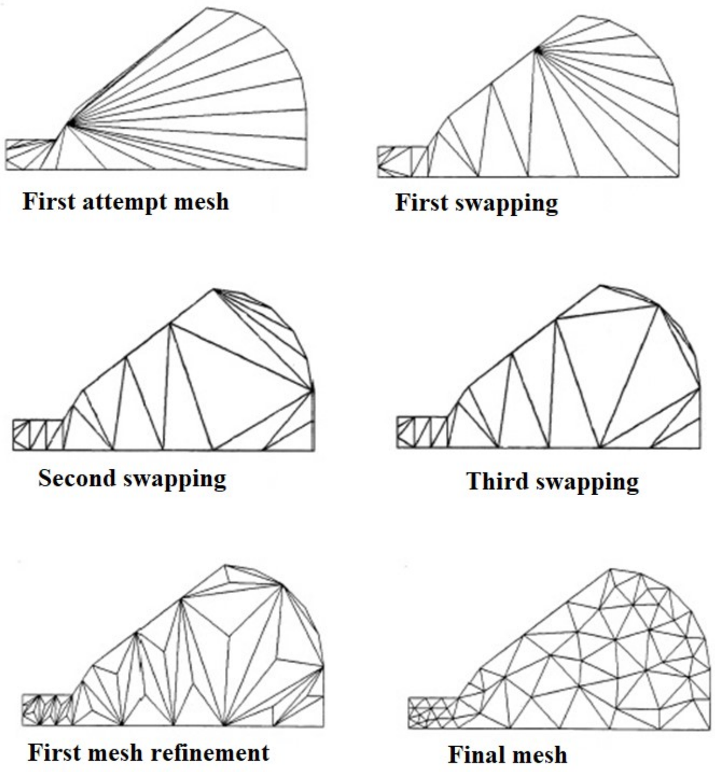

First attempt mesh

First swapping

Second swapping

Third swapping

First mesh refinement

Final mesh

Figure 2.1: An example of an authomatic mesh generation

2.1.2 Solver

To accurately model the MST rod, both magnetic and mechanical hysteresis have to be properly taken into account. In the literature, mechanical effects are introduced in hysteresis models, basically following three alternative ways.

- One is based on the idea of modifying the properties of the hysteresis model (e.g. in the Preisach model this can be obtained by changing the Preisach distribution function). An example of this approach in described in the paper [122].

- An alternative approach starts from physical basis and introduces the mechanical effects throughout an effective field, which is related to the applied mechanical stress [123, 124].

- Finally, genetic algorithms have been more recently applied to reconstruct the response of a magnetostrictive material, starting from a large set of experimental data [125, 126].

In this thesis work, it was adopted the second approach based on the introduction of an effective field H_e, which is obtained by summing to the applied external field H, a corrector term $\xi(J, \sigma)$, which is function of the mechanical stress σ, as well as of the magnetic polarization J:

$$H_e = H + \xi(J, \sigma) \tag{2.5}$$

This approach has been already experimented for Terfenol-D [127] but its validity has never been tested for galfenol. Although galfenol has limited hysteresis, whether or not to keep it into account may vary the accuracy of the results, even if only slightly.
Magnetic flux density B is expressed as:

$$B = \Psi(H) = \mu_0 H + J = \mu_0 H + \zeta(H_e) \tag{2.6}$$

where the magnetic polarisation J, including reversible and irreversible contributions, depends on H_e. Hysteretic function ζ is described through the classical Preisach model (CPM). In all the field quantities, the dependence on time is omitted for the sake of simplicity. Moreover, CPM is assumed to be a scalar model, that is magnetic field and magnetic flux density are aligned and oscillate along a fixed direction (main direction). In presence of alternating 2-D fields, the main direction is determined and an equivalent scalar field is estimated to enter the MS-model. This approximation is made possible by studying the 3D geometry with the axisymmetric 2D approach, taking into account that the magnetic field in the rod is unidirectional. Since no rotating fields are present, unlike to what happens in an electric motor, the scalar approximation is suitable in such a problem.
The correction introduced by the effective field H_e makes the magneto-mechanical (MM) Preisach model implicit, so that an iterative procedure is needed to obtain the output B from a given input H. This problem is solved by applying the Fixed Point (FP) technique. Assumed the applied stress σ and field H to be known, the effective field is written as:

$$H_e = H + \xi(J, \sigma) = H + \xi[\zeta(H_e), \sigma] = H + \Psi(H_e, \sigma) = H + \nu H_e + S(H_e, \sigma) \tag{2.7}$$

where function Ψ is written as the sum of a linear term (with constant ν) plus a nonlinear residual S, which is updated during the iteration process starting from a trial value. At the generic iteration $(m-1)$, the sequence of operations is detailed in the following:

$$\begin{aligned} H_e^{(m)} &= \frac{H + S^{(m-1)}}{1-\nu} \\ J^{(m)} &= \zeta\left(H_e^{(m)}\right) \\ S^{(m)} &= \xi\left(J^{(m)}, \sigma\right) - \nu H_e^{(m)} \end{aligned} \tag{2.8}$$

Effecting both the convergence and the speed of the iterative method, the definition of the FP constant ν may represent the difference between a succeed in the simulation or not. For magnetostrictive materials with invariable (or quite close) magnetic characteristic like Terfenol-D, the optimal value of the FP constant can be simply chosen as the average value between the maximum and minimum slopes of the B-H curve. This average value guarantees a regular convergence of the iterative process. However, the relative strong dependence of the magnetic behaviour with the mechanical load σ (as the sum of the preload and dynamic load), makes this assumption not suitable for the Fe-Ga alloy. As well illustrated by the curves in Figure 2, the characteristics show an evident bending at the preload increase. In addition, also the presence of the magnetic bias has a strong effect on the definition of the FP constant, which becomes even more critical.

Unlike magnetostrictive materials like Terfenol-D, not only the average value of the B-H curves slope does not assure an optimal definition, but it is no more possible to guarantee that a single FP constant value may ensure convergence for different values of the mechanical load σ. Therefore, in the case of the Fe-Ga alloy, the FP constant varies together with considered value of σ, and a relative tuning method must be implied.

Finally, to study the behaviour of the entire actuator, the MM Preisach model of a MST rod is coupled with a step-by-step finite element computational scheme, accounting for the electromagnetic phenomena within all the device (FEM-MM model). Taking advantage of the geometrical structure of these kind of devices, the computations are performed in an axial-symmetric domain with cylindrical coordinates r, θ, z.

2.1.3 Post-processing

In the last phase of the simulation, the information deduced on the effective field are used to evaluate the current density **J** in each element.

Working on a quasi-static condition, one can express a bidimensional (z invariant) electromagnetic field with the non linear equation:

$$rot\left(\xi(rot\mathbf{A})\right) = \mathbf{J} \tag{2.9}$$

The current density is expressed by:

$$\mathbf{J} = \mathbf{J}^{(S)} + \mathbf{J}^{(E)} \tag{2.10}$$

The term $\mathbf{J}^{(S)}$ represents the current densities imposed by external sources, such as coil currents due to several conductors with small section. Moreover, these currents are not disrupted by the presence of a variable magnetic field.
Contrary, the term $\mathbf{J}^{(E)}$ represents the current densities, usually non-uniform, as effect of the electromagnetic induction both in conductors not connected to an electric circuit (as in the case of a ferromagnetic core) as in the electric circuit components which have non negligible dimension. In the latter, the induced effects overlap to the uniform current distribution imposed by the sources.
While $\mathbf{J}^{(S)}$ is a-priori known, $\mathbf{J}^{(E)}$ must be determined from the filed contextually to the solution of the latter.
From the Maxwell equation it is possible to deduce the form of $\mathbf{J}^{(E)}$:

$$rot\mathbf{E} = -\frac{\partial \mathbf{B}}{\partial t} \rightarrow rot\left(\mathbf{E} + \frac{\partial \mathbf{A}}{\partial t}\right) = 0 \tag{2.11}$$

Through the introduction of a scalar potential, one may obtain:

$$\mathbf{E} + \frac{\partial \mathbf{A}}{\partial t} = -grad\varphi \rightarrow \left[E_z(x,y) + \frac{\partial A_z(x,y)}{\partial t}\right] i_z = -\frac{\partial \varphi}{\partial x}\mathbf{i}_x - \frac{\partial \varphi}{\partial y}\mathbf{i}_y - \frac{\partial \varphi}{\partial z}\mathbf{i}_z \tag{2.12}$$

These relations imply:

- The potential φ cannot be function but of z $\left(\text{since } \frac{\partial \varphi}{\partial x} = \frac{\partial \varphi}{\partial y} = 0\right)$.
- Its derivative $\frac{\partial \varphi}{\partial z}$ is not a function of z.
- The potential φ is then a linear function in z.
- As a consequence, $grad\varphi$ is a constant in each conductor interested by the electromagnetic induction.

The current density in a generic conductor k is expressed by:

$$\mathbf{J}^{(E)} = \sigma_k \mathbf{E} = -\sigma_k\left(\frac{\partial \mathbf{A}}{\partial t} + grad\varphi\right) = -\sigma_k\left(\frac{\partial \mathbf{A}}{\partial t} + \lambda_k\right) \tag{2.13}$$

The eddy currents in a single conductor may modify the current density distribution but not the total value of the conductor current. Therefore, the value of the constant λ_k can be evaluated through the integral constraint:

$$i_k = \int_{\Sigma_\mathrm{k}} \mathbf{J}^E dS = -\int_{\Sigma_\mathrm{k}} \sigma_k \frac{\partial \mathbf{A}}{\partial t} dS - \int_{\Sigma_\mathrm{k}} \sigma_k \lambda_k dS = -\sigma_k \int_{\Sigma_\mathrm{k}} \frac{\partial \mathbf{A}}{\partial t} dS - \sigma_k \lambda_k \mathrm{S_k} \tag{2.14}$$

where Σ_k is the trace of the k-conductor with surface $\mathrm{S_k}$ in which the conductor itself may be considered homogeneous.
From this it is possible to obtain:

$$\lambda_k = -\frac{i_k}{\sigma_k S_k} - \frac{1}{S_k}\int_{\Sigma_k} \frac{\partial \mathbf{A}}{\partial t} dS = -\frac{i_k}{\sigma_k S_k} - \mathbf{M}_k \tag{2.15}$$

where $\mathbf{M}_k$ it the average time derivative of $\mathbf{A}$ over the surface Σ_k. Therefore:

$$\mathbf{J}^{(E)} = -\sigma_k \frac{\partial \mathbf{A}}{\partial t} + \frac{i_k}{S_k} + \sigma_k \mathbf{M}_k \tag{2.16}$$

2.1.4 Material identification

As well described in [120], the Preisach distribution function mentioned in eq. 2.5 is identified starting from the measured *B*-*H* loops at zero stress, introducing the function factorization and following the approach described in [128]. The successive step is the determination of function ξ , used to compute the effective field H_e. This procedure starts from a set of experimental static *B*-*H* cycles at different stresses, as shown in Figure 2.2.

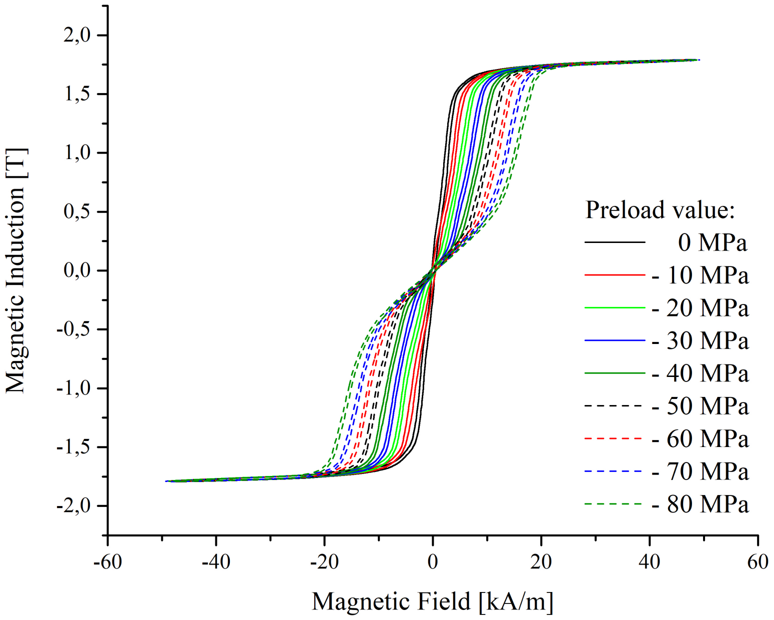

Figure 2.2: Experimental quasistatic B-H loops, measured on the bulk FeGa rod at different levels of the constant preload. For sake of clearness, in the graph are just represented a short number of loops. Image taken from [129].

Given an experimental loop (H_{exp}, B_{exp}) at $\sigma_{exp} \neq 0$, the timewaveform of the effective field H_e is computed and then compared with the experimental waveform

H_{exp}.

$$\begin{aligned} J_{exp} &= B_{exp} - \mu_0 H_{exp} \\ \tilde{H}_e &= \zeta^{-1}\left(J_{exp}\right) \\ \xi\left(J_{exp}, \sigma_{exp}\right) &= \tilde{H}_e - H_{exp} \end{aligned} \tag{2.17}$$

An example of this process can be seen in Figure 2.3 The inversion of the Preisach model (ζ^{-1}) is performed through a numerical procedure. This scheme, repeated for all the measured loops at different values of σ_{exp}, gives a number of sampled values of ξ. Where it is possible, through the use of a least-square fitting, the sampled values of ξ are interpolated by the function:

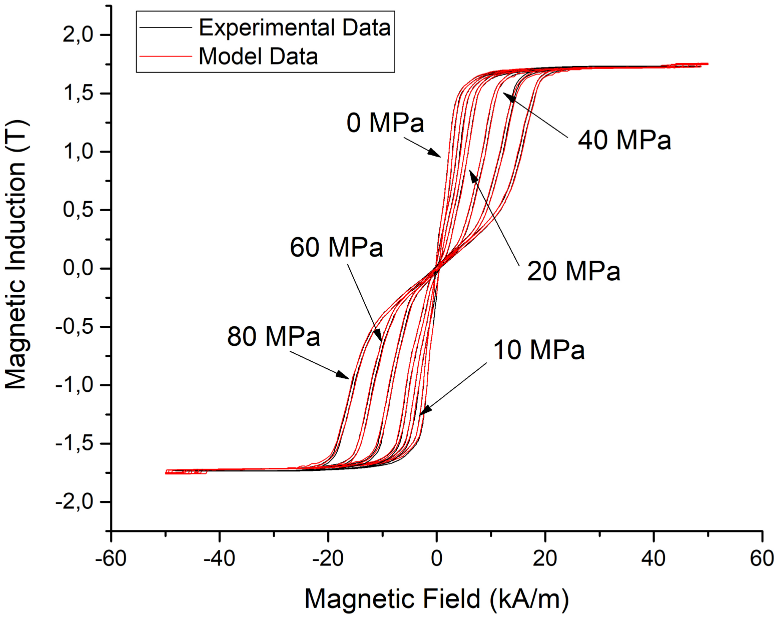

Figure 2.3: Superposition of model data B-H loops on experimental B-H loops of fig. 2.2. For sake of clearness, in the graph are just represented a small selection of loops. Image taken from [129].

$$\xi\left(J, \sigma\right) = \sum_i \sum_j a_{ij} \sigma^i J^{2i+1} \tag{2.18}$$

where a_{ij} are constant coefficient. This procedure was used in [121], in which it was characterized a rod of Terfenol-D.

In the case of galfenol, it was not possible to identify a function capable to interpolate the sampled values of ξ. For this reason, the function $\xi\left(J_{exp}, \sigma_{exp}\right)$ is represented as a tabular function, in which the couple of simulated data is reconstructed through a 4-points spatial interpolation. Each simulated point is considered a linear quadrilateral element of the tabular function $\xi\left(J_{exp}, \sigma_{exp}\right)$, as shown in Figure 2.4

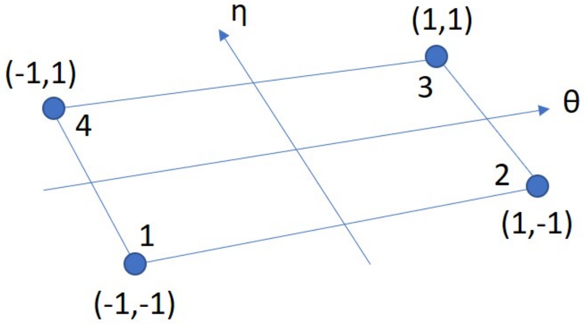

Figure 2.4: Scheme of a general linear quadrilateral element.

In this representation, the tabular function $\xi\left(J_{exp}, \sigma_{exp}\right)$ is reported in the new coordinates system θ, η.
The value of $\xi\left(J, \sigma\right)$ is then obtained as:

$$\xi\left(J, \sigma\right) = \sum_{i=1}^{4} N_i \xi(\theta_i, \eta_i) \tag{2.19}$$

with $\sum_{i=1}^{4} N_i = 1$ at any point inside the element and where N_i are the *four shape* function (or weights) given by:

$$\begin{aligned} N_1 &= \frac{1}{4}(1-\theta)(1-\eta) \quad N_2 = \frac{1}{4}(1+\theta)(1-\eta) \\ N_3 &= \frac{1}{4}(1+\theta)(1+\eta) \quad N_4 = \frac{1}{4}(1-\theta)(1+\eta) \end{aligned} \tag{2.20}$$

In other words, each point of the function $\xi\left(J, \sigma\right)$ is the weighted sum of the 4 nearest point of the tabular function $\xi\left(J_{exp}, \sigma_{exp}\right)$.

2.2 Model testing

2.2.1 Harvester prototype setup and modelling

The harvester prototype used for the model testing is a polycrystalline Fe81Ga19 sample (cubic grains with <100> easy axes) direct force harvester with a shape of a cylinder. With a length of 60 mm and a diameter of 12 mm, the cylindrical rod is then machined reducing the diameter down to 6 mm for a length of 53 mm, in order to host a 2000 turns pick-up coil with 32.6 Ω electric resistance. Figure 2.5a is the sketch of the 3D-model of the rod. In this prototype, the magnetic bias is generated by a couple of permanent magnets (PMs) placed at the extremities of the rod.

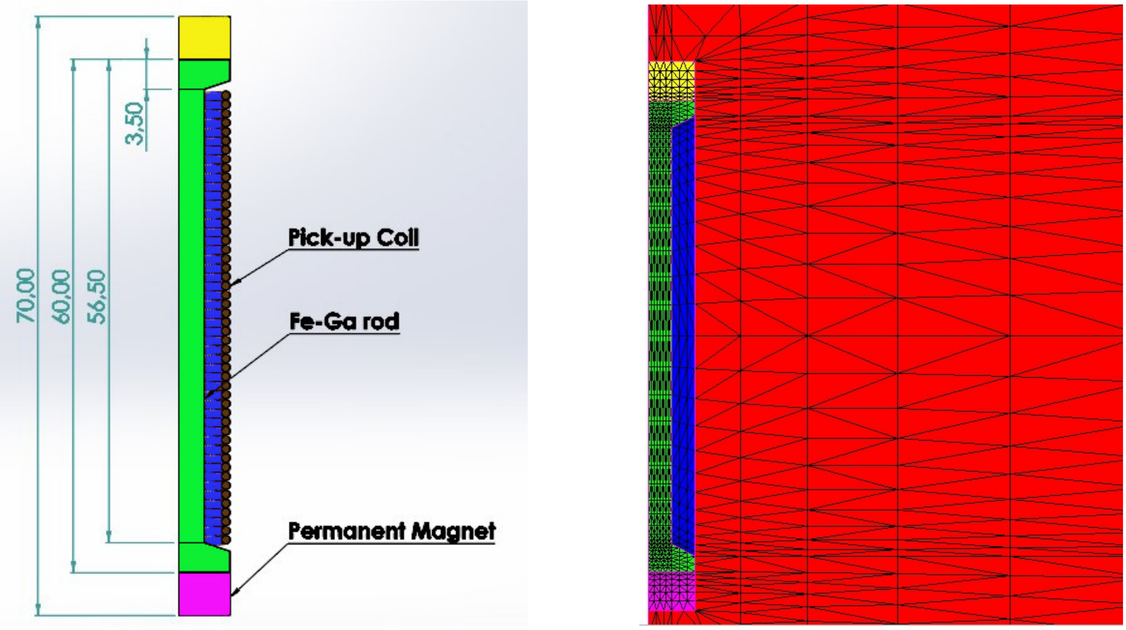

(a)

(b)

Figure 2.5: (a) The rod technical section draw. All the geometric dimensions are reported. (b) The 2D mesh of the longitudinal section of the rod. Each colour represent a different material: air (red), FeGa (green), coil (blue), permanent magnetsblue (violet and yellow). Image taken from [129].

From the technical draw it is possible to reconstruct the 2D mesh of the longitudinal section shown in Figure 2.5b

The axis-symmetric structure of the prototype is discretized into 2D triangular finite elements. A portion of the considered domain is shown in 2.5b, where each colour indicates a different material: air (red), Fe-Ga (green), pick-up coil (blu), PMs (yellow and purple).

The 3D assemble is obtained through a simple rotation over an axis of simmetry (in Figure 2.5b is the extreme left side of the picture).
Once that all the information is given to the model, the software gives back the solution, which is in particular the flux linkage on the pick-up coil. Coupling the result with the information of the electrical circuit, constituted at least by pick-up coil resistance and the load, the solver can also return directly the induced electromotive force and/or the current.

2.2.2 Model tuning

The definition of the FP constant ν is crucial to obtain a good correlation between the simulated data and the experiments. As already highlighted in the above section, the magneto-mechanic behaviour of the Fe-Ga alloy seems to not allow to use a unique and predetermined value, capable to ensure a relative fast and regular convergence of the solution. To verify how this could affect the results, a preliminary comparison is performed varying the mechanical preload σ_0 between 30 MPa and 70 MPa and applying a dynamical load of 8 MPa with a frequency of 100 Hz. The magnetic bias is given by the permanent magnets, and the relative magnetic behaviours are directly inserted into the model. The experimental pickup-coil has a resistance of 32.6 Ω, coupled with a load resistance of 160 Ω. The solver gives also the possibility to set externally both the FP constant ν and the maximum number of iterations for each instant. The model is initially verified imposing a maximum number of iterations per each time instant equal to 800 and two different value of ν: 50 and 3400. The results are shown in Figure 2.6.
The first information one can obtain, is that none of the two attempt show a good correlation with the experimental data.
At a deeper analysis, it is possible to observe that, on one hand, with $\nu = 50$ the simulated values are higher than the experimental ones, and on the other hand that with default value of ν the model gives back results lower than the measured ones. These informations lead to two aspect:

- by increasing the value of the constant ν, the simulated value decreases
- it is not possible to use a unique value of the constant ν for all the mechanical preload range

It seems that for each value of the mechanical preload it should be an ideal value of the constant ν, also if the maximum number of iterations given to the software may influence the results too. Increasing the maximum number of iterations, theoretically also up to infinity, could give the possibility to choose a unique value of the constant ν for all the value of the mechanical preload σ_0. But, in order to work in a low time-consuming regime, this is not an option. So, another possibility is to modify progressively the value of ν by means of a try and error process. To do

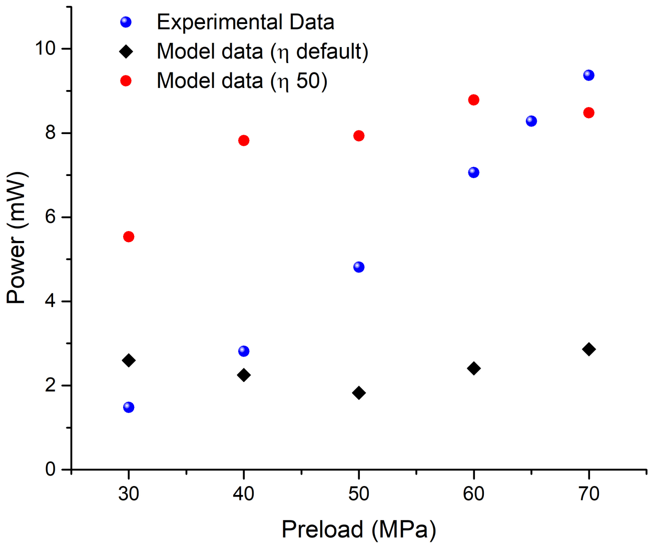

Figure 2.6: Preliminar comparison of the model with the experimental data for several values of mechanical preload and of constant ν. Image taken from [129].

so, there exist several methods, also using a set of experimental values to calibrate the model. If on one hand this could solve all the problem, on the other hand this could be a limitation, since each change on the experimental setup could require a new calibration curve. Another possibility is to analyse the convergence index expressed as L2-norm, as shown in Figure 2.7

When the FP constant ν approaches the ideal value for a particular value of σ_0, the convergence index $\epsilon \sim 0.4 \cdot 10^{-2}$, while if it is sensibly different from the ideal one, $\epsilon > 0.1 \cdot 10^{-1}$, and it is true both if the chosen value is greater or lesser than the ideal one. With $0.1 \cdot 10^{-2} < \epsilon < 5.0 \cdot 10^{-2}$ the result is still not the desirable one, but it could be enough to ensure a good correlation between the model and the experimental data. Another good reason looking at the convergence index, is that help to set the maximum number of iterations. Indeed, the choice of the correct FP constant is also affected by the maximum number of iterations. For example, let's focus on the mechanical preload $\sigma_0 = 70$ MPa, imposing $\nu = 50$, and observing the evolution of the convergence index by increasing the maximum number of iterations, as shown in Figure 2.8. From these results, it is possible to observe that with 3600 iterations are enough to reach the ideal convergence index value and to properly simulate the output power. But, on the other hand, it is clear that the required time for completing the simulation is 4 times higher than with just 800 maximum iterations. The information here obtained is that with higher value of iterations it is possible to obtain the convergence with a wider range of values of the

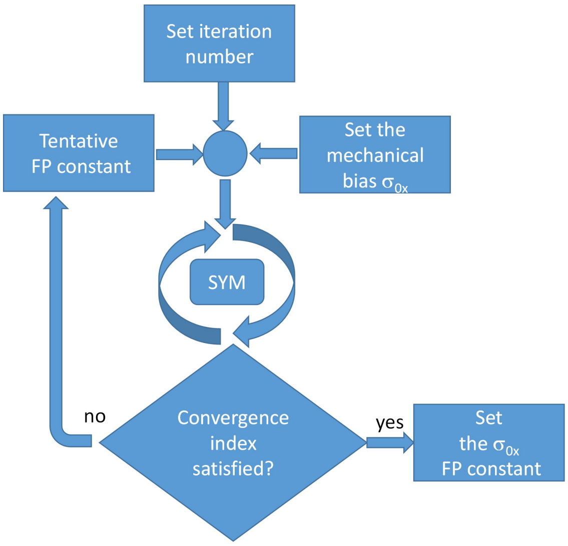

Figure 2.7: Scheme for the choice of the FP constant for a generic mechanical preload. Image taken from [129].

FP constant, but on the other hand it takes more and more time. 3600 maximum iterations here appear as a good compromise between the final result and the total time of the simulation.

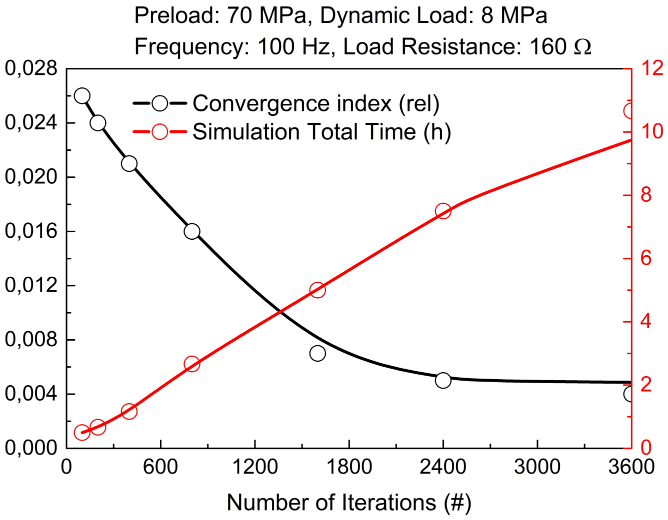

Figure 2.8: Evolution of convergence index and simulation time as a function of the number of iterations. Trend lines are just a guide for the eyes. Image taken from [129].

2.2.3 Results and discussion

After the correct identification and choice of the FP constant, the simulations lead to an excellent agreement with the experimental values of the output power transferred to the load, as shown in Figure 2.9.

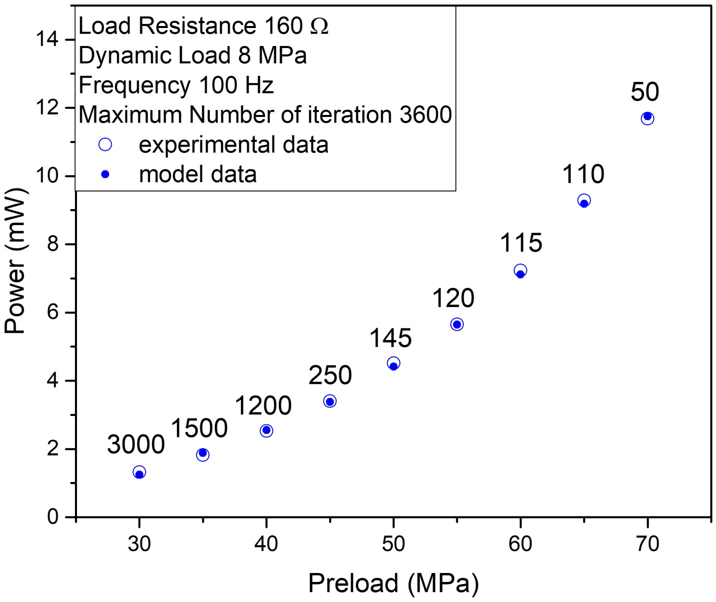

Figure 2.9: Final comparison of the model with the experimental data for several values of mechanical preload. For each point the label indicates the value of the constant ν. Image taken from [129].

At first this method requires a great number of simulation, and therefore a significant amount of time. But once the value of the constant ν has been identified for each considered value of σ the model is ready to be applied for any working condition of the device and the results seems to be quite good, as shown in Figure 2.9.

In Figure 2.10a, the model is compared with the experimental data varying the dynamic load (4 MPa up to 10 MPa) for 3 different preloads: 40 MPa, 50 MPa and 60 MPa. The frequency is equal to 100 Hz and the load resistance is 160 Ω. The results clearly show how the model is capable to predict the output power of the harvester also varying the dynamic load.

The second parameter analysed is the frequency. Since the first comparison was done with a frequency of 100 Hz (the higher value that the testing machine is capable to reach) 3 other frequency values were chosen: 20 Hz, 50 Hz and 80 Hz. The dynamic load is equal to 8 MPa and the load resistance is 160 Ω. Figure 2.10b shows a good overlapping between experimental and calculated data.

Again, it is possible to observe a good correlation between the model and the measurement results. As well known, the output power depends directly from the frequency.

Finally, it was also verified the ability of the model to simulate the load resistance effect on the output power (from 10 Ω up to 10 kΩ with constant dynamic load (8 MPa) and frequency (110 Hz). The simulation was repeated for three different preload value: 40 MPa, 50 MPa and 60 MPa. The dynamic load is equal to 8 MPa and the frequeny is 100 Hz. The results are shown in Figure 2.10c.

It is possible to observe a good correlation between simulations and the experiments, especially for load resistances higher than 100 Ω.

As expected, there exists an ideal load resistance which maximize the output power of the harvester, and which is equal to 60 Ω. For higher values, the current decreases too much, while for lower load resistances the output power decreases due to the low value of the output voltage. The analysis on the load resistance plays a fundamental role in the design of an energy harvester, since both the sensor and the rectifier circuit represent the load.

In conclusion, the analysis carried out in this thesis highlighted the applicability of the Preisach magnetomechanical model to galfenol. Compared to Terfenol-D model application, a sensitivity of the fixed point constant with respect to the preload was highlighted. An accurate tuning of the convergence of the model is therefore necessary at the preload variation. Once this tuning has been carried out, which involves an adjustment of the fixed point constant in order to obtain a good convergence index, a good agreement can be found between calculated and measured results. It has been shown that this agreement was maintained when the other electrical, magnetic and mechanical parameters change, such as the electrical load, the frequency of vibration, the magnetic bias or the amplitude of the vibration. The results obtained in this chapter have been recently published in [129].

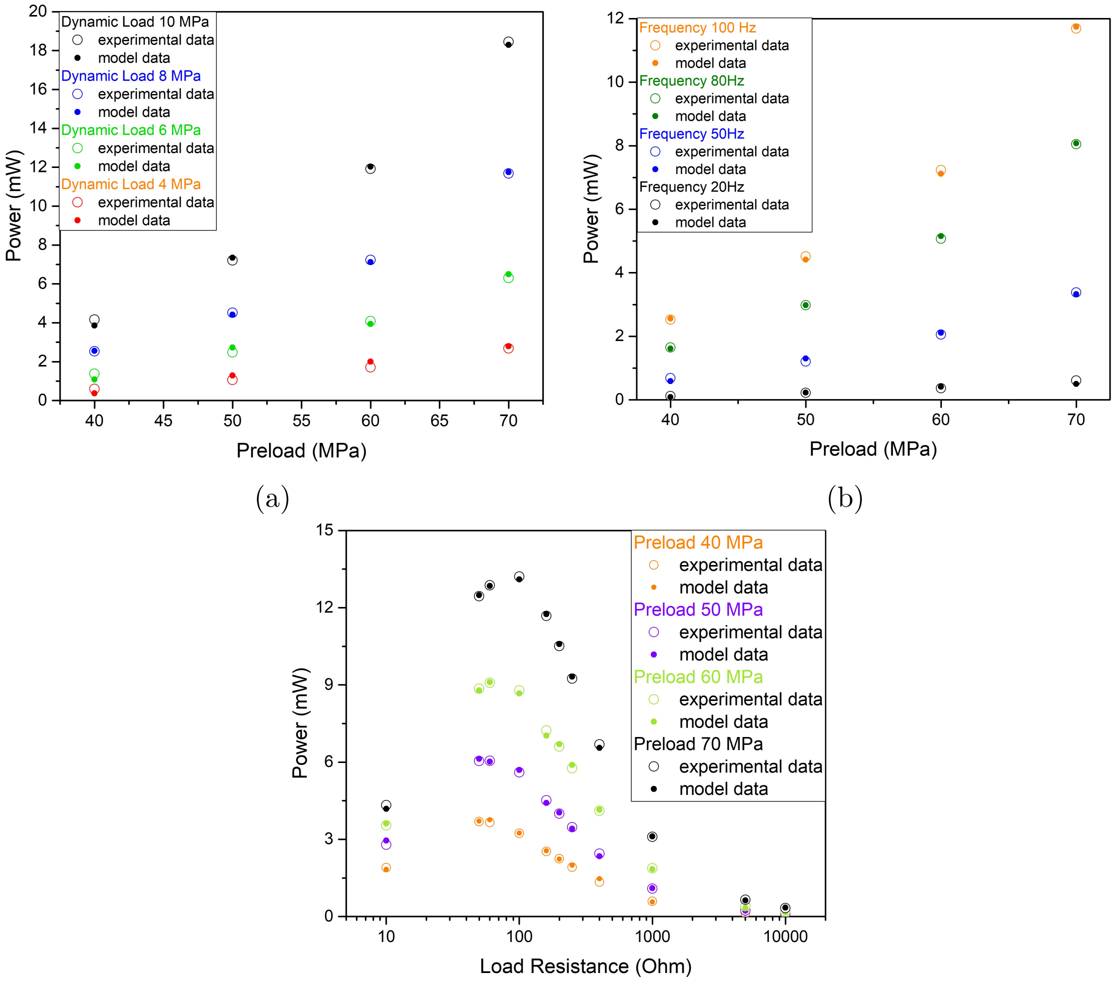

(a)

(b)

(c)

Figure 2.10: Comparison of the model with the experimental data for four different preloads (from 40 MPa up to 70 MPa) varying: (a) the dynamic loads (4 MPa up to 10 MPa) while the frequency is equal to 100 Hz and the load resistance is 160 Ω; (b) the frequency (20 Hz, 50 Hz, 80 Hz and 100 Hz) with a dynamic load equals to 8 MPa and the load resistance is 160 Ω; and (c) the load resistance (from 10 Ω up to 10kΩ having the dynamic load equal to 8 MPa and the frequency to 100 Hz. Images taken from [129].

Chapter 3

Galfenol figure of merit

3.1 Experimental setup

3.1.1 Description of the experimental setup

This section presents a special investigation of the interaction between magnetic bias and prestress in a direct force harvester excited with harmonic stress up to 100 Hz. A specific experimental setup has been realized, that is able to finely and continuously regulate both the magnetic as the mechanical bias, under dynamic excitation. The results have been developed in the framework of this thesis work and have been already published in [130]. In the following analysis a particular attention has been devoted to test repeatability and accuracy of the results. A part of the experimental analysis was also reported in [131].
A three-legged magnetizer has been designed in order to bring the galfenol up to saturation and in order to tune continuously the magnetic field bias. The magnetizer is shown in Figure 3.1a. It is made of Fe-Si laminations, 0.2 mm thick, cut in a L shape and glued together in 4 parts. The parts were then glued two by two, and then connected by two pure iron rings, drilled in the centre to allow the passage of the galfenol rod. The latter is milled in the central part, in order to allow the housing of the coil and, at the same time, the passage through the hole.
The magnetizer can be schematized into three principal components: (A) the four equal L-shaped elements constituting the yoke and the external limbs; (B) two 600-turns coils connected in series and wrapped around the external limbs; (C) the magnetostrictive element (details in Figure 3.1a).
Such a magnetizer is able to regulate the magnetization of galfenol rod (see [132]) applying a d.c. current of 6 A paired with a compressive stress of about 120 MPa. As can be seen in Figure 3.1b, the rod of galfenol is a cylinder of 3 mm radius in the center, which increases up to 6 mm at the two ends. This design is particularly indicated to place a pick-up coil wrapped around the magnetostrictive material, giving to the sample the appearance of a uniform cylinder. The correlation between the

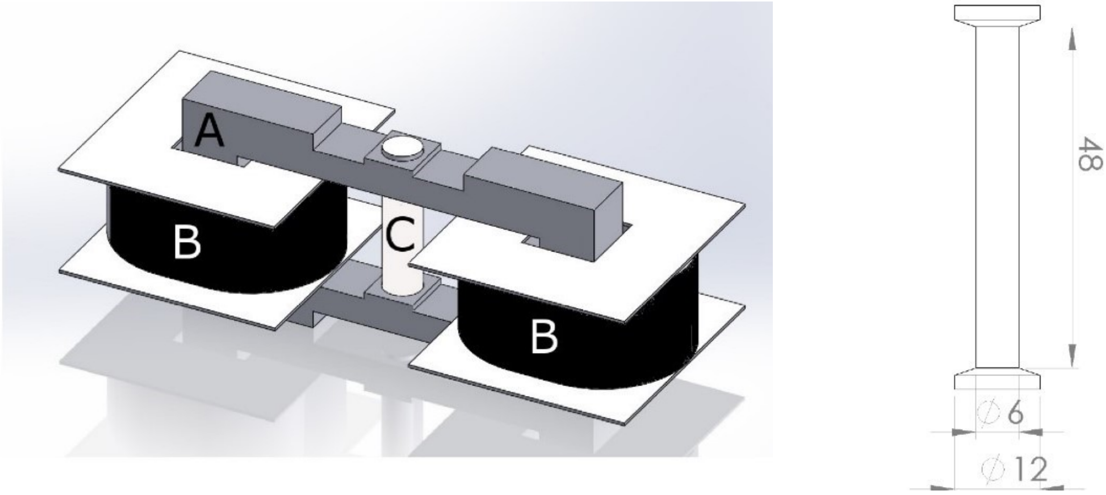

(a) (b)

Figure 3.1: (a) Three-legged magnetizer harvester: A) Fe-Si 0.2 mm lamination magnetic closure, B) excitation coils, C) magnetostrictive Fe-Ga rod. The overall dimensions of the yoke are 120 mm x 68 mm x 15 mm. (b) Fe-Ga rod section. Images taken from [130].

input current and the magnetic bias may be influenced by several parameters. The use of a Hall probe (Lakeshore 460, Lake Shore Cryotronics, Inc, Westerville, OH, USA) located next to the magnetostrictive material to measure the magnetic field bias, guarantee reproducibility of the bias tuning the excitation current.
In order to apply a well-known and reproducible mechanical stress, in the thesis work a fatigue-testing machine (Instron, model E10000, Instron Corp., Norwood, MA, USA) was adopted. This machine represents a versatile solution to produce and control a sinusoidal mechanical vibration, in which the mean value represents the mechanical prestress. The machine control is able to maintain constant the previously set prestress while the sample undergoes dynamic excitation.
The magnetizer is controlled by a signal generator (Agilent 33220A, Keysight Technologies, Santa Rosa, CA, USA) and a Kepco amplifier (BOP 72-6ML, Kepko Inc. Flushing, NY, USA). The dynamic testing machine uses a control software (Instron Console and WaveMatrix software, Instron Corp., Norwood, MA, USA) to set the test parameters, such as mechanical preload (σ_0) and vibration amplitude ($\Delta\sigma_{\mathrm{pk}}$), show the control measurements and diagrams and, if needed, save the data. The scheme of the whole system (Figure 3.2a) and a picture of the device in the testing machine (Figure 3.2b) are reported.
Finally, a programmable resistor (Pickering PXI 40-297- 002 programmable precision Resistors, Pickering Interfaces Ltd., Clacton-on-Sea, Essex, UK) represents the passive load and is measured, together with other electrical parameters, by a Yokogawa WT 3000 power analyser (Yokogawa Electric Co., Musashino, Tokyo,

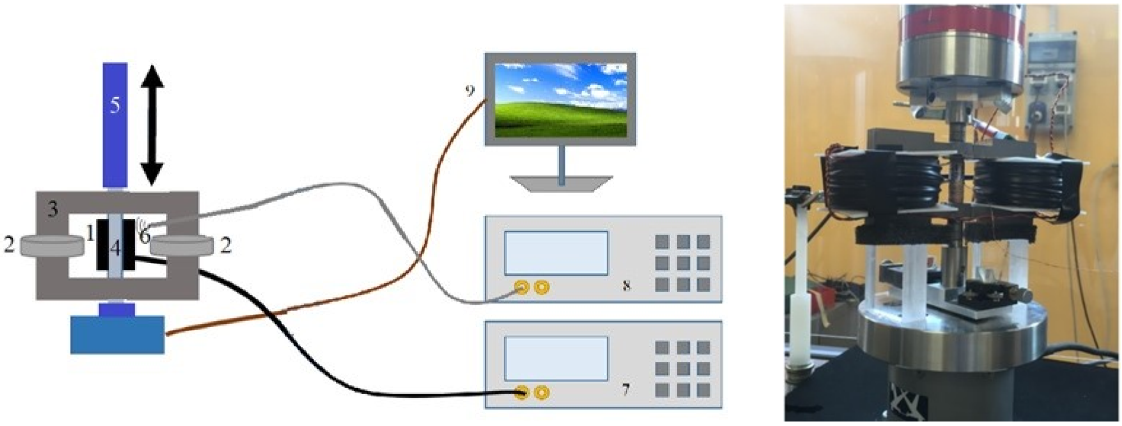

(a) (b)

Figure 3.2: (a) Scheme of the measurement system. 1) Harvester pick-up coils, 2) Excitation coils, 3) Closure yoke, 4) galfenol rod, 5) Test machine moving spindle, 6) Hall sensor, 7) Measuring system including programmable load resistors, 8) Mainframe Hall meter, 9) Control of the test machine including mechanical bias control and vibration amplitude. (b) Picture of the device inserted in the test machine. Images taken from [130].

Japan).

3.1.2 Metrological characterization of the force test machine

The 10 kN peak force testing machine Instron Pulse E10000 used to apply the mechanical stress underwent a preliminary metrological characterization in accordance with the ISO 7500-1 [133], using the primary force standard (ISO 376 [134]) of the Italian National Metrological Research Institute (INRiM). The characterization started from the lower value of 1 kN rms (about 14% of the machine nominal rms load) up to the nominal one of 7 kN rms. The measurement points corresponding to an applied continuous load are reported in Table 3.1.
The signal was acquired with a Digital Precision Amplifier DMP40, which also supply the internal extensometers of the National Force Standard. The main characteristics are summed in Table 3.2.
The procedure ISO 7500-1:2016 [133] indicates that for each generic force F_i applied by the force machine, the real value F, coming from the primary force standard, must be noted. Before starting the metrological characterization, it is also required to perform a general visual inspection, as reported by the ISO 7500-1:2016 [133] Annex A. This inspection was conducted in three different phases: (i) a visual inspection to verify that the machine does not present any signs of wear or even minor

Table 3.1: Measurement points of the metrological characterization

Force (N)
1000
1500
2000
3000
4000
5000
6000

Table 3.2: DMP40 parameters

Parameter	Value
Voltage	5 V
Frequency	225 Hz
Reading format	mV/V
Sensibility	10^{-6} mV/V
Full-scale	2.5 mV
Anti-aliasing filter	Bessel
Filter cutting frequency	0.1 Hz

damage to its structure and that it is isolated by any external factor (as mechanical vibration, electrical or temperature interferences, and so on); (ii) then it comes the inspection of the machine structure, in order to verify that bot the structure as the gripping system guarantee the force is applied uniaxially; (iii) finally the load beam is inspected. At the end of this inspection, a preload equal to the nominal load of 7 kN was applied, each time for 3 minutes.

At this point, a preliminary measurement was executed in order to find any systematic error to correct before the characterization. Table 3.3 summed up the results.

As can be seen from the results, it seems that the applied force value seen by the machine system is lower than the real one, with an increasing trend as the load increases. It is possible to define a mean systematic error ε equal to -0.97 %. The trend of the relative difference for each discrete value of applied force was reported in Figure 3.3.

Correcting the value reported by the machine of the systematic error ε, the relative difference between the error and the real force indicated by the primary sample was recalculated. The results are thus reported in Table 3.4.

In this way, it was possible to improve the relative difference by an order of magnitude, and it is now possible to start the calibration.

Table 3.3: Relative accuracy of the applied force

Applied force F_i (N)	Real value F (N)	Relative difference %
1000	1007.8	-0.77
1500	1513.5	-0.89
2000	2019.2	-0.95
3000	3030.6	-1.01
4000	4041.6	-1.03
5000	5052.8	-1.04
6000	6061.8	-1.02

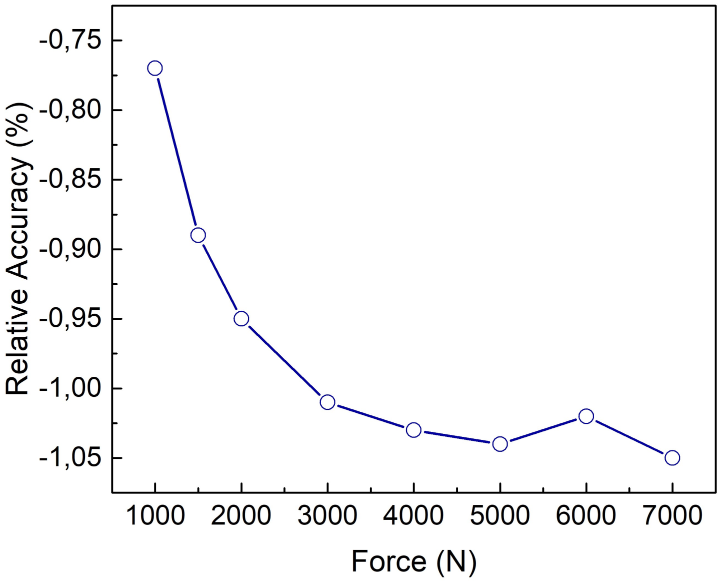

Figure 3.3: Relative accuracy for each discrete value of applied force

The force levels are then measured in different angular positions, rotating the force transducer on the support base and taking care not to change its position with respect to the vertical direction of application of the force. The various force levels are applied to the force transducer according to an increasing sequence of values. Once a starting angular position has been defined, called 0° position, two measurement cycles and one cycle are performed, respectively, in the 120° and 240° position. At each load application, including the absence of load, the reading value is recorded after thirty seconds.
During the elaboration phase, just the second range of value for 0° position is considered for the repeatability evaluation. Indeed, the first cycle is applied only to exercise the elastic element and minimize undesired effect due to the force transducer. All the results are presented in the following Table 3.5.

Table 3.4: Effects of calibration on relative accuracy

Applied force F_i (N)	Real value F (N)	Relative difference %
1009.7	1007.8	0.19
1514.5	1513.5	0.07
2019.4	2019.2	0.01
3029.1	3030.6	-0.05
4038.8	4041.6	-0.07
5048.5	5052.8	-0.08
6058.2	6061.8	-0.06

Table 3.5: Force values recorded during calibration

Applied force F_i (N)	Real value F (N) 0°	Real value F (N) 120°	Real value F (N) 240°
1000	999.9	999.8	1000.0
1500	1500.1	1500.0	1499.1
2000	2000.3	1999.8	1999.4
3000	3000.8	2999.8	3000.1
4000	4000.8	3999.8	4000.1
5000	5000.8	4999.6	5000.5
6000	5999.8	5995.1	5998.8
7000	6999.7	6997.7	6999.9
0	-0.04	-0.05	-0.02

The ISO 7500-1 [133] also provides indication on how evaluate the results. During the elaboration phase, for each value of applied force Fi it has been evaluated the mean value of the real force applied.
Relative accuracy q has been calculated as:

$$q = \frac{F_i - \bar{F}}{\bar{F}} \times 100 \tag{3.1}$$

For each discrete value of force, the difference between the maximum and the minimum measured values is indicated as the relative repeatability error b, and is calculated as:

$$q = \frac{F_{max} - F_{min}}{\bar{F}} \times 100 \tag{3.2}$$

Furthermore, it is recorded the relative resolution related to each discrete value of force, given by:

$$a = \frac{r}{F} \times 1000 \tag{3.3}$$

where r is the resolution of the conditional signal recorder expressed in newton. At the end of each cycle, the final value F_{i0} is recorded. Been F_N the maximum value recorded, the relative zero error for each measurement cycle is equal to:

$$f_0 = \frac{F_{i0}}{F_N} \tag{3.4}$$

For each discrete value of force presented in Table 3.5 the indices shown below have been calculated. For the purpose of classifying the force testing machine, the highest value was considered for each index. In Table 3.6 these indexes were transcribed together with the machine classification.

Table 3.6: Characteristic values of the force measurement system.

Accuracy q	Repeatability b	Zero f_0	Relative resolution a	Machine classification
-0.00711	0.066679	-0.00071	0.1	0.5

The Instron Force Testing Machine can be so classified as class 0.5, the best result achievable by a commercial device of this type.

3.1.3 Friction and misalignment issues

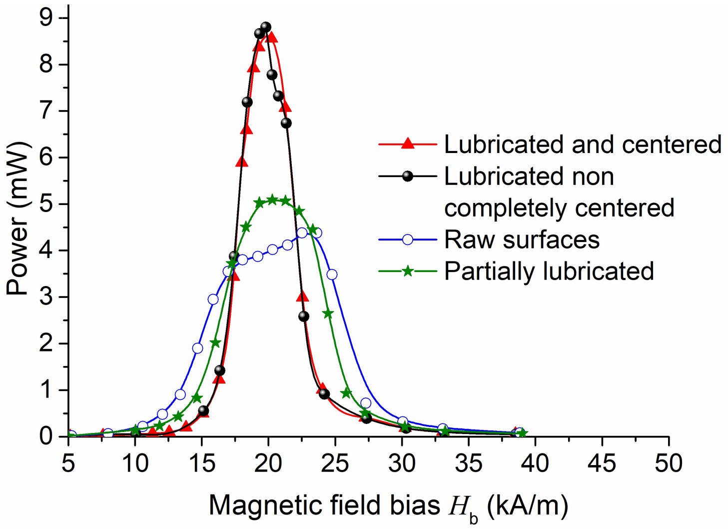

Figure 3.4: Output power versus the applied magnetic field bias. Preload at 90 MPa. Vibration amplitude 4 MPa. Frequency of the vibration 100 Hz. Effect of friction and misalignment on the measurement results. Image taken from [130].

It was therefore established that the test machine accuracy is of the order of per thousand, and therefore higher magnitude repeatability issues cannot be attributed to the test machine. From the very first measurement, it comes out that friction and misalignment lead to significant repeatability issues. So that, they must be taken into consideration, as well represented in Figure 3.4.
Figure 3.4 shows the behaviour of the output power of the device with coils described in sect. 3.1, versus the magnetic bias. Through the coils it was possible to vary seamlessly the magnetic bias, keeping constant the instantaneous magnetic bias and the dynamic load through the test machine. Up to now, in literature only discrete values of magnetic bias can be found, usually applied through permanent magnets in a limited range. Figure 3.4 shows a complete behaviour, which is strongly affected by friction.
In order to obtain reproducible results, it is necessary lubricate the rod inside the magnetizer. But it could not be enough. Even the misalignment affects the reproducibility of the results. Therefore, it becomes important to centre in the best way possible the rod under the testing machine, in order to apply a uniaxial force. When a sample is well lubricated and perfectly positioned under the testing machine, the results of Figure 3.5 can be achieved with an high repeatability.

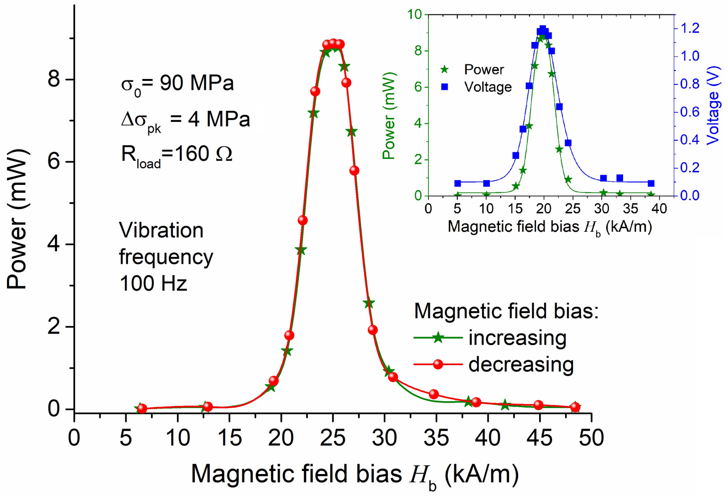

Figure 3.5: Output power versus magnetic field bias, increasing and decreasing the latter and keeping constant the amplitude of the vibration excitation and of the mechanical preload. The inset shows, in comparison, the output voltage and power. Image taken from [130].

In laboratory it was finally possible to obtain a nearly perfect results in terms of repeatability increasing and decreasing the magnetic bias, while the sample was undergoing mechanical bias and dynamic mechanical excitation. Figure 3.5 shows how the results are almost superimposed with differences between the two peaks values lower than 1%.

The curve can be described by an axisymmetric peak function, belonging to Gaussian family, as:

$$P(H_b) = y_0 + \alpha P_{Max} \cdot \left(1 + e^{-\frac{H_b - H_c + w_1/2}{w_2}}\right) \cdot \left[1 - \left(1 + e^{-\frac{H_b - H_c - w_1/2}{w_3}}\right)\right] \tag{3.5}$$

where y_0 is an offset parameter having a value much less than 1 mW. The parameter α depends on the mechanical preload with a value, in our experience, between $0.7 \leq \alpha \geq 1.0$. P_{Max} is the maximum output power in mW, i.e. the peak of the curve, while H_c is the value of the bias field expressed in kA/m corresponding to P_{Max}. Finally, w_1, w_2 and w_3 are weights of the interpolator expressed in kA/m.

3.2 Experimental results with magnetizer

3.2.1 Combined effect of mechanical and magnetic bias

The combined use of a force testing machine and of a magnetizer, lead to the possibility to deeply analyse the combined effect of mechanical and magnetic bias on the output performance of a magnetostrictive device. The main result of this experimental campaign is presented in Figure 3.6.

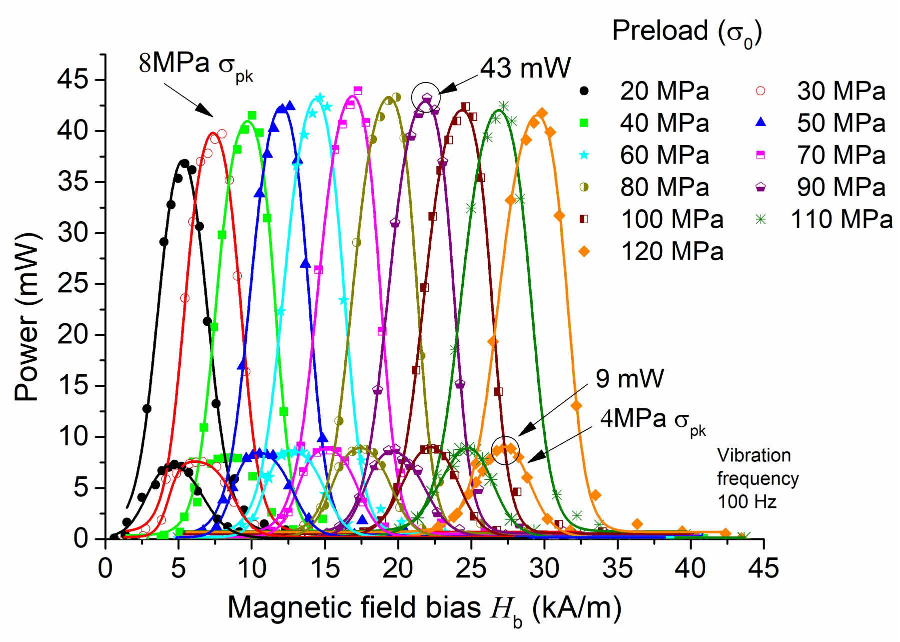

Figure 3.6: Output power versus the magnetic field bias for different values of the mechanical preload and two values of the vibration amplitude. Dots represent the measurements points. Solid lines are the fits according to eqn 3.5. Image taken from [130].

Here the behaviour of the output power versus the magnetic bias is shown. The frequency of the dynamic load is equal to 100 Hz, and it was used a load resistance close to matched load, equal to 160 Ω. Two curve families are shown, characterized by two different dynamic load value (4 MPa and 8 MPa), where each colour represents a different mechanical preload.

The main result underlined by Figure 3.6 consists of the experimental demonstration that for each mechanical preload it exists a particular magnetic bias able to maximize the output power of the harvester. On the other hand, this result clearly demonstrate that for each value of magnetic bias it is possible to maximize the output power simply matching the mechanical preload. For applications, it is interesting to notice that for lower values of magnetic bias, it is possible to obtain a

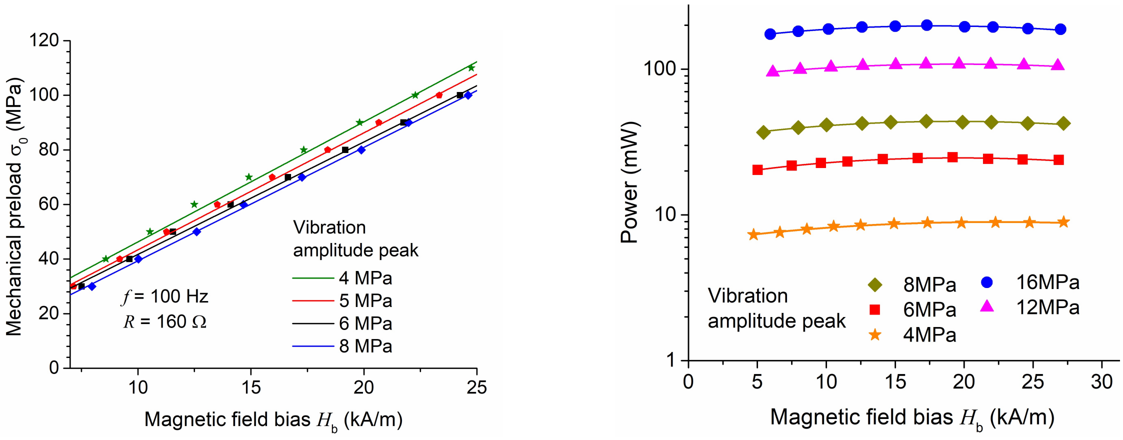

(a) (b)

Figure 3.7: (a) Mechanical preload versus magnetic field bias of the maximum output power values (see Fig. 6 for vibration amplitudes peaks of 4 MPa and 8 MPa) and (b) maximum output power versus the magnetic field bias for different preload values (labels near symbols). Curve families obtained by varying the vibration stress amplitude. Frequency of the vibration 100 Hz. Images taken from [130].

maximum output power close to the highest one (about 37 mW vs 43 mW). It is an interesting result, since permanent magnets usually provide a limited magnetic bias in a device. Finally, as well known, it can be noted that doubling the dynamic force, the output power increases by a factor 5 (9 mW vs 43 mW) following an exponential trend. All the curves in Fig. 6 can be interpolated with the formula 3.5 presented above. As far as the interpolating coefficients are concerned, see Table 3.7.

Another remarkable outcome of the experimental survey can be found drawing-up the couple *mechanical preload versus the magnetic bias* which maximize the output power. It is possible to verify that exist a liner correlation between them, as presented in Figure 3.7a.

The figure presents a curves family in which the dynamic load was variated. This could be a useful result during the design phase, since it gives back immediately which are the best value of mechanical preload to maximize the output power starting from the magnetic field bias, and vice versa. However, Figure 3.6 shows that the output power is not constant. Even when the mechanical preload match ideally the magnetic field bias, the maximum output power is limited for lower values of the magnetic bias. Therefore, in the case the choice of the magnetic bias is not an issue, it could be interesting to verify the trend of the maximum available output power as function of preload and magnetic bias. Figure 3.7b shows the results.

3.2.2 Effects of the load resistance

Up to here, we have discussed how the output power in the analyzed device is a function of some parameters such as: positioning and centering accuracy of the rod in the device, friction, mechanical and magnetic bias and vibration amplitude. A well-known parameter that is missing is the load impedance, which significantly affect the output power. As is known, the impedance is coupled when the load and impedance of the device matches (mainly the coil impedance in the device), with in addition a magneto-mechanical term that varies with the operating conditions. This is highlighted by the diagram in Figure 3.8 where, for sake of clarity, the coordinate axis is expressed in a logarithmic scale.

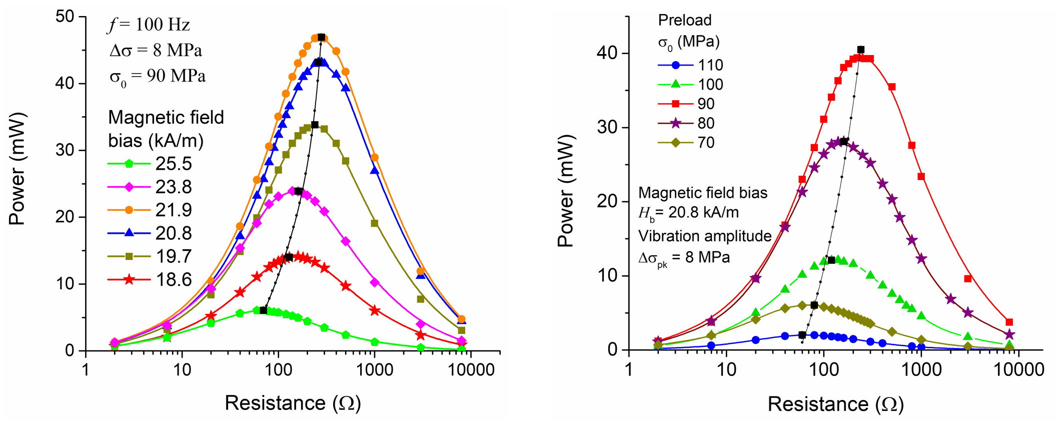

Figure 3.8: Output power versus the load resistance values. Frequency of the vibration 100 Hz. Curve family obtained varying: a) the magnetic field bias and keeping constant the mechanical preload at 90 MPa; b) the mechanical preload and keeping constant the magnetic bias at 20.8 kA/m. Image taken from [130].

Here, in the two graphs the curves are obtained varying the magnetic field bias (Figure 3.8a) or the mechanical preload (Figure 3.8b). In both cases, it is evident that the output power vs the load resistance has a maximazing resistance value.
It is also important to underline how the output voltage must be conditioned in order to transform the AC signal to a DC signal suitable for the storage element (battery or supercapacitor). This ask for a rectifier bridge, which requires a minimum value of voltage to work, usually at least one volt. Therefore, there could be the case in which it is convenient have a decreased value of output power and a significant increase in the output voltage. The results are summed up in Figure 3.9.

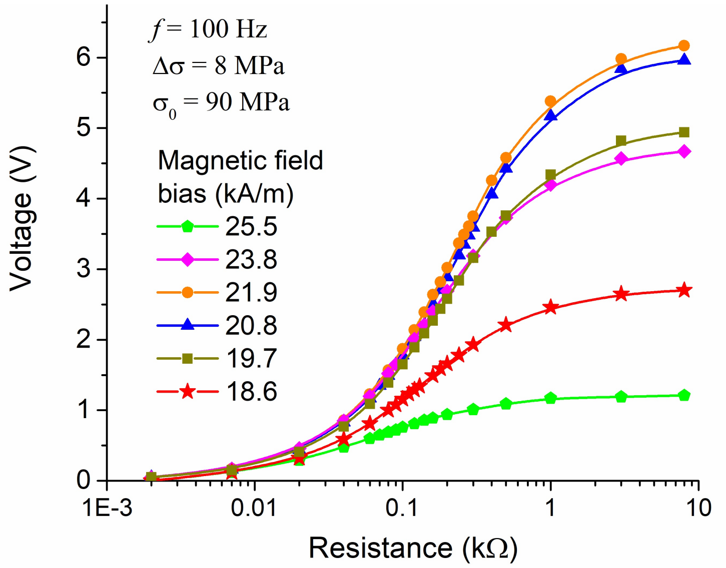

Figure 3.9: Output voltage versus load resistance. Curve family obtained varying the magnetic bias and keeping constant the mechanical preload at 90 MPa. Image taken from [130].

3.3 Experimental validation with permanent magnets

The use of the magnetizer has made possible to deeply analyse the combined effect of prestress and magnetic bias. Nevertheless, the results may not be complete, as the need to externally power the magnetizer is in contrast with the primary purpose of a harvester. To overcome this issue, and make consistent the results obtained through the experimental survey, the two yokes with permanent magnets of Figure 3.10 has been realized.

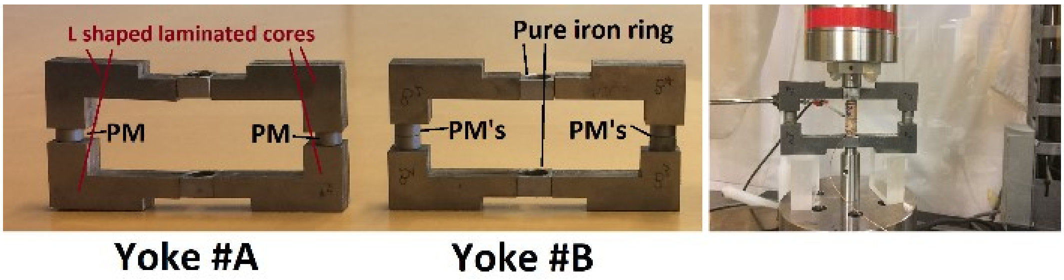

Figure 3.10: Magnetic yokes with 2 (Yoke #A) and 4 (Yoke #B) permanent magnets. On the right side, yoke #B in the testing machine. Image taken from [130].

The two yokes are a faithful reproduction of the magnetizer. The two columns have been shortened in order to obtain the same length of the columns including one magnet per column (Yoke #A) or two magnets per column (Yoke #B).Now the magnetic field bias is provided by permanent magnets and no more by a pair of coils. Since the magnetic bias is constant, it is possible to regulate the dynamic stress and the preload. As a preliminary working assessment, the two yokes were employed to test the output power varying the mechanical preload, as reported in Figure 3.11.

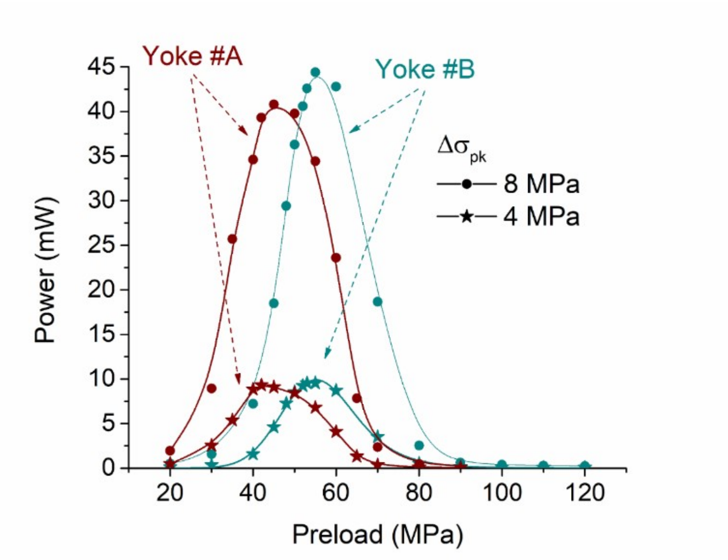

Figure 3.11: Output power versus preload. Curves obtained varying the preload for two different values of the vibration amplitude. Vibration frequency is 100 Hz. Load resistance 160 Ω. Image taken from [130].

To make the results more general, two different vibration amplitude (4 and 8 MPa) were applied, while using both yokes it was possible to impose two different magnetic field bias. The vibration frequency and the load resistance were kept constant and respectively equal to 100 Hz and 160 Ω, in order to reproduce the same conditions of the measurements with coils. As already seen, for a given value of magnetic field bias it exists one ideal value of mechanical preload which maximize the output power. For higher value of the magnetic field bias, the mechanical preload must be increased in order to match the new magnetic condition of the rod. With this preliminary test, most of the main results showed in the experimental campaign has been confirmed. Even the maximum value of the output power is in line with the results of Figure 3.6. This means that the experimental analysis conducted with the magnetizer can be extended also to permanent magnets. Moreover, a pair of permanent magnets is enough to provide more than 40 mW, close to what provided by the magnetizer. The issue now is to verify if the results obtained with the magnetizer can be used to design the harvester, or if there are relative differences in the output performances using the magnetizer or permanent magnets. A comparison between the results obtained with the magnetizer and with permanent magnets is shown in Figure 3.12.

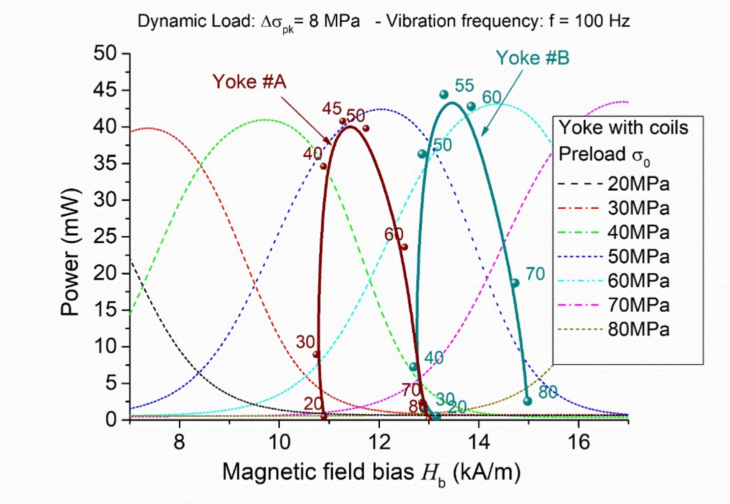

Figure 3.12: Measured output power versus magnetic bias. Curves obtained varying the preload (labels in MPa). Vibration amplitude $\sigma_{pk} = 8$ MPa. Frequency 100 Hz. Load resistance 160 Ω. The dotted curves are the ones measured with the yoke with coils and shown in Figure 3.6. They are reported here for comparison. Image taken from [130].

The solid lines in Figure 3.12 represent the result obtained with permanent magnets, while the dotted lines refer to the yoke with coils.
It is possible to highlight a few points:

- the magnetic field bias given by the permanent magnets is not constant, but varies with the preload from 11 kA/m to 13 kA/m for the configuration #A and between 13 kA/m to 15 kA/m for the configuration #B;
- the power values obtained at a given preload, are close to the corresponding curves at the same preload measured with the yoke with coils.

Therefore, it is possible to state that the experimental survey conducted with the use of the magnetizer can be used also in the designing of a vibration harvester provided by the same magnetic yokes, but with permanent magnets instead of coils.
Finally, using only the yoke #B, in Figure 14 it is analysed the output performance increasing the dynamic load.
As expected, the output power follows a cubic trend respect the vibration amplitude value. On the right scale of the graph, the output power is expressed in terms of specific power. In this way, it is possible to verify that just with a dynamic load

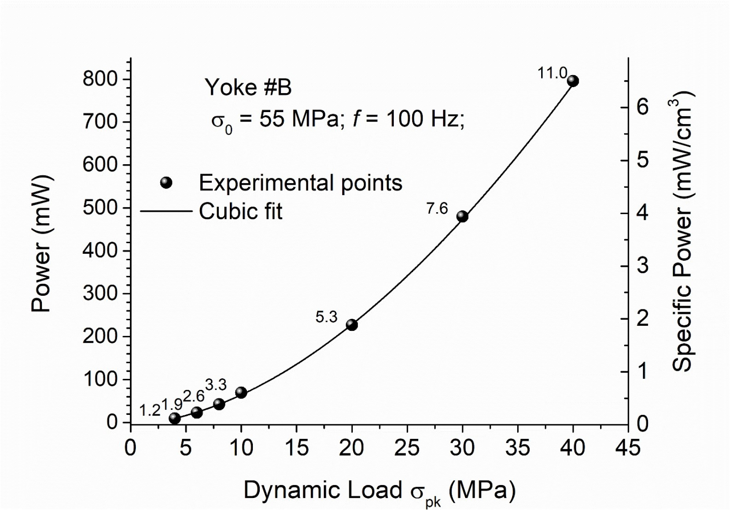

Figure 3.13: Measured output power and specific power versus the applied dynamic load. Curve related to the yoke with permanent magnets (yoke #B). Frequency 100 Hz, mechanical prestress 55 MPa. The labels near the experimental points represent the measured output voltage in volt. Image taken from [130].

around 15 MPa it is possible to reach a specific power equal to 1.0 mW/cm^3, which is starting to be interesting for applications.

In conclusion, the simultaneous use of a material testing machine and of a magnetizer lead to a complete study of the combined effect of prestress and magnetic field bias. The experimental survey provided a series of family curves which can be useful for guiding the design of an EH device, also providing an indication of which characteristics to be reproduced using a numerical model, for design purposes.

Table 3.7: Figure 3.6 curves fitting parameters

$\Delta\sigma_{pk}$ MPa	σ_0 MPa	y_0 mW	H_c kA/m	P_{Max} mW	α	w_1 kA/m	w_2 kA/m	w_3 kA/m
8	20	0.63	0.53	44.92	0.83	0.33	0.08	0.08
8	30	0.68	0.73	42.98	0.92	0.39	0.07	0.06
8	40	0.37	0.96	43.44	0.94	0.42	0.07	0.06
8	50	0.42	1.19	46.59	0.91	0.41	0.08	0.06
8	60	0.52	1.42	47.40	0.91	0.42	0.08	0.06
8	70	0.49	1.67	46.57	0.93	0.44	0.08	0.06
8	80	0.56	1.91	45.75	0.94	0.45	0.08	0.06
8	90	0.56	2.16	45.31	0.95	0.46	0.08	0.06
8	100	0.53	2.41	44.29	0.95	0.48	0.08	0.06
8	110	0.75	2.67	44.98	0.93	0.48	0.09	0.07
8	120	0.69	2.92	44.47	0.94	0.48	0.09	0.06
4	20	0.07	0.47	8.48	0.85	0.38	0.07	0.09
4	30	0.19	0.65	7.66	0.99	0.44	0.04	0.07
4	40	0.11	0.83	7.88	1.00	0.51	0.05	0.07
4	50	0.17	1.07	8.88	0.95	0.42	0.05	0.07
4	60	0.18	1.29	9.11	0.95	0.42	0.05	0.07
4	70	0.18	1.52	9.35	0.93	0.42	0.06	0.07
4	80	0.17	1.75	9.66	0.92	0.42	0.07	0.07
4	90	0.17	1.98	9.67	0.91	0.41	0.07	0.09
4	100	0.17	2.22	10.60	0.84	0.38	0.08	0.08
4	110	0.14	2.47	12.39	0.72	0.32	0.11	0.08
4	120	0.14	2.72	12.83	0.70	0.31	0.11	0.08

Chapter 4

Chemical - physical analysis of Si-FLG nanocomposite anode material

4.1 Silicon as anode material for Lithium Ion batteries

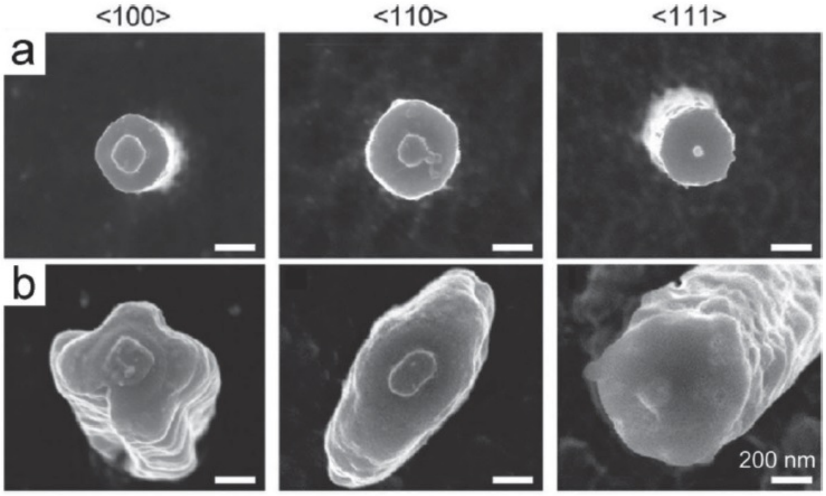

Figure 4.1: SEM images demonstrating anisotropic lateral expansion upon lithiation of crystalline Si nanopillars with three different orientation (<100>,<110> and <111>). a) pristine pillars and relative axial orientation. b) Fully lithiated pillars. Taken from [135].

Silicon represents one of the most promising materials to use as anode for Li-ion batteries [136, 137, 138, 139]. Silicon can react electrochemically with Lithium through an alloying reaction, which theoretically, can lead to the formation of Li4.4Si with a corresponding specific capacity of 4200 mAh/g [140]. However, the redox processes (the electrochemical lithiation/delithiation) leads to a significant volume changes ($> 300\%$) [141], due to the insertion of Lithium ions in the bulk Si. This large volume change leads to a fracture in the bulk Si, resulting also in a significant capacity decay in Si anodes [142]. Through SEM imaging [135], the volume expansion was observed after a potentiostatic lithiation. It was demonstrated that different axial orientation leads to different expansion, as can be seen in Figure 4.1. It was observed that the nanopillars expanded into cross, ellipse and hexagonal shapes, demonstrating that the volume expansion occurs along <110> directions, perpendicular to the nanopillar axis. The average overall volume expansion ratios of the pillar were also measured, resulting to be approximately 240%, 270% and 260% respectively [135].

An appreciable direct effect of the volume expansion is a poor cycling performance [142]. Moreover, the volume expansion affects negatively the electrode-electrolyte interface [106]. This results into the exposure of fresh electrode surface (during the expansion phase) and the consequent continuous electrolyte reduction during the cycling.

4.1.1 Lithium insertion in bulk Silicon

The effects of the lithiation in bulk Si are the main issue hindering the implementation of Si-based anodes in commercial batteries [143]. The Silicon atoms arrange in solid with a sp^3 hybridisation, resulting in a diamond-like crystal lattice, as shown in Figure 4.2, where the tetrahedral (Td), hexagonal (Hex), anti-bonding (A), bond-center (B), center of the second nearest silicon (C), and midway (M) sites between Hex site and B site are represented.

During the lithiation process, Li acts like a bad donor occupying an interstitial site rather than a substitutional one. Once inserted in the bulk Si, the Li defects have long-range diffusion processes occurring in a *zig-zag* manner, since they are continuously repelled by a host Si atom.

The electronic band structures for bulk Si does not change much its shape when the Li dopant is located on the Td and Hex. On the contrary, the Fermi level is moved to the bottom of conduction band, indicating a metal-like behaviour of the Li-doped Si material [144].

It is possible to identify different non-equivalent insertion positions in the Si lattice, each one with the relative binding energy, summed in Table 4.1.

Lithium can be seen as a substitutional (S) defect, when it is placed on a Si lattice site, or as a Frenkel defect (F), when it is positioned on the original Si site while the Si atom is repelled to an adjacent Td site. S and F defects indicates again that the Li dopant acts as an interstitial impurity. The relative negative binding energy indicates that the system becomes less stable after Li insertion. Table 4.1 clearly

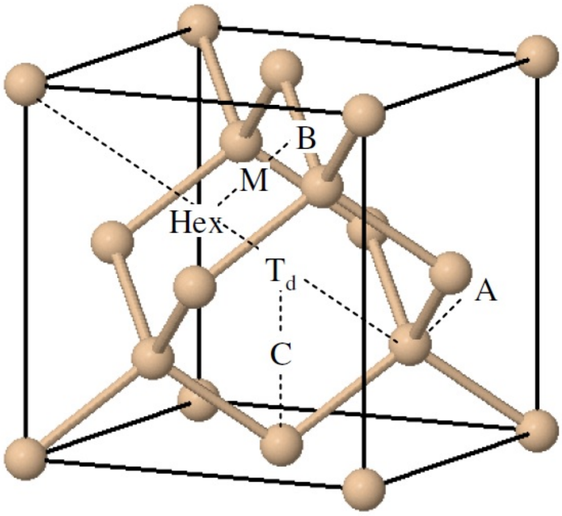

Figure 4.2: The Td, Hex, A, B, C, and M sites in bulk Si with a diamond structure. Image from [144].

Table 4.1: The binding energies of single Li dopant in bulk Si. Data taken from [144].

Position	Binding Energy (eV)
Td	1.359
Hex	0.847
B	-1.176
S	-6.602
F	-2.392

shows that the Td site is the most stable position, while the Hex site is a transition state. The ascent energy contribution due to the distortion of the closest Si shell around the defect and the descent one due to attractive interaction stemming from electron transfer between the impurity and its neighbouring Si atoms result in this site preference. Another way to explain it, is the study of the Si-Li bond-length. Despite Li atoms have only one valence electron, they also have large ionic radius. Therefore, Li atoms stay further away from the host atoms in closely-packed bulk Si. The longest and the second longest Si–Li bond lengths are, respectively, Td sites and Hex sites. Finally, B sites represents a non-stable position due to their negative binding energy. B sites are occupied by Li defects at high temperature only when an adjacent vacancy is present [145].

By inserting more Li atoms into Si supercells, Li impurity atoms will continuously occupy the Td sites until no Td voids are available in bulk Si. In a first approximation, the undestroyed host lattice should retain a ratio of [Li]/[Si] from x = 0-1, since each Si atoms hold only one Td sites. However, amorphization occurs at a ratio of [Li]/[Si] as low as 0.1 [146], and the Si-Si bond may be broken also at low Li doping concentrations.

At low doping region Li atoms are all located on the Td sites. Since the distance between two nearest Td sites (2.61 A), is smaller than a Li-Li bond length in Li metal (3.05 A), two Li atoms will repel each other if they occupy two adjacent Td sites. It comes that Li atoms incline to separate from each other, forming isolated impurities in bulk Si, and a homogeneous doping distribution is expected.

With the insertion of more Li dopants, a clear local structure distortion occurs, which destroys the homogeneous arrangement of the six-member ring in perfect crystalline Si (see Figure 4.3a). One five-member ring and one seven-member ring appear around the Li dopants and Si-Si bonds can be broken and reformed frequently. As a result, Li dopants change behaviour from repelling each other to gathering together.

At high doping concentration, the host lattice is significantly destroyed with respect to its diamond-cubic symmetry as well as short-range order. A typical distorted structure with the lowest energy is shown in Figure 4.3b after full relaxation.

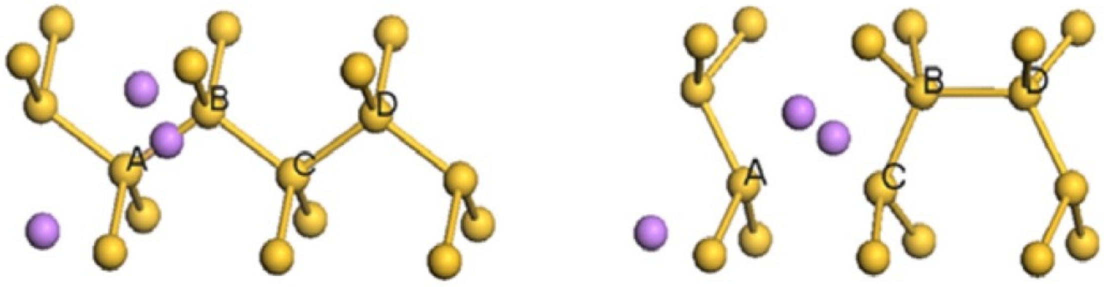

(a) (b)

Figure 4.3: Rearrangement of the Si lattice after lithium insertion at high doping concentration. (a) is the Si structure before relaxing; (b) is the Si configuration after geometrical relaxation. The purple balls represent Li atoms and the yellow ones are Si atoms. Image taken from [144].

For the sake of simplicity, a set of letters is used to label the Si and Li atoms. It is possible to see clearly that the Si(A)-Si(B) and Si(C)-Si(D) bonds are broken and a new Si(B)-Si(D) bond forms. Meanwhile, the distance between Si(A) and Si(C) is 3.308 A, which is too long to represent a bond. Therefore, the three-Si-neighboured Si(A) or Si(C) atoms have a dangling bond and create a negatively charged environment around them. Summarizing, Li dopants have broken a Si-Si bond permanently in two dangling bonds, which create a negatively charged zone that attracts two nearby Li ions.

4.1.2 State of the art

The theoretically high specific capacity of Silicon as anode material is counterbalanced by a significant volume changes (>300%) during the lithiation/delithiation processes, which produces cracks and pulverization of the electrode. Limit particle cracking upon lithiation is currently the main strategy to bring Silicon from being a promising alloying anode material [136, 137, 138, 139] to replace graphite-based anodes. A good strategy is the use of non-agglomerated nanosized silicon, as proven by several experimental works [109, 147, 148]. Controlling the Silicon particle morphology (i.e., nanospheres, [145, 149, 150] nanowires [151] or nanotubes [152]) is known to affect the electrochemical properties. Nanowires have been reported to be particularly superior promising in lithium ion storage (Figure 4.4) [153].
Due to the facile strain relaxation and efficient electron transport along each nanowire, this configuration is capable to avoid the issue of pulverization and contact loss. A carbon skin could enhance the cycling and rate performances [154], as well as Ti@Si core–shell coaxial nanorods.
The benefit of a metallic core is the dramatic reduction of the axial resistance observed in solid Si nanorods.
A completely different strategy is the realization of a composite, in which a carbon nanostructure encloses the silicon nanoparticles [82, 155, 156]. This strategy represents a well-known way to mitigate the volumetric changes while ensuring also the electrical contact of the electrode, improving the performance of the electrode in terms of both cycle life and rate. The Silicon nanoparticle inclusion in a carbon nanostructure is the key factor to make this approach effective. Composites obtained by just carbon coating methods or simply mixing Silicon nanoparticles and amorphous carbon lead only to minor improvements [138, 157]. Therefore, more complex strategies are needed. For the example, allowing Silicon nanoparticles to freely expand and contract has a positive effect on cyclability [139]. This result can be achieved with the encapsulation of Silicon particles into carbon nanostructures with empty spaces [158] or just with their infiltration inside a nanoporous matrix. Focusing attention on conductive carbon structures [82, 155, 156], graphene [98, 104, 159] has been shown to be a promising partner for Silicon, due to its excellent mechanical properties [105] and electrical conductivity [94]. In the last years several approaches have demonstrated the successful integratione of graphene with silicon nanoparticles, obtaining anodes with long cycle life [95, 96, 100, 107, 160, 161, 162]. In particular, the most common graphene-based material used is reduced graphene oxide (RGO) [163, 164, 165, 166, 167], due to the presence of an oxygen-containing functional group. Being RGO flakes hydrophilic, it enables the possibility of using

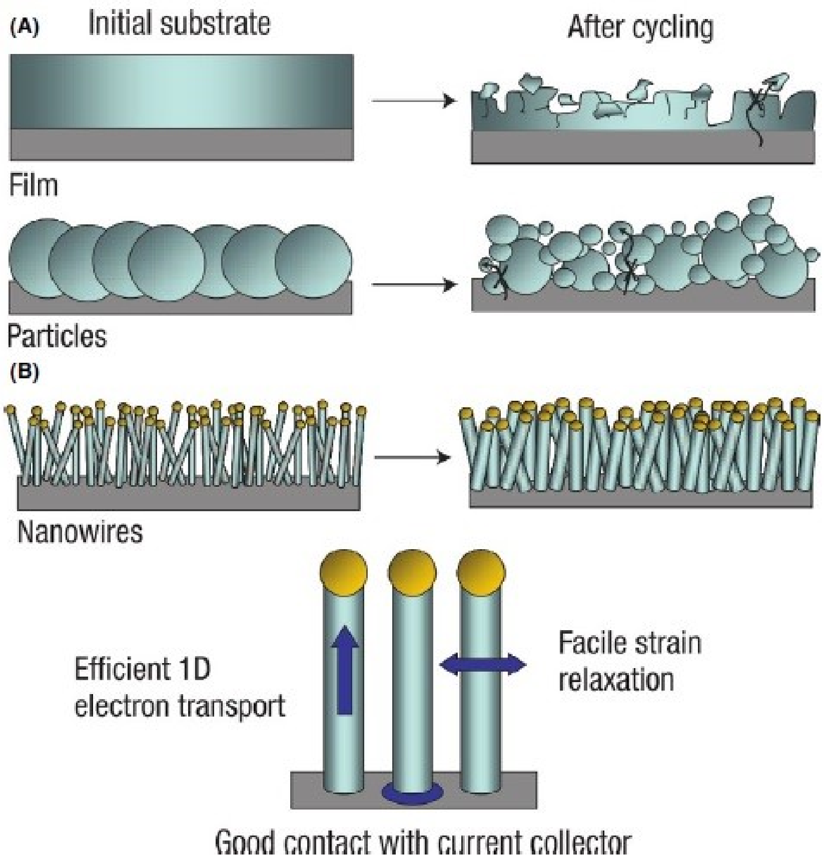

Figure 4.4: Schematic comparing the stability of (B) silicon nanowires with (A) thin film and particles upon repeated lithiation and delithiation. Image taken from [153].

a large variety of solvents, even water [104, 168].
Other strategies relies on modified graphene material such as N-doped graphene [169]. In these materials, the nitrogen atoms modify the graphene electronic structure [90, 91, 92, 93, 170], improving both the lithium diffusion kinetics as the transfer [171] and affecting positively its electrochemical performance [172, 173, 174].
Finally, single- or few-layer pristine graphene crystals (SLG and FLG, respectively) can be used. In these composite materials, the graphene provides an accommodation to the electroactive material and a much more effective pathway for electron conductivity [175, 176].

4.2 Development of a silicon-based Li-ion battery

The aim of our work was to realize a Si-graphene-based anode material to be implemented in a Li-ion battery. We designed a composite consisting of Silicon nanoparticles entrapped between horizontally oriented FLG flakes. Here, only the Silicon nanoparticles represent the active material, while the FLG flakes are used to increase the mechanical strength and the conductivity of the bulk Si.

Through chemical-physical characterization, phase and the structure of both the Silicon nanoparticles and the FLG flakes were studied, in particular after the annealing process, and was verified the realization of a thin layer (4nm circa) of carbon coating around the Silicon nanoparticles. The carbon coating has turned out to be decisive in further mechanical strengthening the Silicon nanoparticles, increasing at the same time the electronic conductivity.

Great efforts were also given in the realisation process. The goal was to identify a low-time consuming process, cheap and easy to be reproduced. The entire process for the realization of the composite requires less than 8 hours, resulting ready to be scalable up to the industry level. The process can be schematised in three steps: i) ultra-sonication of the composite; ii) drop casting on Cu disk; iii) thermal treatment.

Finally, the applicability of the Si-FLG based in a Li-ion cell anode was tested using a high capacity commercial cathode (NMC111), and the results have showed to be promising.

4.2.1 Materials and methods

Silicon nanoparticles (<100 nm diameter) and poly(acrylic acid) were purchased from Alfa-Aesar and used as received. The cathode, LiNi1/3Mn1/3Co1/3O2 (NMC111), was coated on Al foil (16 mg/cm2) kindly provided by Varta Micro Innovation gmbH.

The FLG flakes were prepared following the procedure already developed in the IIT graphene labs [177]. This procedure provides a Wet-Jet Mill exfoliation, through a mechanical stirrer, of 200g of graphite flakes (+100 mesh, Sigma-Aldrich) mixed with 20 L of N-methyl-2-pyrrolidone (NMP) (>97%, Sigma-Aldrich). A scheme of the wet-jet miller system is presented in Figure 4.5a.

The as-prepared mixture is pushed in the processor by a piston, where it is subject to a pulverization and an exfoliation process, with a pressure between 180 and 250 MPa. The processor, as shown in Figure 4.5b, is composed by a set of 5 different processors (disks A, B and $\bar{A}$), characterized by different holes size. The 4 disks A and $\bar{A}$ present each two holes in order to divide and recombine the as-prepared mixture in two different jet streams. The disk B consists of a half-cylinder channel (a nozzle) with a diameter of 0.3mm. The pulverization process takes place between the first two disk A and the disk B, mainly colliding the two pressurised streams of the particle liquid dispersion. The exfoliation process, on the other hand, takes places principally during the sample passage through the nozzle. The two streams, at the end, recombine in the last disk before leaving the processor. Finally, the sample needs to be cooled down in the chiller. This process is repeated other two times changing the disk B with other one presenting a nozzle of 0.15 mm and 0.10 mm respectively. A final rotavapor and freeze-drying processes are necessary to completely remove the NMP solvent.

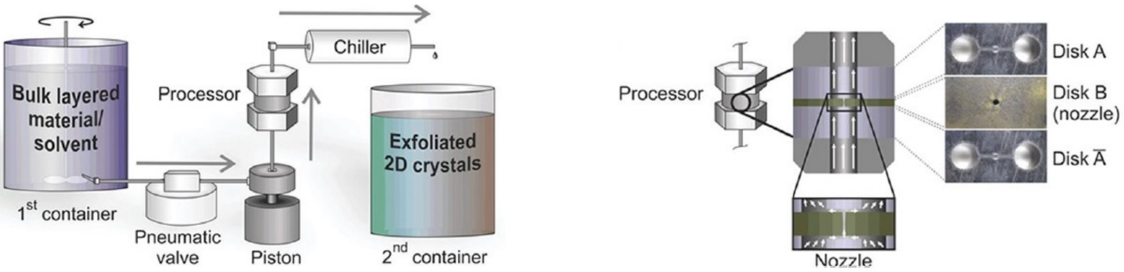

(a)

(b)

Figure 4.5: (a) Scheme of the wet-jet mill system, the arrows indicate the flow of the solvent through WJM, and (b) close-up view of the processor. The zoomed-in image in (b) shows the channel configuration and the disk arrangement. The solvent flow is indicated by the white arrows. On the right side is a top view of the holes and channels on each disk. The disks A and Ā have two holes of 1 mm in diameter, separated by 2.3 mm from centre to centre and joined by a half-cylinder channel of 0.3 mm in diameter. The thickness of the A and Ā disks is 4mm. Disk B is the core of the system; the image ((b), disk B) shows the 0.10 mm nozzle. It can be changed to 0.10, 0.20, and 0.30 mm nozzle diameter disks according to the size of the bulk layered crystals. The thickness of the B disk is 0.95 mm. Image taken from [177].

4.2.2 Electrode preparation

The anode material is composed of Silicon nanoparticles, FLG flakes and poly (acrylic acid) (PAA).The electrode preparation requires first the dispersion of equal amount of Silicon nanoparticles, FLG flakes and PAA in ethanol (see Figure 4.6). The concentration of solute in the solvent is equal to 30 mg (10 mg each component) / mL. The homogeneity of the mixture is guaranteed by ultrasonication for 90 min. The deposition of the obtained dispersion onto a copper disk, having a 15 mm in diameter, is performed by drop casting and it is followed by air-drying for 5 min. Finally, the last step consists of an annealing in a tubular furnace in reducing atmosphere. Under controlled atmosphere (vacuum + 5 sccm of $H2$), the sample first is heated up to 700 °C with a heating rate of 15 °C/min, then reaches the final

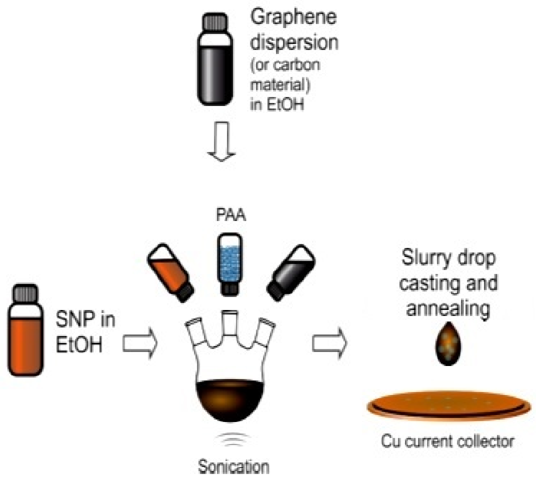

Figure 4.6: Sample preparation of the Si-FLG composite. Take from [178].

temperature of 750 °C with a heating rate of 5 °C/min. The temperature is kept constant for 30 min, then the sample is cooled down to room temperature. The aim of the annealing process is twofold: (i) increase the anode specific capacitance by the total annihilation of the binder, and (ii) realise a carbon coating over the Silicon nanoparticles and in between in order to achieve a higher conductivity of the composite through the formation of a better electrical contact between the Si-NPs and the FLG flakes. The samples are immediately stored in Argon inside a glove box in order to avoid undesired oxidation of the surface.

4.3 Chemical-physical characterization

Structural and morphological analyses have been carried out to demonstrate the validity of the approach, which combine ultrasonication and annealing, in order to obtain a silicon-FLG electrode with a well-organized structure.

4.3.1 X-ray diffraction analysis

Figure 4.7 shows the X-ray diffraction (XRD) patterns comparison of Silicon nanoparticles (green), Si-FLG composite pre-annealing (red) and after annealing (blue). The patterns were recorded on a PANalytical Empyrean X-ray diffractometer equipped with a 1.8 kW CuKa ceramic X-ray tube, PIXcel3D 2 x 2 area detector and operating at 45 kV and 40 mA. The diffraction patterns were collected in air at room temperature using Parallel-Beam (PB) geometry and symmetric reflection mode. X-ray diffraction data analysis was carried out using HighScore 4.7 software91 from PANalytical. For sake of clarity, the graphs also present the references of Si peaks (PDF 27-1402, green) and Graphite one (PDF 41-1482, orange).

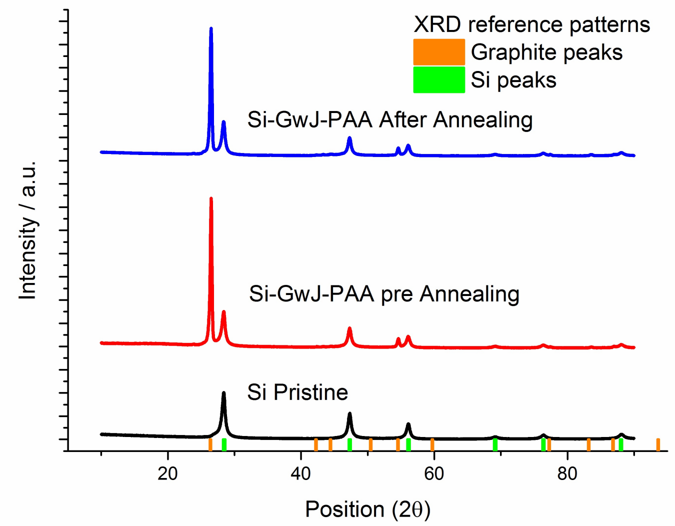

Figure 4.7: XRD patterns of Si pristine (green), Si-FLG nanocomposite before (red) and after annealing process.

The Si particles used in the composite presents the typical pattern of the cubic silicon. We can observe the main peak at 28.442°, corresponding to the (1,1,1) reflection. The composite pre-annealing shows in addition to the silicon signals, other two small peaks that can be indexed with graphite phase are visible, with the main signal at 26.381°, corresponding to the (0,0,2) reflection. The xrd pattern of the sample after the annealing procedure appears similar to the sample before annealing, giving us the information that the thermal treatment has no effect on the phase. However, after annealing all the peaks appear reduced in intensity.

4.3.2 X-ray photoelectron spectroscopy

X-ray photoelectron spectroscopy (XPS) was carried out to observe structural difference on the Silicon nanoparticles on the electrode surface, which are the ones which can be mainly subjected to an oxidation. The measurements were performed on a Kratos Axis UltraDLD spectrometer, using a monochromatic Al Ka source operated at 15 kV and 20 mA. High resolution narrow scans were acquired on Si 2p core levels at constant pass energy of 10 eV in steps of 0.1 eV. The photoelectrons were detected at a take-off angle of $\Phi = 0°$ with respect to the surface normal. The data were processed with Casa XPS software v 2.3.17. Silicon spectra fitting has been performed by considering Voigt profiles; for elemental silicon, an intensity ratio of 2:1 between the two components of the doublet and a doublet separation of

0.6 eV have been assumed [179]. Figure 4.8 shows the superposition of three XPS spectra relative to the pristine Silicon nanoparticles (green), the Si-FLG composite pre-annealing (blue) and after annealing (red).

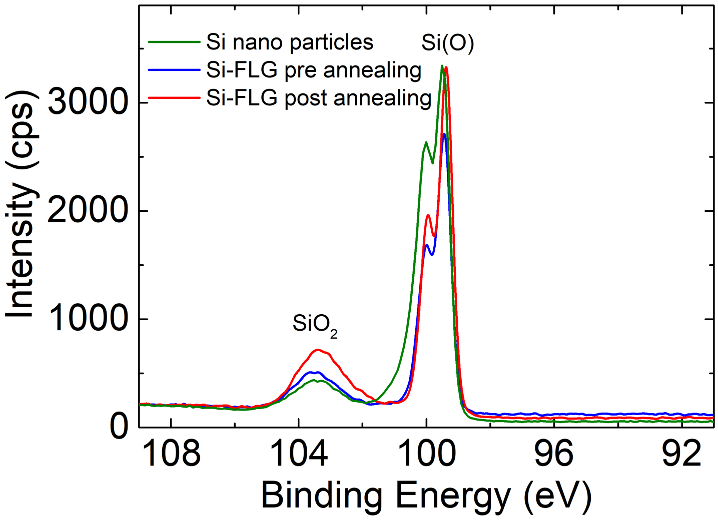

Figure 4.8: XPS spectrum comparison of the silicon particles (green) and of the silicon-FLG electrode pre-(blue) and post-(red) annealing.

All the spectra are characterized by the presence of a doublet of narrow peaks. The most intense is centred at (99.4 ± 0.2) eV, and it is typical of elemental silicon [179]. The broad peak centred at (103.4 ± 0.2) eV corresponds to SiO2 [179]. Focusing on the broad peak, it is not possible to observe significant difference between the pristine silicon and the silicon-FLG electrode not subjected to the annealing process. On the other hand, after the annealing process the results depicts an increase in intensity of the oxide peak, which pass from 19.6% to 28.3% of the whole Si content. This might be due to annealing conditions and by the presence of oxygen atoms in the PAA.

4.3.3 Raman spectroscopy

To validate the formation of a carbon layer over the Silicon nanoparticles, Raman spectra in the $1100 - 1900$ cm^{-1} range were acquired by using a Renishaw inVia micro-Raman spectrometer with the 514.5 nm line of an Ar+ laser. The incident laser was focused by a 50× optical microscope objective with a numerical aperture of 0.95 and then the scattered light was detected in a backscattering geometry dispersed by a 2400 l/mm holografic grating. All the spectra were collected by acquiring 3 accumulations of 30 s each. Acquired spectra were analyzed by OriginLab OriginPro 2016 using Voight curves in order to deconvolute the main Lorentzian components. In Figure 4.9 the superposition of Raman spectra of pristine and annealed samples is reported.

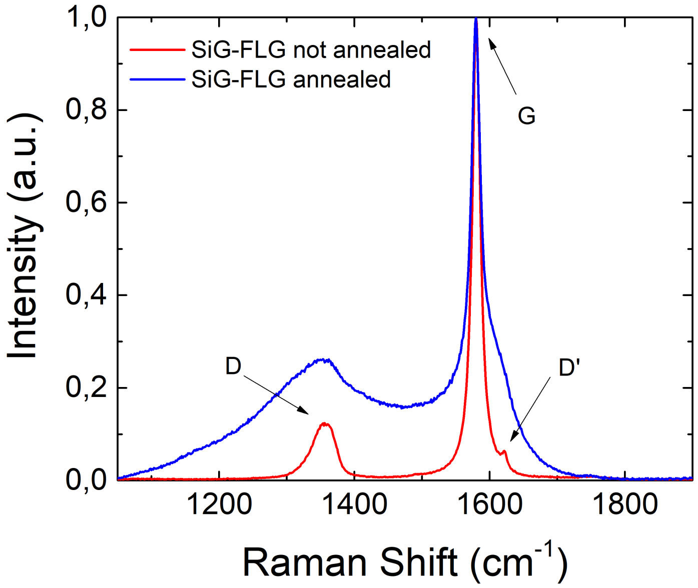

Figure 4.9: Superposition of the normalized Raman spectra for the Si-FLG anode pre-annealing (red) and post-annealing (blue).

Spectra were normalized to the intensity of the carbon G peak and the peaks were deconvoluted in their Lorentzian components.

The pre-annealing sample spectrum (red curve) presents the typical components of graphene spectrum in the range acquired (D, G, and D' [180]). The peaks are well-defined and separated and the I(G)/I(D) ratio is 0.064. The Raman spectrum of the post-annealing sample (blue curve) shows several differences. First, the intensity of the D peak was strongly increased. Moreover, a partially overlapping of the D and G peaks can be easily observed. Furthermore, the deconvolution of the Raman spectrum identifies five different components: three of them, i.e., D, G, and D' peaks, can be ascribed to the graphene flakes, while the other two reveal the typical features of the amorphous carbon.

The origin of the amorphous carbon can be ascribed to the carbon content present in the binder, which turned into a carbon coating after the annealing process.

4.4 Morphological analysis

An High Resolution Transmission Electron Microscopy imaging with relative fast Fourier transformation were carried out and the results are shown in Figure 4.10. The upper images were taken on the composite before the annealing process, while the lower one represents the material after the annealing process.

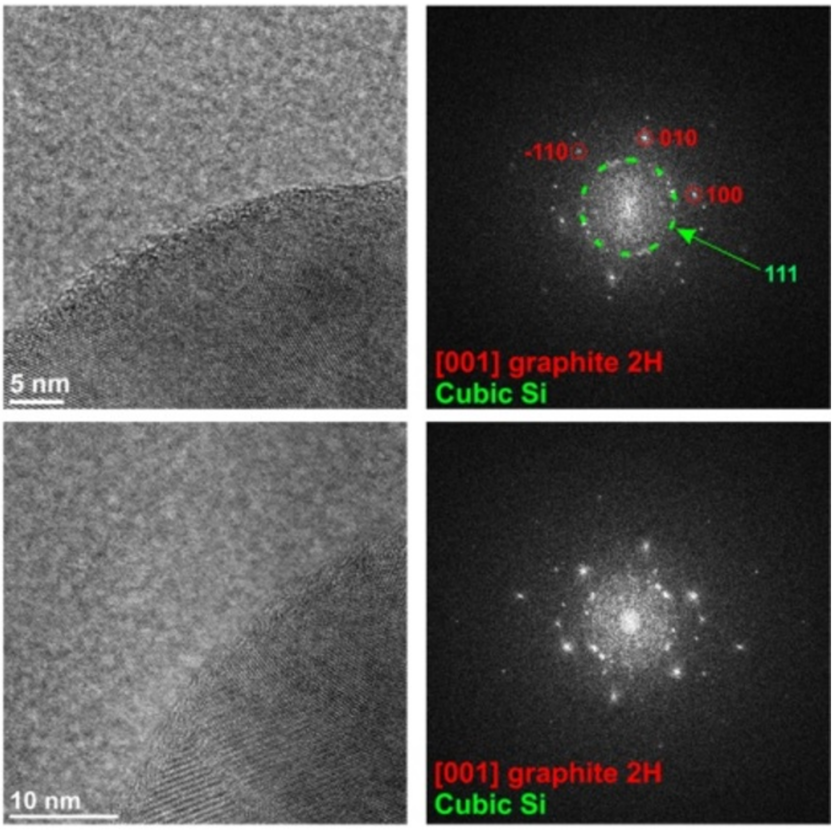

Figure 4.10: HRTEM images and corresponding fast Fourier transforms (FFTs) for regions in the (upper) pristine and (lower) annealed Si-FLG electrode on top of an amorphous carbon film. The FFTs indicate a [001]-oriented graphite (ICSD 76767) pattern, due to the FLG flakes, and randomly oriented cubic silicon (ICSD 51688) nanometre-sized domains.

The fast Fourier transform (FFT) of the HRTEM images of Figure 4.10 indicates the [001] orientation of the FLG flakes and a polycrystalline structure of Silicon nanoparticles due to the relative spots arranged in rings. This is true both before (upper) and after (lower) the annealing process, confirming again how this process does not affect the structure of the materials.
The Raman spectra suggests that the annealing process leads to the formation of graphite on the material. This is a desired result, since it can be linked to the

formation of a carbon coating around the Silicon nanoparticles. To acquire more evidence of the presence of the of carbon coating, an energy-filtered transmission electron microscopy (EFTEM) elemental maps was carried out.

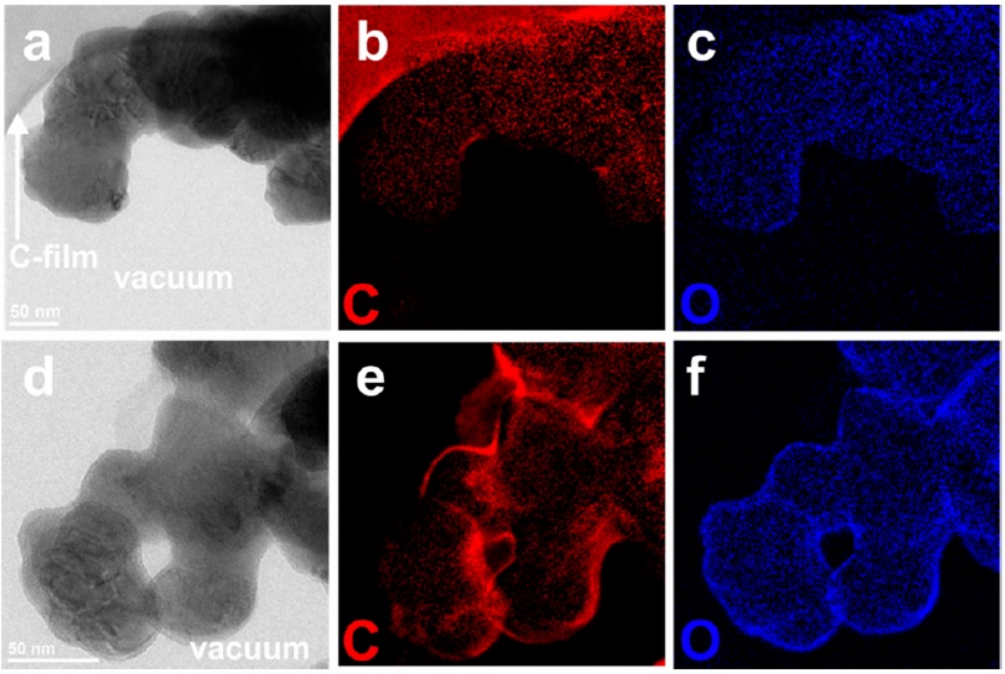

Figure 4.11: (a,d) Zero-loss filtered Bright Field TEM (BF-TEM) image and (b,c, e,f) corresponding EFTEM elemental maps for carbon (red) and oxygen (blue) on regions of (a-c) pristine and (d-f) annealed Si-FLG electrode, partly suspended on a hole in the holey carbon support film.

Figure 4.11 shows the EFTEM analysis for the composite material pre-annealing (Figure 4.11a-c) and post-annealing (Figure 4.11d-f). The C map in Figure 4.11e shows an inhomogeneous 3-nm-thick carbon coverage all over the silicon nanoparticles, which is not present in the case of the not-annealed sample. Furthermore, in the pristine sample there is a low amount of carbon.

The O map, on the other hand, clearly indicates a surface oxidation due to the annealing process (Figure 4.11f), which is less prominent in the pristine sample (Figure 4.11c).

So far, the results have clearly shown that the annealing process does not affect the structure of Silicon nanoparticles and Graphene flakes but leads to the total burning of the binder together with the formation of a carbon coating around the Silicon nanoparticles. It was also demonstrated a slightly oxidation of the silicon nanoparticles, both on the surface and in the bulk. These data refer all to the structure of the composite. Therefore, SEM imaging was carried out to verify if and how the annealing process has modified the morphology of the material.

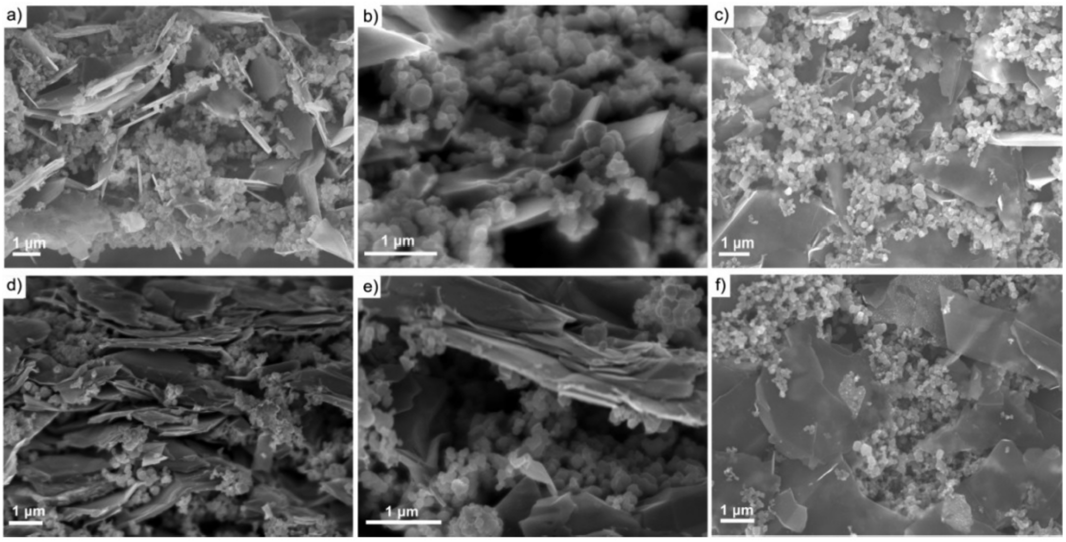

Figure 4.12: (a-c) Cross section and top view SEM micrographs of the silicon-FLG electrode before and (d-f) after annealing.

Figures 4.12a and 4.12b show the cross section of the electrode before the annealing process. The two components are easy to be distinguished, but the entire composite seems muddled and presents also large aggregates of Silicon nanoparticles, as shown in Figure 4.12c.
After the annealing, the morphology of the composite changes significantly. In the cross section of Figure 4.12d, the graphene flakes are well oriented and parallel one to each other. Even the dimension of the Silicon aggregates appears reduced and better distributed between the FLG flakes. More in detail, Figure 4.12e shows that FLG flakes create a well-organized and ordered structure entrapping silicon nanoparticles. Even the surface of the electrode (top view, Figure 4.12f) presents differences, with the FLG flakes covering a higher surface compared to the situation before the annealing.

4.4.1 Conclusion

Summarizing the chemical-physical analysis, we demonstrated that the annealing process affects positively the structure of the composite material, without modifying the phases of the singular components. The FLG flakes, initially disordered, are horizontally oriented once subjected to the annealing procedure, realising in this way an optimal accommodation for the Silicon nanoparticles. In such a structure, the Silicon nanoparticles occupy the space between FLG flakes, which also guarantee a conductive matrix able to transfer the capacity till the Cu disk. Moreover, the binder annihilation provides the carbon atoms necessary to the Silicon nanoparticle carbon coating, as demonstrate both by Raman measurements and HR-TEM imaging.

Chapter 5

Development of a Li-ion cell

5.1 Evaluation of the electrochemical properties of Silicon-graphene composite in Lithium cell

5.1.1 Evaluation of Si-content in the anode material

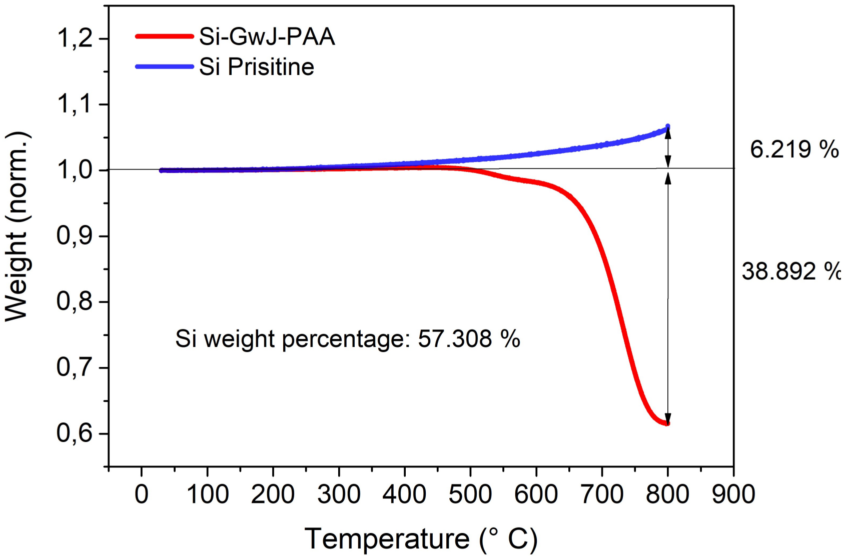

Figure 5.1: Thermogravimetric analysis of the pristine silicon nanoparticles (blue) and Si-FLG electrode (red). Image taken from [181]

To evaluate the exact content of silicon in the composite, a thermogravimetric analysis (TGA) [182] was performed using a TGA Q500-TA Instrument. The measurement was carried out in air with a flux of 50 ml/min, in order to eliminate all the carbonaceous matrix. The temperature scan comprises an initial stabilization of the sample at 30 °C for 5 minutes, a heating rump at 5 °C/min up to a final temperature of 800 °C and an isothermal step at 800°C for 1 hour. The contribution of oxidation of silicon nano-particles, was evaluated with a second experiment conducted on pristine Silicon nanoparticles. The results are shown in Figure 5.1. The figure shows the weight loss (red curve), normalized to the starting value, as a function of the temperature. It is shown that the first variation in the mass is observable at a temperature of about 500 °C, but it is only after a temperature greater than 700 °C that most of mass loss takes place. Contrary, the Si-NPs mass (blue curve) shows a continuous increasing, due to the oxidation of the silicon. Combining the relative increase of the Si-NPs mass with the expected drop in the Si-FLG sample, it is possible to estimate a weight percentage of the Silicon nanoparticles on the anode mass equal to 57.3%. The active material mass, evaluated starting from this value, has been used in all the galvanostatic cycling to estimate the specific capacity and the current density applied to the cell.

5.1.2 Cell assembly

The evaluation of the electrochemical properties of our Silicon-graphene composite has been conducted in half-cells, in which the Si-FLG based electrode was tested against a Lithium foil. The electrode was realised through the procedure presented in the previous chapter, in which the same mass amount of Silicon nanoparticles, Few-layer Graphene and Poly-acrylic acid as binder were mixed together in Ethanol and sonicated for 90 minutes. The mixture was then deposited by drop casting on a Cu-disk. The carbon coating of the Silicon nanoparticles was obtained through the annealing of the binder up to 750 °C in reduced atmosphere.

As comparison to Si-graphene composite, other two types of electrode were prepared. The first one named Silicon-pristine was obtained through mixing and sonication of only Silicon nanoparticles and PAA in Ethanol having a mass ratio of 9:1. The deposition was obtained through drop casting. The second electrode was realized mixing a same amount of Silicon nanoparticles and PAA in Ethanol, subjected to a sonication process and, after a deposition through drop casting, to an annealing process up to 750 °C, similarly to the Si-FLG electrodes.

The electrochemical measurements were conducted in CR2032 coin cells, facing the Si-FLG electrode to a chip of metallic lithium as counter electrode and using a glass fibre as separator (Whatman GF/D). The electrolyte used was a commercial 1M $LiPF_6$ in a 50:50 w/w mixture of EC and DMC with the addition of 10% v/v of Fluoroethylene carbonate (FEC). All the measurements were carried out in the potential range of 0.1 – 1.0 V at C/10 (1C = 3500 mA/g), with a first formation cycle with a potential range of 0.01 - 2.0 V at C/20. The aim of the potential range is to allow the formation of a stable solid-electrolyte interface (SEI).

5.1.3 Galvanostatic Cycling

Controlled current methods represent the main experimental setup used in this thesis work to analyse the cycling performances of the cell. A schematic representation is shown in Figure 5.2

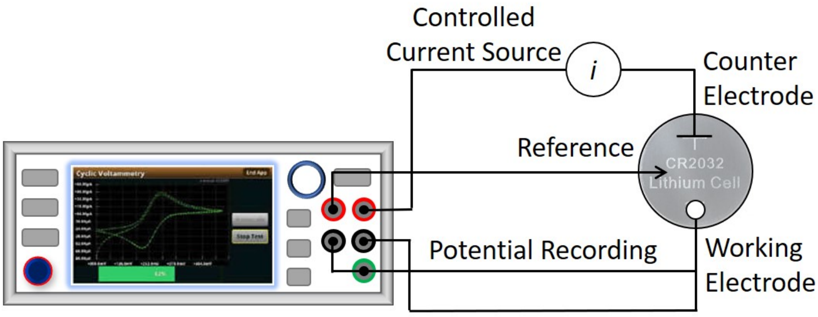

Figure 5.2: Schematic representation of the experimental setup. A potentiostat applies to a cell a controlled current and measures contemporary the voltage of the working electrode against a reference. Paring the data of the current applied with the voltage on the working electrode it is possible to evaluate the capacity of the electrode.

Figure 5.3 shows the comparison of the cycling performance of the silicon pristine (orange) silicon carbon coated (grey) and Si-FLG (blue) electrodes obtained by galvanostatic cycling in lithium cells, following the procedure described in the previous paragraph.
In the comparison represented in Figure 5.3, the cycling performances are expressed through the specific capacity (charge – full dots and discharge – empty dots capacities) as a function of the cycle number.
It should not be surprising that just the Silicon nanoparticles shows an appreciable cycling performance. As suggested by several experimental works [109, 147, 148], non-agglomerated nanosized silicon were chosen as active material, since it could be a good strategy to suppress the silicon particle cracking. In Figure 5.3, the full (charge capacity) and empty (discharge capacity) circles represent the specific capacity over cycling of commercial Silicon nanoparticles. It is possible to observe how the first discharge capacity is very close to the theoretically one, but also that the capacity drops quickly, and it is less than 1000 mAh/g after just 40 cycles. The Coulombic Efficiency near 99% demonstrates that the Silicon nanoparticles can perform long cycling, but it is still not enough to be used as anode in a commercial battery.
The semiconductor nature of Silicon represents a typical issue, since the material shows very low conductivity respect other anode materials, such as the commonly-used graphite. Therefore, minor improvements should come by simply mixing silicon nanoparticles with an amorphous carbon or by carbon coating methods [138,

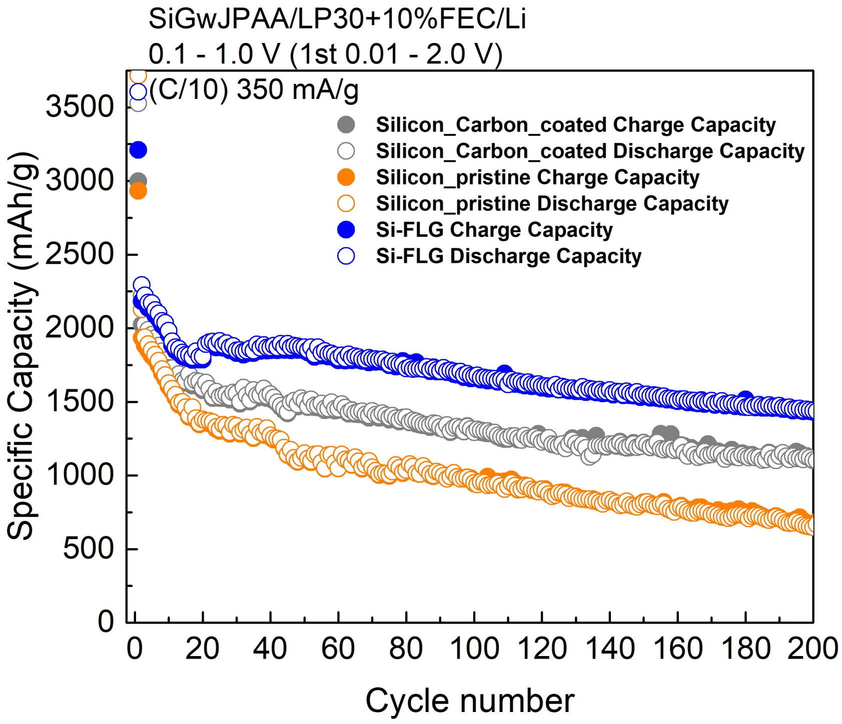

Figure 5.3: Cycling performances versus lithium comparison of Silicon particles: pristine (orange), with carbon coating (grey) and incapsulated inside few-layer graphene (blue). The tests are performed in half cell, with a current density of 350 mA/g (C/10), with a voltage range of 0.1 – 1.0 V after a first forming cycle; the electrolyte is LP30 + 10% of FEC

157], as represented in Figure 5.3 by the grey circles. The carbon coating of the Silicon nanoparticles is obtained just mixing in equal mass rate Silicon and binder (PAA) and annealing the composite. The behaviour of the specific capacity is similar with respect to pristine Silicon nanoparticles, but the Coulombic Efficiency is now higher than 99%, resulting in a higher mean capacity higher than 1000 mAh/g over 200 cycles. However, the carbon coating just increases the conductivity of the anode material without affecting considerably the volumetric changes which Silicon suffers.

The realization of a composite, in which a carbon nanostructure encloses the silicon nanoparticles, represents a well-known way to mitigate the volumetric changes while ensuring also the electrical contact of the electrode [82, 155, 156]. It should improve the performance of the electrode in terms of both cycle life and rate. This strategy is represented in Figure 5.3 by the blue circles, where Silicon nanoparticles with carbon coating are finally entrapped between horizontally oriented FLG flakes. This solution not only increase the mean capacity, which is higher than 1500 mAh/g also after 200 cycles, it results also in a more stability of the cycling, with a quite linear drops after the 40th cycle.

5.1.4 Electrolytes

The choice of the correct voltage range can strongly affect the cycling performance of the anode material in lithium halg-cell tests. In the same way, also the electrolyte affects both the cycling stability as well asthe specific capacity. The commonly used electrolyte is LP30, a 1M LiPF6 in a 50:50 w/w mixture of EC and DMC. Commonly, this lithium salt is coupled with additives like Vinyl Carbonate (VC) or Fluoroethylene carbonate (FEC). Figure 5.4 shows the result of several measurements in which the LP30 is coupled with combination of VC (Figure 5.4a) and/or FEC (Figure 5.4b). In both figures the cycling performance measured using only LP30 without additives as electrolyte is presented as reference.

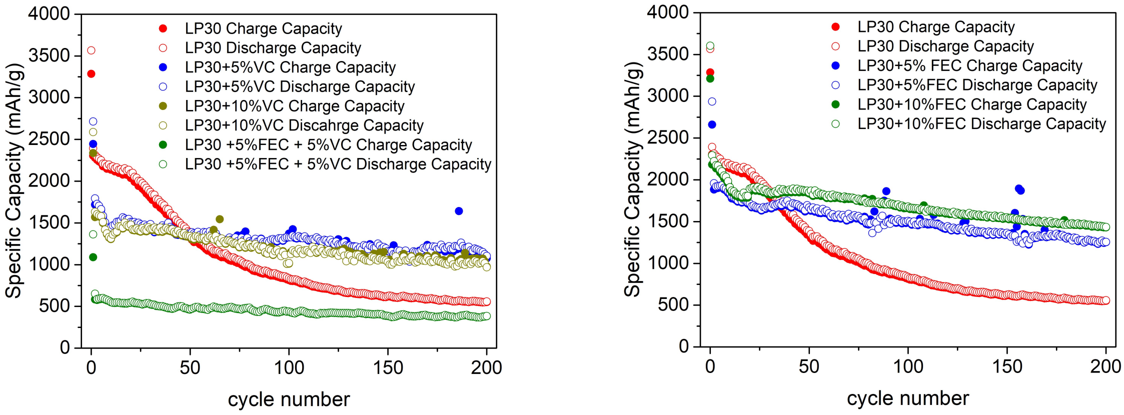

(a) (b)

Figure 5.4: Cycling performance of the anode in lithium cell using as electrolyte LP30 with several combination of VC (a) and FEC(b). The results using only LP30 as electrolyte are used as reference. Cycling condition: current density 350 mA/g; first forming cycle voltage range 0.01 -2.0 V, other cycles voltage range 0.1 – 1.0 V.

The cycling condition are the one selected in Figure 5.3 with a current density of 350 mA/g, a voltage range of 0.1 – 1.0 V and a first forming cycle voltage range of 0.01 – 2.0 V.

The electrolyte with only lithium salt (red dots) presents the best results for the first 20 cycles, after which there is an exponential drop in the specific capacity with 500 mAh/g as asymptote. The anode material seems stable, but the drastic drop after only 20 cycles advises against a possible use in commercial batteries. In order to maintain a stable value of the specific capacity, LP30 was coupled first with VC as addictive (Figure 5.4a). Weather the volumetric addition of VC is equal to 5% or 10%, the behaviour is quite the same, with a specific capacity that start from

around 1500 mAh/g and slowly finishes at 1250 mAh/g, with a little better performance with just 5% v/v of VC. However, the cycling stability it is not maintained. For this reason, VC in this case does not represent a valid option as additive to LP30. As final analysis, LP30 with both VC and FEC (LP30 + 5% v/v VC + 5% v/v FEC) was tested. The result is the worst presented, with a stable cycling around 500 mAh/g, lower even than the electrolyte with just the lithium salt.
Figure 5.4b shows that FEC gives an important contribution to the cycling. The specific capacity is higher than with VC, even considering that LP30 + 5% v/v FEC shows some instability after about 70 cycles. The best results were obtained with an electrolyte composed by LP30 + 10% v/v FEC. The specific capacity shows the highest values, coupled with a good long-term stability. Comparing the results with VC and FEC, it is possible to observe the same behaviour: the cycling seems to have two different trends, with a most pronounced slope during the first cycles and a sweeter one after about 20 cycles. Since this result was obtained in all measurements, it is not possible to consider the electrolyte the main cause, or even to asset a sensible contribution of the latter.

5.1.5 Current Density

An important feature of the anode material is related to the possibility of sustaining high currents. Therefore, further tests have been performed to evaluate the electrochemical performance of the Si-FLG electrode at higher currents.

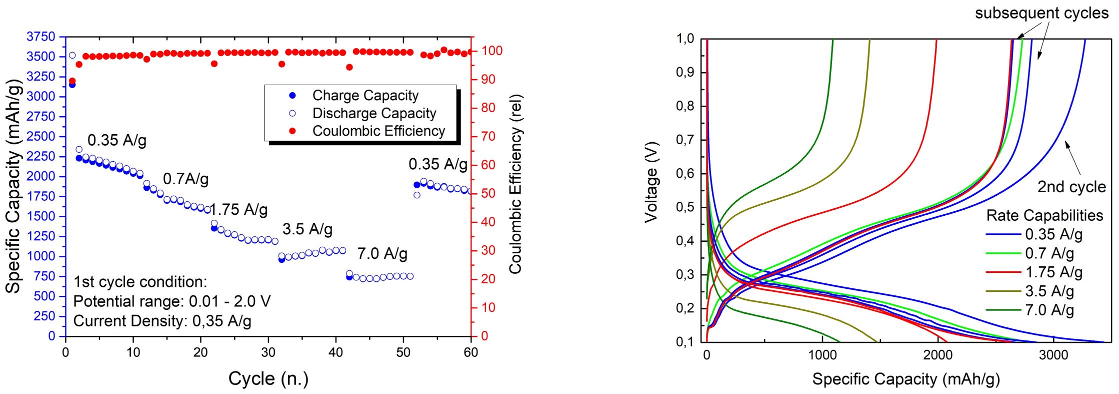

(a) (b)

Figure 5.5: Charge-discharge rate capability. Images taken from [181].

The charge-discharge rate capability presented in Figure 5.5 is one of the most important properties of anode materials for lithium batteries. It represents the ability of the material to reach and hold high current density. The test is quite simple. The initial current density, nominally a C-rate of C/10 rate also known as a ten-hours charge/discharge, is applied for the first cycles; then, it is increased step by

step up to the desired value (in this case 7.0 A/g equal to 2C rate or 30 minutes charge/discharge); at the end, the current density comes back to the initial value. The results display a stair-like aspect, with the specific capacity decreasing with an increase of the current density. This results from the fact that faster electrochemical reactions are always less interacting with the bulk material. With the last step, when the current density comes back to the initial value, the specific capacity should be at similar values of the first cycles. The main information coming from the measurements, is that the anode material is capable to work also with high current density up to 7.0 A/g.
Starting from the results of the rate capacity, the electrode was also tested with a galvanostatic cycling performed with a potential rate of 0.1 – 1.0 V and a current density from of 1C. The first forming cycle was carried out in a potential range of 0.01 – 2.0 V and at a current rate of C/10. The results are presented in Figure 5.6. As expected, the specific capacity exchanged upon cycling is lower than the one at low current density (Figure 5.3, blue), but after 100 cycles the electrode continue to achieve 1000 mAh/g and it decrease to 760 mAh/g after 250 cycles. The capacity retention is then equal to 49.0%. The Si-FLG electrode material demonstrates its ability to hold high current density also for prolonged cycling.

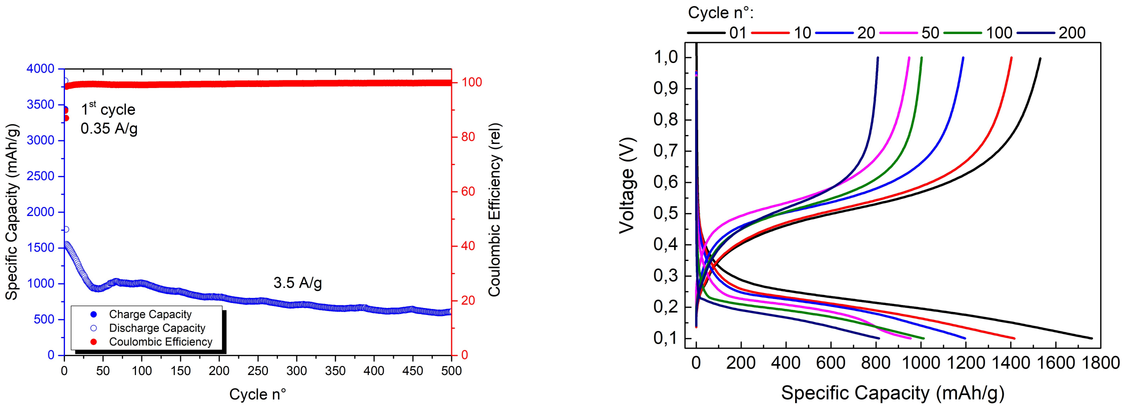

(a) (b)

Figure 5.6: (a) Cycling performance of the anode in lithium cell. Current density 3.5 Ah/g. Voltage Range 0.1 – 1.0 V. First forming cycle voltage range 0.01 – 2.0 V, current density 350 mAh/g. (b) potential profiles of a selected number of cycles. Images taken from [181].

5.1.6 Mass Loading Effect

Expressing the capacities of electrode materials in terms of specific capacity provides the amount of charge stored per mass unit and leads an immediate verification with the expected theoretical value. For example, Si-based anode material

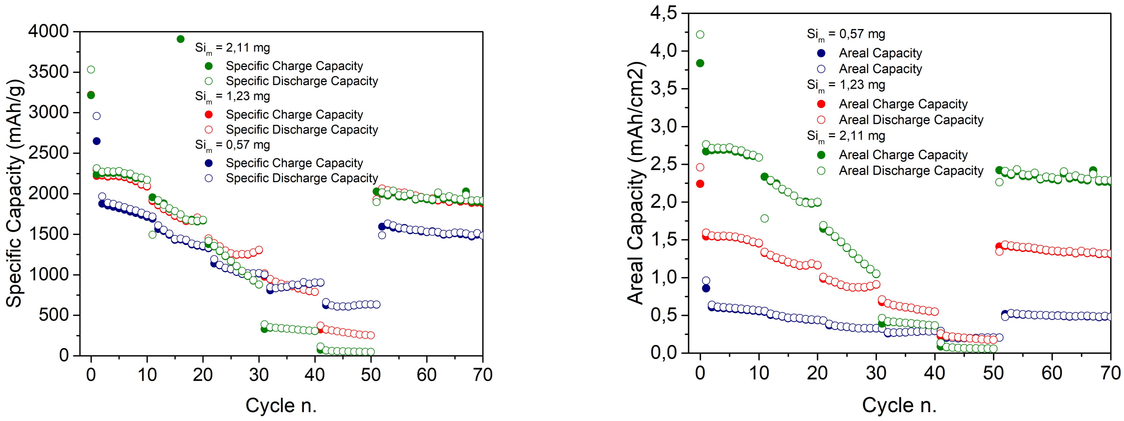

(a) (b)

Figure 5.7: Rate capability measured at different current density values. The Charge/Discharge capacity are referred to a) the mass of Silicon and b) the electrode surface (1.768 cm^2). Voltage range: first forming cycle 0.01 - 2.0 V, other cycles 0.1 - 1.0 V.

are usually referred to 3500 mAh/g (or even 4200 mAh/g) as theoretical specific capacity. The more comparable the values, the closer the material under analysis is to its optimum. Therefore, often different electrode materials are compared in terms of specific capacity. However, the electrochemical reactions are usually limited to electrode surface and to the higher portion of the bulk. It comes that the higher values of specific capacity can be observed only with thin layers which, on the contrary, have low value of total capacity. Moreover, the specific capacity shows a peak function respect the mass and, once passed the maximizing mass amount, it slowly decreases. Therefore, when it comes to design a cell for real application, the areal capacity becomes more reliable. With this parameter, the capacity is expressed in terms of the electrode surface, and the total capacity shows a linear dependence to the areal capacity, unlike specific capacity. Both analyses are shown in Figure 5.7.

Figure 5.7a shows the capacities referred to the mass obtained with three different mass loading for several current densities. The lower mass loading (0.57 mg of Silicon nanoparticles), as it could be expected, has the lower values of specific capacity but can sustain the highest current density (7.0 A/g). This result is not surprising: most probably, at this current density, the electrochemical reactions regards mainly, or only, the surface. The second mass loading selected (1.23 mg of Silicon nanoparticles), leads the highest specific capacity of the composite under study. As confirmation, the measurements obtained with a higher mass loading (2.21 mg of Silicon nanoparticles) show, at all the current density, a lower specific capacity. It means that the increment in the total capacity is lower than the one in the mass loading. In conclusion, the information obtained are the following: the anode material can hold high current density despite the mass loading; for very high current density (7.0 A/g), the electrochemical reactions involve just the surface of the material, and a mass loading of 0.57 mg could be enough; the highest performance can be obtained with a mass of active material between 1.2 mg and 2.2 mg.

The same capacities of Figure 5.7a are then expressed on the electrode surface in terms of areal capacity, as shown in Figure 5.7b. Here, the results are quite different. The increase of the mass loading results directly in an increasing of the areal capacity. Moreover, the lower mass loading seems not sufficient to cover adequately all the surface, resulting in a unit ratio between areal capacity and mass loading, while the other two measurements have the same index of about 1.22. The other noteworthy information is the areal capacity of the material with highest mass loading and equal to about 2.5 mAh/cm^2, higher than most of the commercial nowadays cathode material (e.g. NMC 111 has a surface capacity of about 2.0 mAh/cm^2). The results of Figure 5.7b become very useful when it comes to design a full battery, since the areal capacity of the two electrodes must be equal. This should be obtained using electrode materials with the same areal capacity. However, mainly inside a coin cell, if the difference is limited there is also the possibility to resize one of the two electrodes in order to obtain a similar total capacity.

5.1.7 Potentiostatic Intermittent Titration Techniques

The Potentiostatic Intermittent Titration Techniques [183] (PITT) is a method performed to have an insight on the redox processes of the electrode under analysis. A potentiostat apply to the electrode a potential equal to its initial equilibrium potential. Then the potential value is increased with a small step for a given time, and the chronoamperometric response is recorded. At this point, the system switch to open circuit in order to record the equilibrium potential. The latter will be as close to the previously applied potential as the final current was negligible at the cut-off. The charge increment is given as:

$$\Delta Q = \int_t i(dt) \tag{5.1}$$

where i is the chronoamperometric response. The shape strictly depends on the kinetics of the process at that potential levels. A set of "incremental capacity" values, ΔQ (V), can be obtained just repeating the experiment.

A.H. Thompson [184] proposed an extension of the PITT protocol in which the successive steps of potential are applied without going through an open circuit period. In this method, the system switch to the following step every time the reduction (oxidation) current has reached a predefined value which is considered as negligible compared to the capacity of the system. The result is a set of quasi-equilibrium incremental capacities values, with a periodic potential interval corresponding to the potential step amplitude.

The main difference with respect to a linear sweep cycling voltammetry lies on the duration of a potential level: while in the PITT it depends on the kinetics of the process at that level, in a linear sweep it is either continuous or stepwise.

A PITT measurement was performed in a Biologic VMP3 potentiostat to have an insight on the redox processes of the Si-FLG composite vs Li/Li+ in half cell, and Figure 5.8 reports the results. In the first cycle a voltage was applied in a range of 0.01 – 2.0 V, while for the other cycles the potential range was limited between 0.1 -1.0 V. The current density was equal to 350 mA/g, approximately a C/10 rate.

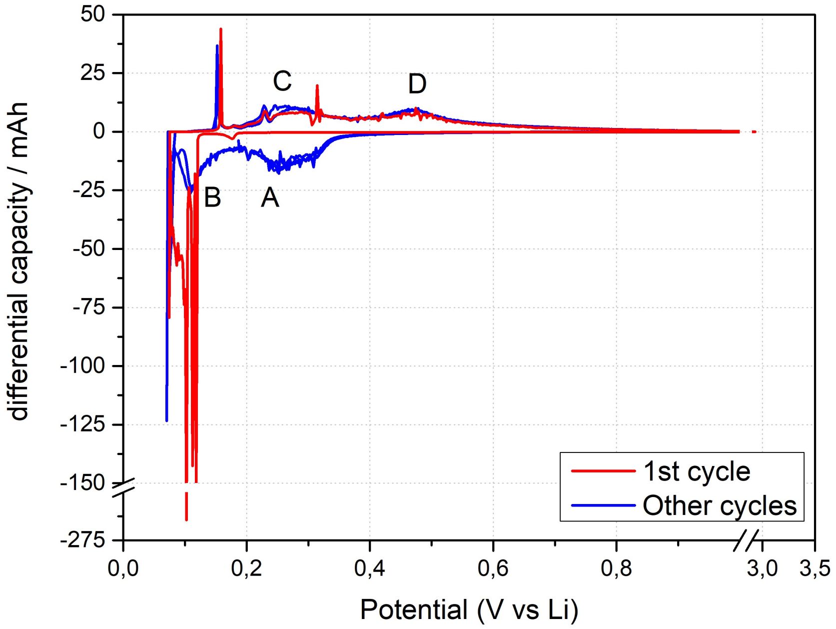

Figure 5.8: PITT response of the annealed silicon-graphene electrode in lithium cell. Image taken from [181].

During the lithiation, it is possible to highlight two main processes related to silicon (peaks A and B). The peaks A, between 0.25-0.3 V, seem to be a broad doublet peak and suggest a gradual lithiation of the crystalline silicon phase to amorphous Li2.0Si alloys. This phase involves extended Si networks and large Si-Si clusters [185]. The multiple processes occurring at peaks B, below 0.13V, may represent the complete lithiation of Si, which involves the formation of amorphous-Li3.5Si, in parallel with the intercalation of lithium into FLG layers. This process leads to the further breaking of Si-Si bonds with the subsequent formation of small Si clusters or eventually isolated Si atoms. In addition, only in the first discharge (blue line) it is possible to identify a process starting around 0.2V, followed by multiple processes below 0.13V, which could be brought back to the formation of c-Li3.75Si

from a-LixSi [186, 187, 188].
In the recharge process, the two large peaks at 0.3 and 0.45V (peaks C and D, respectively) correspond to silicon electrochemical process [189, 190, 191, 192]. In these processes the Silicon nanoparticles convert gradually from Li3.5Si to the initial phase, passing through $a - \mathrm{Li} \sim 2.0\mathrm{Si}$. The redox process of FLG are observable at 0.1 and 0.15V. Therefore, limiting the potential cut-offs to 0.1-1V results also in a limited contribution of FLG into redox process. At the end, two-anodic process centred at 0.25 and 0.1V are observable.
With reference to the graphene content, it has been reported that its eventual contribution to the lithiation process appears at around 0.07 V, consisting mainly in the Li+ insertion into graphene [193]. Working with a potential range of 0.1 - 1.0 V, it should be possible to exclude the contribution of graphene in the lithiation process, as also Figure 5.8 seems to suggest. This could a proof that, in this composite, the only active material is constituted by the Silicon nanoparticles.

5.1.8 Post Mortem Analysis

The blue circles (full and empty) shown in Figure 5.3, represent the cycling performance of the Si-FLG composite material up to about 200 cycles. In order to fully analyse the behaviour of the composite, the first 100 cycles of the cycling are presented in Figure 5.9.
The composite in analysis presents two different behaviour: a first pronounced slope until about cycle #10, and a second more stable cycling after 20 cycles and up to long cycling (represented by cycle #100). The cycling performance, and also the PITT measurement, are not enough to fully understand the reason for a similar behaviour. Therefore, a post-mortem analysis was carried out using both SEM and TEM imaging techniques. 4 points, highlighted in Figure 5.9 with circles, was selected to carry on the analysis:

- After the first forming cycle
- At the end of the first slope (cycle #10)
- In the mean of the second slope (cycle #50)
- After long cycling (cycle #100)

A first cycle with a deep voltage range (0.01 - 2.0V) is performed with a current density of 350 mAh/g (theoretically C/10).
The comparison of the images indicates that no clear change is appreciated after 1 cycle. The Si spots in the FFT image (Figure 5.10e) are arranged in rings, confirming the BF-TEM information (i.e., nonhomogeneous contrast due to varying diffraction condition) of the Si net-like structures being polycrystalline. The conclusion is that the first forming cycle is able to stabilise the SEI layer without

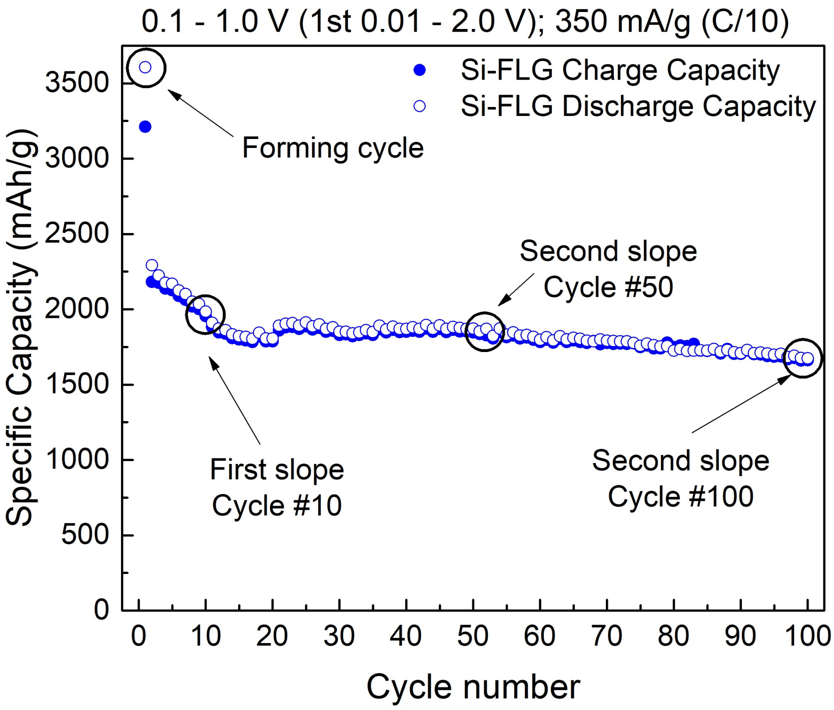

Figure 5.9: First 100 points of the cycling performance of the anode in lithium cell from Figure 2. Current density 350 mAh/g. First cycle voltage range 0.01 - 2.0 V. Other cycles voltage range 0.1-– 1.0 V.

affecting the structure of the Si nanoparticles.

The post-mortem analysis of the anode after 10 cycles shows the complete amorphization of the Silicon nanoparticles, as shown by FFT image of Figure 5.10f. It is possible to state that the first pronounced slope represents the amorphization of the Silicon nanoparticles, after which the cycling assumes a more horizontal decrease. Once that the Silicon nanoparticles become amorphic, they do no more change their structure, as demonstrate by the FFT images after 50 cycles (Figure 5.10g). On the other hand, Figure 5.10h shows the expected [001] orientation of the FLG flakes, confirming that also after the first forming cycle and over 100 cycles the FLG flakes are still crystalline. The conclusion is that the FLG flakes do not take part as an active material in the electrochemical process but affects the conductivity and the stability of the anode.

SEM-TEM imaging showed the volume-expansion issue, while electrochemical tests have returned that the material has maintained high capacity values (2.5 Ah/g circa) near the theoretical ones and quite ten times the carbon-based materials capacity. The mean capacity is higher than 1.5 Ah/g also after 200 cycles and is accompanied by a high stability of the cycling, with a quite linear drops after the

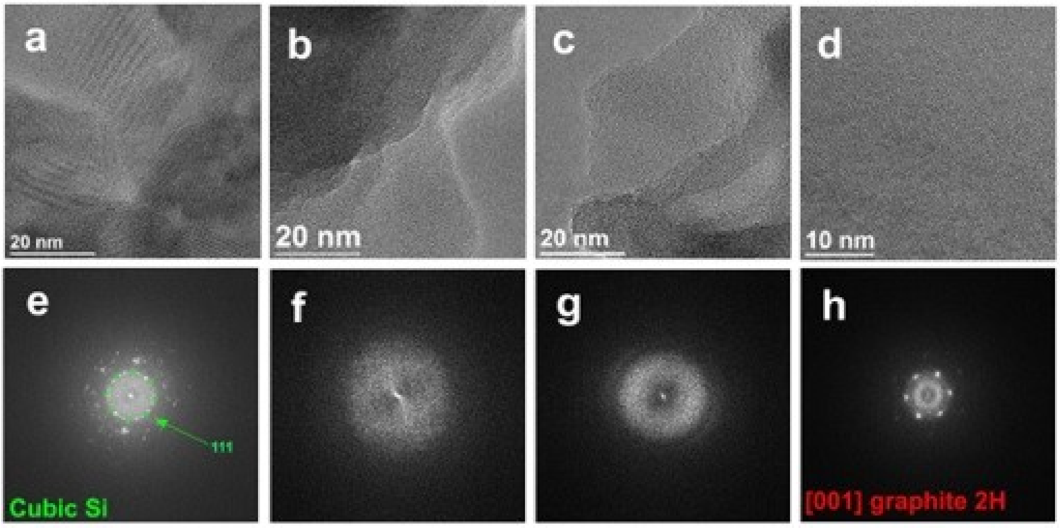

Figure 5.10: HRTEM imaging of (a-d) Si-graphene nanoparticles after (a) 1, (b) 10 and (c) 50 cycles and (d) after 100 cycles, with the corresponding FFT analysis (e-h) matching with (e) randomly oriented cubic silicon (ICSD 51688) nanometer-sized domains and (h) graphite (ICSD 76767). Image taken from [181].

40th cycle. With these results, it is possible to describe the composite as a high-energy density and long-life cycle anodes material, which is also capable to reach and maintain high current density.

5.2 Development of a Lithium-Ion battery

5.2.1 Cathode lithium cell performances

A commercial NMC111 (LiNi1/3Mn1/3Co1/3O2) was chosen as cathode with a nominal capacity of 2 mAh/cm^2. The cathode was first tested in lithium cell to evaluate its cycling performances. A galvanostatic cycling test was performed with a potential range of 3.0 - 4.2 V. Before the cycling, a forming cycle procedure is requested. A detailed description will be given further. After the forming cycles (cycles from #1 to #4) the specific capacity in Figure 5.11a seems to be stable. The Coulombic efficiency is around 99.0%. The potential profile of Figure 5.11b confirms the repeatability of the charge-discharge processes and show a stable specific capacity of 137 mAh/g, near the theoretically one (200 mAh/g) reached in the first charge. For the assembling of the Li-ion, the specific capacity of 137 mAh/g will be considered.

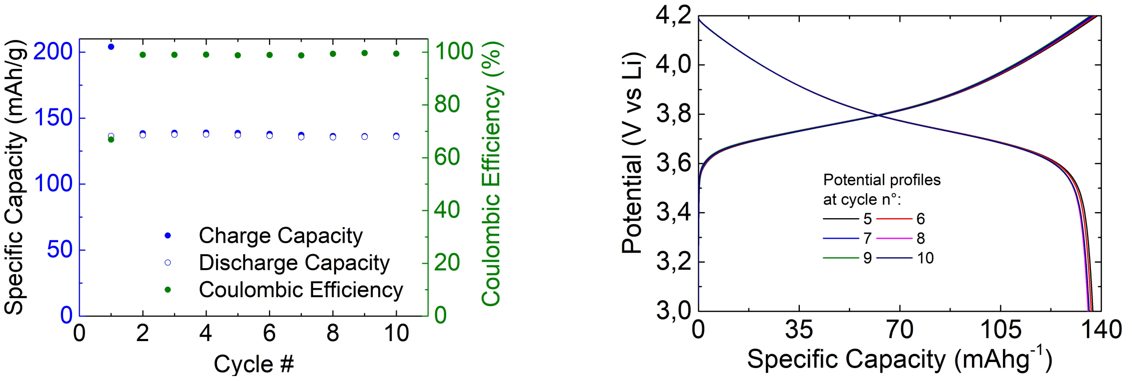

(a) (b)

Figure 5.11: Galvanostatic cycling (a) and potential profile (b) of NMC111. Image taken from [181].

5.2.2 Lithium-Ion cell assembling

The Li-ion cell here presented consisted of an experimental anode, the Si-FLG nanocomposite, and a commercial cathode, NMC111. From the electrochemical characterization presented in Figure 6 it is known that the anode has an areal capacity equal to 1.55 mAh/cm^2, while for the cathode is nominally 2.00 mAh/cm^2. Anode and cathode masses were balanced considering the anode reversible capacity (2300 mAh/g) and the reversible capacity of the cathode (137 mAh/g as reported in Figure 5.11). A coin cell 2032 type was assembled, using a spacer of glass fibre and LP30 EC:DMC 1:1 plus 10% in volume of FEC as electrolyte. The coin cell case was coated in Aluminium or Gold to assure the workability also for potential much higher than 3.0 V. A summary sketch is reported in Figure 5.12.

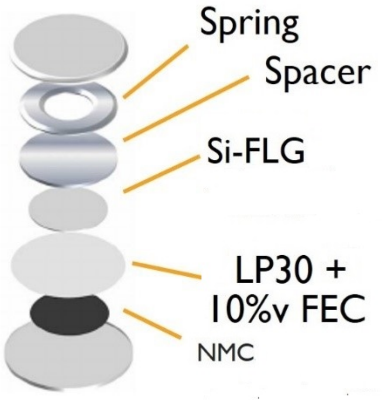

Figure 5.12: Exploded sketch of the Li-ion cell.

5.2.3 Potential range setting

In the choice of the cycling potential range, it is fundamental assuring that the anode relative voltage does not drop under 0 V. Otherwise, it takes place the lithium plating. In order to observe the trend of the anode relative voltage together with the cell potential range, a 3 electrode cell (EL-CELL ECC-REF) was assembled. In a three-eelctrode configuration, the cell and the anode voltages have been recorded at the same time during cycling. To do this, the ECC-REF is abel to arrange three different electrode, as well shown by the spare parts in Figure 5.13a: the working electrode (WE) and the counter electrode (CE), divided by the separator, have been placed as in a coin cell; the reference electrode, i.e. a Lithium chip, provides the voltage reference. In this configuration, the current flows through the WE and the CE, while it is possible to analyse the relative potential between of the cell or the relative ones of the anode (Si-FLG) or cathode (NMC111) simply by paring in the potentiostat the the WE and the CE together or individually with the reference electrode. The measurement, shown in Figure 5.14b, was carried out with a cell potential range of 3.0 - 4.2 V. As it is possible to directly verify, the anode voltage is always higher than 0.03 V. This means that 4.2 V is still a safe potential value, and that lithium plating is avoided. Starting from the measurement result, the potential range has been further regulated. Recalling the electrochemical reaction shown in Figure 5.8, it was considered 0.1 V as the minimum threshold for the working potential of the anode, since lower voltage values leads to non reversible reactions. This value has been already reached when the cell voltage is about 4.0 V. Therefore, the cell voltage should be limited up to 4.0 V instead of the most common 4.2 V. On the other extreme, the cell potential range of 3.0 V corresponds

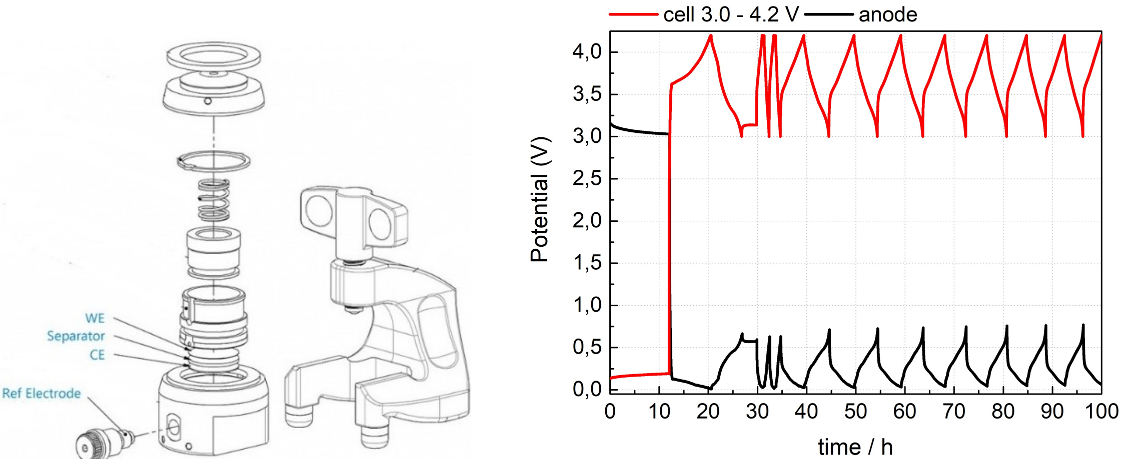

(a) (b)

Figure 5.13: (a) Spare parts of the EL-CELL 3 electrode test cell (ECC-Ref); (b) three-electrode potential range of the Li-ion cell.

approximately to a working potential of 0.67 V for the anode, a voltage sufficient to provide all the lithiation and de-lithiation process. However, for higher values of the anode voltage, the PITT measurement of Figure 5.8 does not show any reaction. Therefore, there is no risk increasing this value. Since the upper value of the cell potential range was decreased from 4.2 V to 4.0 V, it was decided to reduce in the same also the lower limit of 0.2 V (i.e. from 3.0 V to 2.8 V), in order to maintain the same potential difference as before.

5.2.4 Electrochemical characterization of the Li-ion cell

Finally, a complete lithium ion cell was assembled using silicon-FLG electrode as anode, a commercial NMC111, with a nominal capacity of 2 mAh/cm^2 electrode as cathode and LP30 + 10% v/v of FEC as electrolyte. The electrochemical behaviour of the as-assembled cell was tested by galvanostatic cycling in the potential range of 2.8 - 4.0 V, using a C-rate of C/2.
Figure 5.14a show the potential profile of the forming cycles. This formation procedure is made necessary to provide a stable electrode-electrolyte interphase and consisting of (i) a first charge to 4.0 V at C/10, followed by a potentiostatic step with a current cut off corresponding to C/20 and a first discharge at 2.8 V at C/10 (forming cycle #1, black) followed by a rest time of 3 h; then (ii) two charge-discharge cycles between 4.0 and 2.8 V at C/2 (forming cycles #2 and #3, respectively red and blue), with a potentiostatic step at 4.0 V with a current cut off corresponding to C/20; (iii) a final forming cycle (forming cycle #4, violet) with a charge cycle at C/10 up to 4.0 V, followed by a potentiostatic step with a current cut off corresponding to C/20, and a discharge cycle at C/10 ended at 2.8 V. It is interesting to

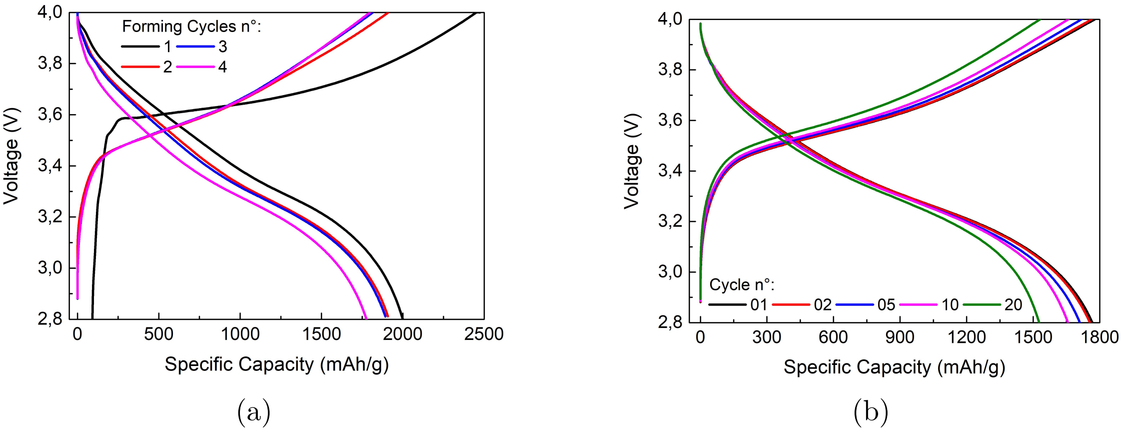

(a) (b)

Figure 5.14: Potential profiles of the li-ion cell: (a) forming cycles; (b) first 20 cycles. Specific capacity related to the Si mass content.

observe the reproducibility of cycles #2 and #3, which show a misalignment only in the charging phase, in its second half, while the discharging phases are substantially superimposed on each other.

After the forming cycles, the Li-ion cell was tested with a constant charge-discharge cycles at C/2, with a potential range of 2.8 - 4.0 V. The potential profile of the first 20 cycles are presented in Figure 5.14. Here it is possible to observe that the specific capacity is initially around 1800 mAh/g of Si, and after 20 cycles is still higher than 1500 mAh/g. It appears clear that there is no difference in the singular potential profiles. Simply, there is a loss of capacity on each cycle. Cycling performances reported in Figure 5.15 can help in the description of the behaviour.

Looking at the specific capacity all along the cycling, it is possible to observe a constant decrease of the specific capacity, that can be simply explained with a mean value of the coulombic efficiency around 99.4%. Therefore, it is clear why the specific capacity after 200 cycles is just one third of the initial value. Staying on the coulombic efficiency, it could be interesting to observe how the first coulombic efficiency has a value around 80.8% and increases in the rest of the forming cycles up to 98.9%.

In conclusion, these results in Li-ion cell test demonstrate that a such laminated silicon-FLG graphene nanocomposite fully works also in a full cell and represents a potential hybrid morphology for high silicon loading Li-ion cells displaying high-rate capabilities and excellent stability.

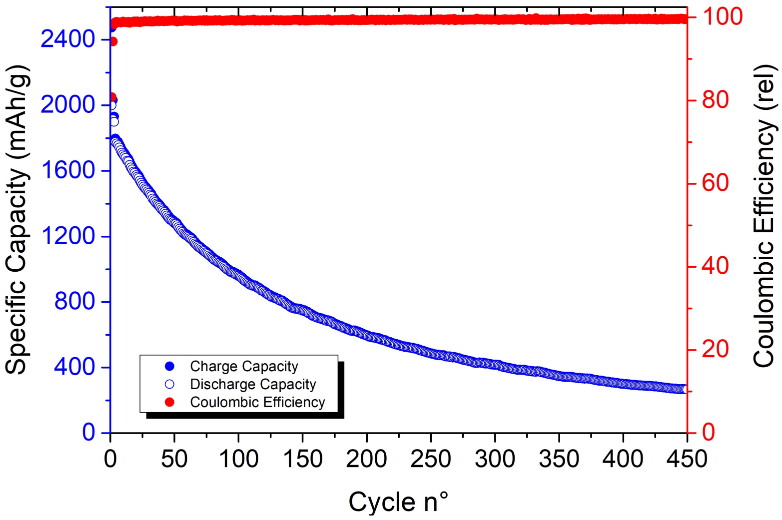

Figure 5.15: Specific capacity (blue) and Coulombic efficiency (red) vs cycle number plot. The specific capacity is related to the Si mass content. Image taken from [181]

Chapter 6

Vibrational Energy Harvesting device

6.1 Design of the conditioning circuit for the EH

Due to the increasing interest on energy harvesters, today there are a plenty of ready to use solution for the signal conditioning. Clearly, these solutions must be as generic as possible to have a chance to be commercially winning and applied to different harvester types. As one example, it is worth to mention the LTC3588-1 integrated circuit produced by Analog Device, which has the dimension of a 0.20 € coin, specifically conceived for piezo harvester but applicable to thermal and magnetostrictive devices. It is also possible to find cheaper solutions provided by all the additional passive components. The device presents several interesting features, such as the digital output PGOOD, which returns a positive digital signal when voltage output is on, and the two digital input channel D_0 and D_1, which can be used to regulate the output voltage. As shown in Figure 6.1, the core of this conditioning circuit is constituted by the bridge rectifier, connected to the input channels PZ_1 and PZ_2, the smart voltage regulator chip and the input/output channel Vin, where it is possible to connect the storage unit. The functioning of the circuit is quite simple: (i) the output voltage coming from the harvester passes in the rectifier bridge, where it is converted from ac to dc; (ii) the rectified signal is then sent to the channel V_{in}, where it starts charging the storage unit; (iii) when Vin is higher than 5 V, the voltage regulator “open” the internal switch and let the current going to the Vout channel, with a constant level previously set by channels D_0 and D_1. This commercial solution has a couple of advantages: it is a plug&play device and the output voltage is constant and can be a priori settled. On the other hand, the minimum voltage level required by the device is a severe issue that could limit its applicability, since it requires 2.5 V to start charging the storage unit, and until V_{in} is less than 5.0 V, the V_{out} channel is off.

The voltage supply represents a non-negligible issue in the case study presented

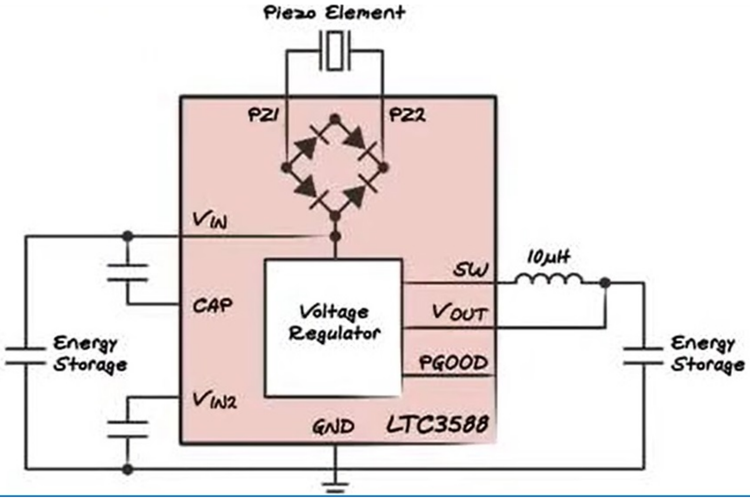

Figure 6.1: The LTC3588 scheme.

in this work, since from a magnetostrictive device the common output voltage is usually between 0.5 V and 2.0 V. Moreover, a Li-ion cell working voltage is usually below 5.0 V, in the range between 3.0 and 4.2 V and it is difficult to design a battery working at higher voltages. Although there are circuits suitable for the case study on the market (e.g. the ADP5091, see `https://www.analog.com/media/en/technical-documentation/data-sheets/ADP5091-5092.pdf.`), it was decided to design a home-made conditioning circuit starting from the scheme of the LTC3588. The priority was given to a conditioning circuit capable of rectifying the output voltage from the harvester. If the signal to be rectified had a voltage of several volts, it would be enough to use a simple rectifier bridge as already seen in the LTC3588 circuit. However, in the case of lower power signals, some precautions must be taken, since the DC output voltage is generally limited by the peak value of the sinusoidal input voltage. By using combinations of rectifier diodes and capacitors together, it is possible not only to rectify the voltage, but also effectively multiply it to some odd or even multiple of the peak input voltage. About this, it is worth mentioning the voltage quadrupler of Figure 6.2.

A voltage quadrupler is a rectifier bridge in which the capacitors are used to store energy during a half-wave phase. The diodes, driving the current during the two half-wave phases, select directly which capacitor is charged and the path followed to discharge in the following phase. The capacitors under charging are not allowed to discharge directly, since there is no path possible. Only during the subsequent phase, they find a path to discharge. Theoretically, at the end of the process it should be possible to obtain an output voltage 4 time greater than the input voltage peak. But this is true only with high voltage ($V > 10V$) pulses. In all other cases, the voltage drop due to the diodes must be taken into account, and the output voltage is no more able to reach the theoretical value.

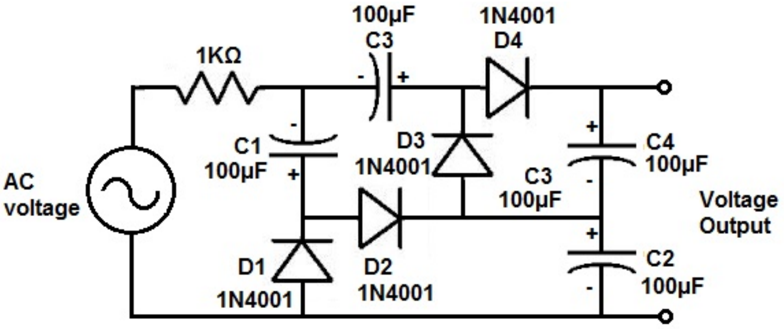

Figure 6.2: Voltage quadrupler circuit.

A voltage multiplier was realised following the scheme of Figure 6.2. It was used four 100 μF EDL (Electrical Double layer) capacitors and four small signal Schottky Diodes (1N5711). Since the generator is a real one, the 1 kΩ resistance is no more necessary. To verify the voltage response of the rectifier, the signals coming from the harvester and from the rectifier were collected and showed in Figure 6.3.

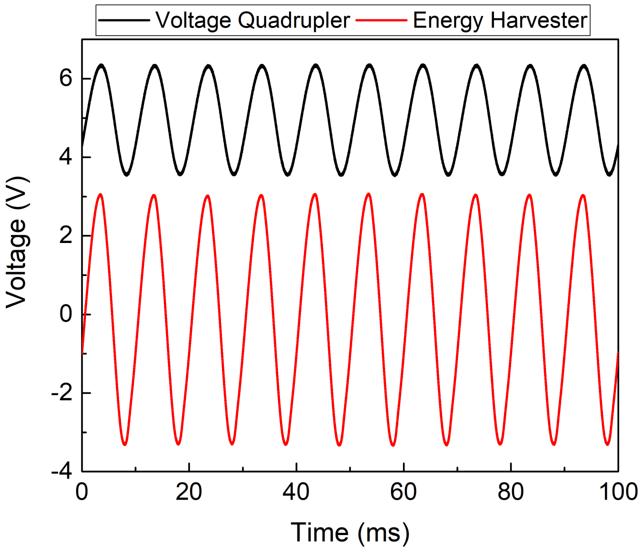

Figure 6.3: Superposition of the output voltage from the harvester (red) and after the conditioning (black).

The harvester output voltage has a frequency of 100 Hz, such as the mechanical vibration applied by the material testing machine. The peak value is about 2.50 V, with a rms value of 2.24 V. At the rectifier output, the voltage is a dc voltage with a significant ripple. As a proof of the result, a small EDLC of 0.5 mF was added in parallel to the output. The result of its charging is shown in Figure 6.4.

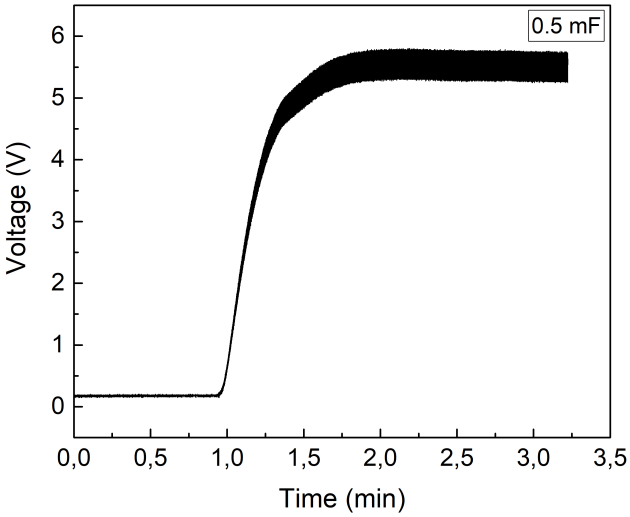

Figure 6.4: Charging cycle of a 0.5mF EDLC placed as a load of the rectifier.

It is possible to see that in less than 2 minutes the EDLC is charged to a value higher than 5.5 V, starting from a rms value of the harvester output voltage equals to 2.42 V. The voltage is more than doubled and it acts as a dc signal with ripple and it charges the capacitor. Anyway, due to the small capacitance of the EDLC, the voltage ripple is still considerable.

6.2 Stress test of the vibrational energy harvesting device

6.2.1 Introduction

Having demonstrated that the rod of Fe-Ga is able to charge a small capacitor with the help of a rectifier, it is now possible to start the design of the complete vibrational energy harvesting device. Following on the scheme presented in the introductory chapter, it is possible to schematize the device into four principal units:

- Energy source
- Conditioning circuit
- Energy storage unit
- Sensor

The energy source will be a mechanical vibration applied by the Instron E-10000 testing machine. The vibration has a frequency of 100 Hz, the suitable mechanical preload is 1690 N and an amplitude of the vibration is set to 340 N, which is realistic for applications. The magnetic field bias is guaranteed by a couple of permanent Nd-Fe-B magnets.

The conditioning circuit is represented by the voltage quadrupler described above. For what concerns the energy storage unit, the first tests will involve the use of an EDL capacitor. Only in a second phase, the use of Li-ion cell will be tested.

The harvester load is represented by a Bluetooth Low Energy (BLE) sensor capable to transmit information on temperature, humidity and acceleration through a bluetooth antenna to a receiver that is, in our case, a smartphone. The sensor is set to send a signal each second. In this way, the discharging period will be reduced to a laboratory scale. Normal use provides longer period, usually no less than one signal per minute.

Working on the capacity of the EDLC, it is possible to envisage two different use of the sensor. The first one, supposes the presence of a continuous vibration which would be interrupted only short stand-by periods. The second case study envisages a significantly long period of vibration (tens of hours or days) followed by a period in which the sensor must be supplied only by the energy storage unit.

6.2.2 Device with stand-by periods

The first case study is centred on a situation in which the vibration is provided continuously by the source. In this case, the absence of vibration must be seen as an occasional break. For this purpose, a small capacitor with a capacity of 1.5

mF has been used as storage unit. The stress test results are represented in the diagram of Figure 6.5.

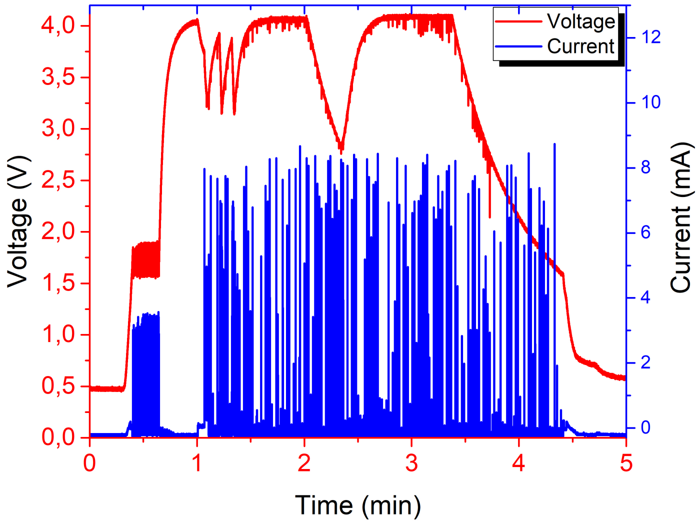

Figure 6.5: Charging and De-charging stress test of a 1.5 mF EDLC. Voltage level of the EDLC (red) and current absorbed by the BLE sensor (blue).

The stress test is subdivided into 5 phases:

- Charging of the capacitor
- Power on the sensor
- Brief interruption of the vibration
- Recovery of the vibration
- End of the vibration

During all the stress test, the red curve indicates the voltage of the capacitor, while the blue curve represents the current absorbed by the sensor.
The first charging phase takes a time of about 1 minute. It is possible to observe that, also if the sensor is off, when the capacitor reaches a voltage of about 1.7 V there is an absorption of power by the sensor circuits for few seconds, maybe due to internal capacitance. After this brief period, no more current is absorbed and the capacitor can achieve a full charge. At this point, the sensor is powered on, and it start to send periodic signal to the receiver, as demonstrated by the peaks of absorbed current. The voltage remains a bit unstable for a while (about 30 seconds) with oscillations of about one volt. When the vibration stops (around

min 2) it is possible to observe that the capacitor is able to supply alone the sensor for a period of about 30 seconds, in which its voltage passes from 4.0 V to 2.75 V. During this period, the sensor continues to send signal to the mobile phone every second, and when the vibration is recovered, the capacitor comes back to a full charge condition without affecting the sensor. When the vibration is definitely suspended, the sensor enter three different phases: (i) with a voltage higher than 2.6 V, the sensor works in normal conditions; (ii) immediately below 2.6 V, the incorporated antenna still continues send message to the receiver, but without any values visible on the smartphone since the sensor is powered off; (iii) with a voltage lower than 1.75 V, the antenna does not have the power to sends message, and the entire device stops working.

With this configuration, the capacitor is able to supply the sensor for a limited period of time, avoiding false negative due to limited drop of voltage. Therefore, an interruption of the signal from the sensor may suggest a severe interruption of the vibration, maybe due to a damage (both of the sensor as of the energy source).

6.2.3 Long-time vibration

A completely different case study is that where the vibration has a long-time duration followed by an equally long period of interruption. It could be the case of an industrial machine tool used as vibration source that works all over the day and stops during the night or during holidays. To verify the applicability of the harvesting device, it is important to test if a long period vibration affects the sensor or the energy storage unit. For this reason, the stress test simply provides two phases: in the first phase, the vibration is guaranteed for 24 hours, while in the second phase it is tested how long the energy storage unit is able to supply the sensor. For this test, an EDLC supercapacitor of 3.0 F was employed. The result is shown in Figure 6.6.

In the first phase, the supercapacitor needs 6 hours to reach a satisfactory charge of about 3.5 V, then the voltage continues to increase asymptotically even if the BLE sensor continues to transmit every second. At the end of the 24 hours, the vibration is powered off, and the sensor is supplied only by the supercapacitor. In about 4 hours, the voltage drops below the critical value of 2.6 V, and it takes other 8 hours to reach a voltage lower than 2.0V, after that all the sensor device is powered off. After that, it is possible to observe a constant loss of potential absorbed by several passive elements. From this stress-test it is possible to derive some interesting data. First of all, a long-time vibration does not affect negatively the energy storage unit or the sensor. If it is a reasonable result for a supercapacitor, the same cannot be said for the sensor, which is designed to work with 3.0 V coin battery. In this test, the sensor is supplied for more than 20 hours with a voltage higher than 3.5 V. Second, the supercapacitor is able to supply the sensor for 4 hours, which is a satisfactory span. In fact, considering that the transmission period would be one

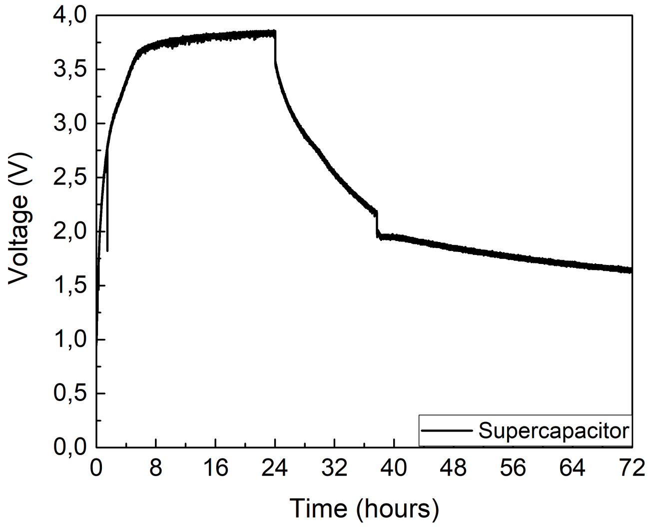

Figure 6.6: Long-time stress-test of an EDLC supercapacitor (3.0 F).

or few minutes in a real application, this means that the autonomy scale of the system in a real application is of the order of 10 days or more.

6.2.4 Use of a Li-ion cell as storage unit in a Vibrational Energy Harvester

The final and most interesting step has been the implementation of the Li-ion cell, described in chapter 5, as storage unit in the harvesting device. The Li-ion cell has a starting potential of 2.8 V coming from the forming cycles. In order to reproduce the testing cycling condition of the prototypal Li-ion cell, it is necessary to apply a voltage range between 2.8 and 4.0 V, and the current should be limited up to around 1 mA, which is the current applied during the galvanostatic tests (corresponding to a C-rate of C/2). For what concerns the voltage range, the lower limit can be equal to the voltage threshold of the sensor, while a voltage value higher of 4.2 V could lead to non-reversible reactions in the anode (more detail can be found in paragraph 5.2.3). Looking to the applied current, slightly exceeding the threshold of 1.0 mA leads to a loss in the cell capacity and a detrimental effect in reaching the full charge (as shown in Figure 5.5a). However, in this configuration the mean current generated by the harvester is about 30 mA, and such a current, capable to fully charge the cell in just 4 minutes, could damage the cell. This issue does not appear when the EH supply directly the BLE or through the supercapacitor. In the case of the battery, for the above reasons, it is necessary to limit both the voltage and the current. A simple solution could be represented by a small resistor of 47 Ω added in series at the output of the voltage quadrupler, which can ensure a current lower than 1 mA to the cell. Clearly, in a real market conditioning circuit a voltage and current limit is ensured in a more sophisticated way. The harvesting device has been than submitted to a first stress test, which was composed by three different phases. The Li-ion cell voltage during all the stress tests is shown in Figure 6.7.

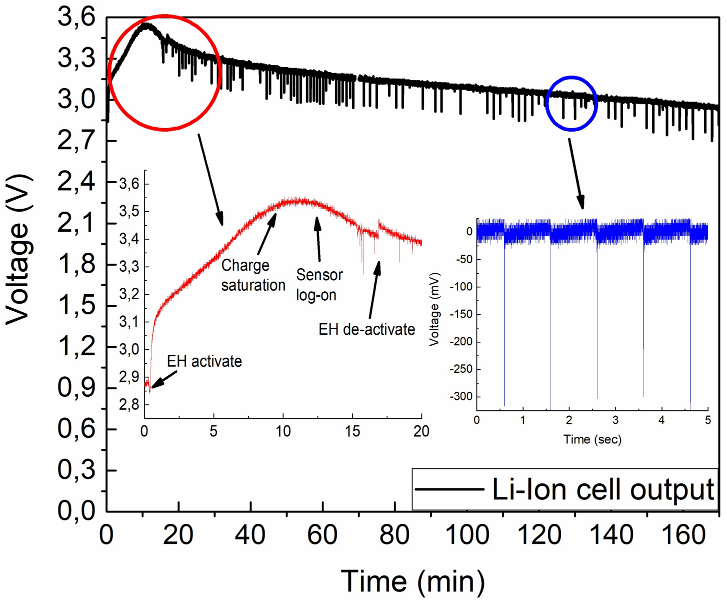

Figure 6.7: Charging and discharging stress test of a Li-ion cell. In the inset: (red) Voltage of the Li-ion cell during the different stress test phases; (blue) the periodical peak voltage drops due to the power absorption by the BLE sensor.

The first phases aimed at verifying if the suitability of the harvester in charging the Li-ion battery. The second one aimed at assessing if the Li-ion cell is capable, and for what time, to supply alone the sensor.

In the figure the two insets have been added for sake of clarity. The one on the left allows one to have a close-up vision of the first phase, while the other one on the right is just a proof that the sensor is working. This is also the reason for which the potential is expressed relatively to the initial value of the inset. In this way, it is possible to estimate the potential absorbed by the sensor in sending the signal to the receiver.

The first phase shows that the Li-ion cell takes about 10 minutes to reach the saturation. The profile of the potential seems to indicate a constant charge process of the cell. The sensor is powered on, while the harvesting is still supplying current to the system. No appreciable process seems to appear, but a significantly loss in the potential due to the power absorbed by the sensor in its activation. Finally,

the vibration has been stopped, and only the Li-ion cell is in charge to supply the sensor. It is possible to observe that the potential is maintained higher than 2.8 V for more than 150 minutes versus a period of charge of only 10 minutes. The test was stopped at a potential of 2.8 V which is the cycling lower limit of the cell.
Looking at the results of Figure 6.7, it is possible to state that the harvester was able to charge the Li-ion cell and, in contemporary, to supply the sensor. Moreover, the charging process does not affect negatively the cell, since it had been supplying the sensor for a long time. Lastly, the Li-ion cell can supply the sensor for more than 150 minutes. Also in this case it should be remembered that in a real application the transmission interval is not a second, but typically it is two orders of magnitude higher and therefore the battery life would exceed 10 hours without the input of the vibration. Furthermore, it should be remembered that the battery in question is an experimental battery, and that its capacity is only 1% of a commercial CR2032 battery. In this regard, see also `https://data.energizer.com/PDFs/cr2032.pdf`.
It was decided to design a second stress test, in which the cell is still charged at a potential value higher than 3.0 V. After activating the sensor, and verifying the cell is capable to supply the sensor, the harvester has been active and then again stopped. The results are shown in Figure 6.8.

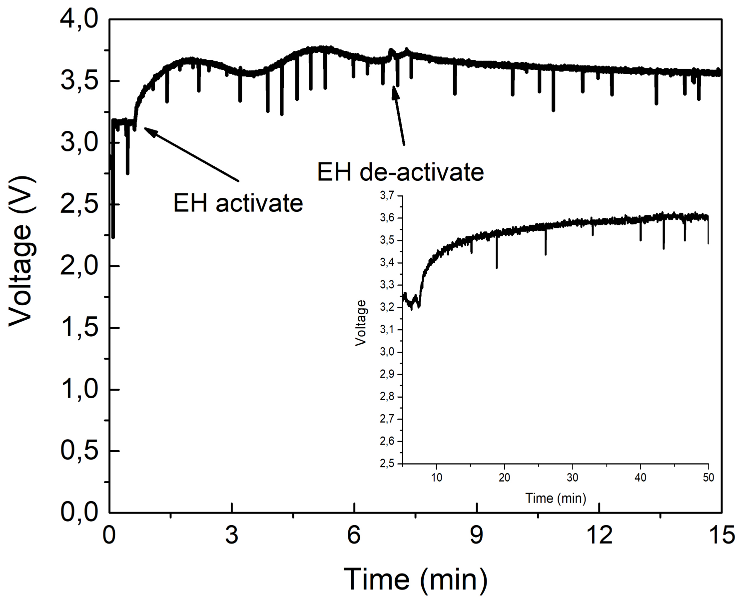

Figure 6.8: Charging and discharging of the Li-ion cell. In the inset, the Li-ion cell is coupled with a small (1.5 mF) EDLC to reduce the voltage ripple.

The test wants to reproduce the situation in which the vibration was interrupted for a period and then taken back. The last period without vibration has just the purpose to verify the cell is still working. It is possible to observe that the cell seems not able to reach the full charge directly but suffers of a drop voltage at the end. This could be due to the voltage ripple affecting the rectifier. In the inset is proposed a possible solution, in which a small capacitor, 1.5 mF, is coupled with the cell. In this configuration, the capacitor should filter the voltage coming from the rectifier giving a voltage like the one showed in Figure 6.5. The new results show a better definition of the charging of the cell, which now is capable to reach the saturation without suffering the effects of the voltage ripple.

6.3 Discussion

In this chapter we briefly discussed the advantages and disadvantages of using commercial systems for signal conditioning. In the case of magnetostrictive EHs the output voltage is not so high and can be lower than 5 V in specific operating conditions. This inhibits the operation of the most common conditioning circuits. Furthermore, the output voltage must also be limited, especially if one uses experimental Li-Ion batteries such as the one analyzed in this thesis work. Thus, a home made conditioning circuit has been created, based on a voltage quadrupler. The circuit has proven to work effectively with both supercapacitors and the experimental Li-Ion battery.

In the second part of the experimentation, a supercapacitor and the Li-Ion battery were used. Using a BLE sensor transmitting with Bluetooth protocol on a smartphone, a series of experiments were made. In order to reach a laboratory time-scale, the transmission period of the BLE has been set to one second, while in real applications it can be one or a few minutes. It has been observed that a supercapacitor can cover, in real applications, a period of transient non-operation of the vibration source, up to covering an entire work shift (about 12 hours). It has also been shown that the experimental battery can do the same and that, if returned to the nominal capacity in the future, it will cover periods of non-operation of the source of the order of the year or more.

Chapter 7

Conclusion

The realization of the harvesting device showed above has required great efforts in terms of experimental measures and project management. Due to the multi-discplinarity level required, the design of all components of the device has been a challenge. The single component (which can be briefly identified as harvester, Li-ion battery and conditioning circuit) does not share any element with the others but the final concept.

The work was focused on the two main component of the device, the harvester and the Li-ion cell.

The study of the magnetostrictive material had the goal to realize a set of preliminary values useful to the design of the harvester starting from the energy source behaviour. The goal was reached in two different but complementary ways: a simulation code based on the Preisach model and a long campaign of experimental measurements through the use of a magnetizer and of a material testing machine. The successfully simulation of the magnetostrictive properties of the FeGa alloy allow to find the best working condition in terms of magnetic bias, mechanical preload and resistance load. Adding the behaviour of the vibrational source, the code is also able to provide a reasonable estimate of the output performance of the harvester, in particular the electromotive force. From the latter, is quite easy to obtain the output current and therefore the output power generated by the harvester. On the other hand, the use of a magnetizer combined with a material testing machine, has given as one of the most significant results the curves family of Figure 3.6. A complete study of the combined effect on the output performances of the magnetic bias and of the mechanical preload has been achieved, and it was demonstrated that for each mechanical preload, it exists a value of the magnetic bias which can maximize the output power of the harvester. The results of Figure 3.6 may be seen also seen backward. For each value of magnetic bias, there is a mechanical preload capable to maximize the output power. It has been highlighted that, with lower value of magnetic bias it is possible to reach performances comparable with the ones obtained with higher magnetic bias. This information is important when one is using permanent magnets, since the design of the harvester has the constraint due to magnetic bias, which is generally quite low. Setting accordingly the mechanical preload it is possible to reach the best performance possible. Therefore, a second set of experimental measurements carried on a second magnetic yoke with permanent magnets instead of coils (see Figure 3.10) confirmed the results of the investigation. The results obtained with permanent magnets as source of the magnetic bias has been in accordance with the ones previously obtained with the magnetizer, so demonstrating that the experimental set-up and the related results could also been used to design the harvester, by means of a numerical code.

Parallel to the study of the FeGa alloy properties, the design of a new Si-Graphene nanocomposite based anode material has been carried out in order to realize the energy storage unit. The nanocomposite represents an optimal way to combine the high specific capacity of the Silicon with the high stability and long life cycling of the carbon materials. The goal was not only to obtain a valuable anode material, but also to do it with a process scalable from the laboratory level to industry. This means that the process must have been as simple as possible, avoiding complex and expensive laboratory equipment (such as C.V.D. techniques) and non-environmental friendly elements, substituting for example the NMP with ethanol as solution the sonication. Moreover, the entire procedure from the single components to the final anode realization must have been as quick as possible. The results has been interesting. The procedure takes less than 8 hours on in laboratory, and could also been speed-up once scaled at the industrial stage. Moreover, all the passages requires simple instruments starting from the powder mixing to the annealing process passing through a sonication. Everything can be reproduced in an industry without paying pledge in terms of final performance or material quality. From a strictly electrochemical point of view, the new anode material has proven to possess high stability and to be able to work also at high current (7.0 A/g). Increasing the mass load, the anode material showed these behaviours both as a thin film and as a bulk material, and it reaches and overcomes the areal capacity of the highest performing cathode on the market (2.5 mAh/cm^2). Due to these performances, the anode was subsequently used in a Li-ion cell together with a commercial cathode (NMC 111). It was so possible to realize a Li-ion cell, subsequently used as energy storage inside the harvesting device. The study of the electrochemical performances has been accompanied by a deep morphological, chemical and physical analysis. It was demonstrated that the annealing process not only does not affect the morphology of both silicon nanoparticles and graphene flakes, but it leads to the creation of a carbon-coating on the silicon nanoparticles, which is able to increase to conductivity of the material and buffer the volume expansion of the particles. Moreover, the cycling behavior of the anode material in half-cell test was deeply analysed through SEM and TEM imaging of post-mortem samples. It was so possible to study the morphological evolution of the Silicon nanoprticles during all the cycling, passing from a crystalline morphology to an amorphous one.

At the end, a coupling and conditioning circuit has been proposed for the harvester, the latter being able to successfully load the storage component. It has been shown that both a supercapacitor and the built for the purpose rechargeable battery can be used as a storage element. In applications such as those on machine tools, when the vibration source shows inactivity cycles (lack of vibration) this can be easily overcome by tuning the system storage system and by adjusting the transmission period of the sensor connected to the harvester. In this case, the use of a supercapacitor may be sufficient. In the case of the experimental rechargeable battery, which at the moment has a very small capacity (1.57 mAh), it is possible to power the transmitter with a single full charge for several years by using the same battery made with a common rated capacity (200 mAh). The improvement of the experimental battery presented in this thesis work will be the continuation of this research.

During this thesis work development, the following publications have been achieved:

- S. Palumbo, P. Rasilo and M .Zucca, Experimental investigation on a Fe-Ga close yoke vibrational harvester by matching magnetic and mechanical biases, *Journal of Magnetism and Magnetic Materials*, 469, 2019, 354-363, `https://doi.org/10.1016/j.jmmm.2018.08.085`.

- S. Palumbo, L. Silvestri, A. Ansaldo, R. Brescia, F. Bonaccorso, and V. Pellegrini, Silicon Few-Layer Graphene Nanocomposite as High-Capacity and High-Rate Anode in Lithium-Ion Batteries, *ACS Applied Energy Materials*, 2(3), 2019, 1793-1802, `https://doi.org/10.1021/acsaem.8b01927`.

- U. Ahmed, J. Jeronen, M. Zucca, S. Palumbo and P. Rasilo, Finite element analysis of magnetostrictive energy harvesting concept device utilizing thermodynamic magneto-mechanical model, *Journal of Magnetism and Magnetic Materials*, 486, 2019, 165275, `https://doi.org/10.1016/j.jmmm.2019.165275`.

- S. Palumbo, M. Chiampi, O. Bottauscio and M. Zucca, Dynamic Simulation of a Fe-Ga Energy Harvester Prototype Through a Preisach-Type Hysteresis Model, textitMaterials, 2019, 12(20), 3384, `https://doi.org/10.3390/ma12203384`.

- U. Ahmed, U. Aydin, M. Zucca, S. Palumbo, R. Kouhia and P. Rasilo, Modeling a Fe-Ga energy harvester fitted with magnetic closure using 3D magneto-mechanical finite element model, *Journal of Magnetism and Magnetic Materials*, 2020, 500, 166390, `https://doi.org/10.1016/j.jmmm.2020.166390`.

Appendix A

Thermodynamic demonstration of the magnetostrictive properties

There exist several approaches to demonstrate the magnetostrictive properties of a material, but it has been choosen a thermodynamic model [194] due to its simplicity.

As for the first ones [195], the model is linear. This is a non negligible assumption, but it is supported by a reasonable linearity of general magnetostrictive materials under moderate exitations. Moreover, it is possible to calculate effective algorithms with a linear mathematical treatment. A second important assumption of the model is that the materials have reversible properties, i.e. hysteresis effects have been neglected.

Definition of Stress and Strain In order to share a common start point, the definition of stress and strain it is first reviewed [196], starting from a general 3D geometry to a 2D-longitudinal one. Lets take a volume element from a magnetostrictive material subjected to a general stress, as shown in Figure A.1

The forces acting on the unit cube can be subdivided in two types: body forces and forces acting on the surface.

Body forces are the ones acting throughout the body and have a magnitude proportional to the volume. This means that if the volume is infinitesimal, such for a unit cube, these forces can be neglected. Example of body fores are gravitational or electromagnetic interation.

The forces acting on the surface, otherwise, are due to the volume element with the surroinding material. A force acting on a unit are defines a stress tensor, $[T_{ij}]$:

$$[T_{ij}] = \begin{bmatrix} T_{11} & T_{12} & T_{13} \\ T_{21} & T_{22} & T_{23} \\ T_{31} & T_{32} & T_{33} \end{bmatrix} \tag{A.1}$$

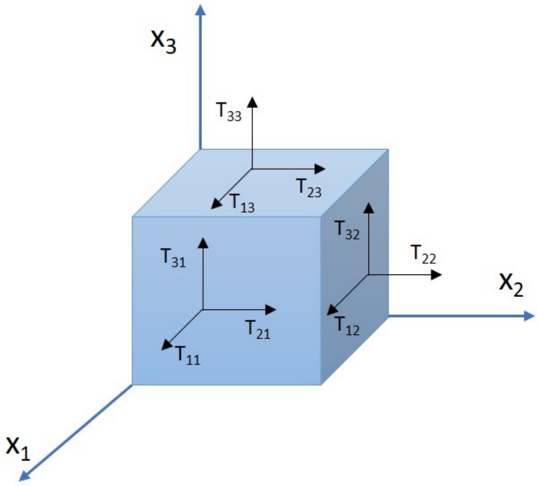

Figure A.1: The forces on the faces of a unit cube in a stressed body [194]

As demonstrated by *Nye* [196], the general stress tensor $[T_{ij}]$ becomes symmetric due to the absence of contribution of the body forces. Hence, in the stress tensor will remain only six indipendent elements, and it becames convenient to convert the stress tensor from in the form a vector. The relation between tensor and vector notations is shown in Table A.1

Table A.1: The relation between the indices in the tensor and vector notations

Tensor notation	11	22	33	23,32	31,13	12,21
Vector notation	1	2	3	4	5	6

Once it is defined a stress vector, it is necessary to define also a strain vector. In two dimension, the deformation of the body defines the following quantities:

$$e_{11} = \frac{\partial u_1}{\partial x_1}; \quad e_{12} = \frac{\partial u_1}{\partial x_2}; \quad e_{21} = \frac{\partial u_2}{\partial x_1}; \quad e_{22} = \frac{\partial u_2}{\partial x_2}; \tag{A.2}$$

Using the Einstein's summation convention, the same quantities became:

$$e_{ij} = \frac{\partial u_i}{\partial x_j}(i, j = 1{,}2{,}3) \tag{A.3}$$

But the tensor $[e_{ij}]$, as shown in Figure A.2 can be represented as the sum of a strain plus a rotation. So, it is not adequate to represent the strain of a deformed body. Indeed, a mere rotation of the body (i.e. a rotation without any deformation) leads $e_{ij} \neq 0$ for $i \neq j$. Therefore, it is necessary to decompose the contribution of

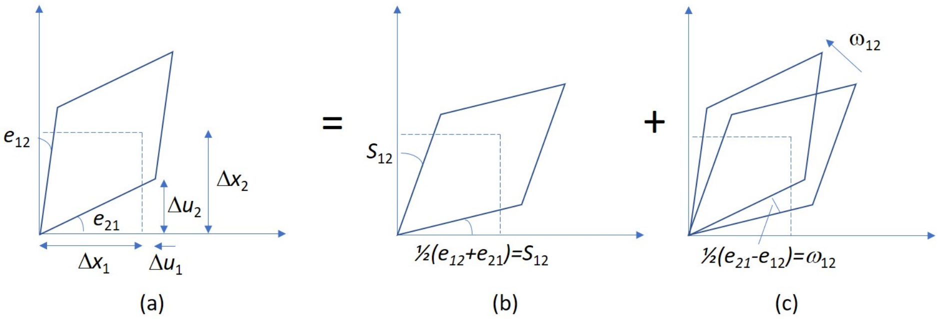

Figure A.2: Undeformed (dashed) and deformed (solid) body. The general defrmation shown in (a) can be represented by a strain (b) plus a rotation (c) [194]

$[e_{ij}]$ into the two vector representing a pure strain $[S_{ij}]$ and a pure rotation $[\omega_{ij}]$:

$$[S_{ij}] = \begin{bmatrix} S_{11} & S_{12} & S_{13} \\ S_{21} & S_{22} & S_{23} \\ S_{31} & S_{32} & S_{33} \end{bmatrix} = \begin{bmatrix} e_{11} & \frac{1}{2}(e_{12}+e_{21}) & \frac{1}{2}(e_{13}+e_{31}) \\ \frac{1}{2}(e_{12}+e_{21}) & e_{22} & \frac{1}{2}(e_{23}+e_{32}) \\ \frac{1}{2}(e_{13}+e_{31}) & \frac{1}{2}(e_{23}+e_{32}) & e_{33} \end{bmatrix} \tag{A.4}$$

We can see that the tensor $[S_{ij}]$ is composed by the symmetrical part of the tensor $[e_{ij}]$. The shear strains is represented by the off-diagonal elements, which corresponds only to one-half of the angle change between the defrmed body and the undeformed one.
Indeed, the rotation tensor $[\omega_{ij}]$ is represented by the anti-symmetric part of the tensor $[e_{ij}]$:

$$[S_{ij}] = \begin{bmatrix} \omega_{11} & \omega_{12} & \omega_{13} \\ \omega_{21} & \omega_{22} & \omega_{23} \\ \omega_{31} & \omega_{32} & \omega_{33} \end{bmatrix} = \begin{bmatrix} 0 & \frac{1}{2}(e_{12}+e_{21}) & \frac{1}{2}(e_{13}+e_{31}) \\ \frac{1}{2}(e_{12}-e_{21}) & 0 & -\frac{1}{2}(e_{32}-e_{23}) \\ -\frac{1}{2}(e_{13}-e_{31}) & \frac{1}{2}(e_{32}-e_{23}) & 0 \end{bmatrix} \tag{A.5}$$

So $[e_{ij}] = [S_{ij} + \omega_{ij}]$.
Another important characteristic of the strain tensor $[S_{ij}]$ is its symmetry; therefore, like the stress tensor, it has only six independant elements and, using the same relation above exposed, can be expressed as a six-component vector.

Energy and Work of Magnetostrictive Materials If a magnetic flux density dB magnetizes a unit volume of a magnetostrictive material, it generates a magnetic work dW

$$dW_b = H_m dB_m \quad (m = 1{,}2{,}3) \tag{A.6}$$

If an isothermal and reversible mechanical strain process is acting on the same unit volume, it delivers a mechanical work:

$$dW_s = T_i dS_i \quad (i = 1, \ldots, 6) \tag{A.7}$$

If, in our reversible system, the unit volume is subjected to both the above situations, the increase of internal energy dU is given by:

$$dU = T_i dS_i + H_m dB_m \tag{A.8}$$

For adiabatic condition, the Gibbs energy can be written as:

$$G = U - T_i S_i - H_m B_m \tag{A.9}$$

By differentiation, for reversible process, one gets:

$$dG = dU - dT_i S_i - dH_m B_m - T_i dS_i - H_m dB_m = -S_i dT_i - B_m dH_m \tag{A.10}$$

which gives:

$$S_i = \left.\frac{-\partial G}{\partial T_i}\right|_H ; \qquad B_m = \left.\frac{-\partial G}{\partial H_m}\right|_T \tag{A.11}$$

If we now take the partial derivative of S_i (with respect to H_m) and of B_m (with respect to T_i), we would obtain:

$$\left.\frac{\partial S_i}{\partial H_m}\right|_T = \left.\frac{\partial B_m}{\partial T_i}\right|_H = d_{mi} \tag{A.12}$$

where $d_{mi} = \frac{-\partial G}{\partial T_i \partial H_m}$.

Since for the magnetostrictive materials the most common mode of operation is the longitudinal mode, the applied magnetic field and stress have only components in the $m = 3$ direction. So, equation A.12 becames:

$$\left.\frac{\partial S_3}{\partial H_3}\right|_T = \left.\frac{\partial B_3}{\partial T_3}\right|_H = d_{33} \tag{A.13}$$

where $S_3 = S_33$, $T_3 = T_33$, $B_3 = B_z$ and $H_3 = H_z$.

Magnetomechanical Coupling A characteristic property of magnetostrictive materials is that a mechanical strain will occur if theey are subjected to a magnetic field in addition to strains originated from pure applied stress. Also, their magnetization changes in applied mechanical stresses due to changes caused by changes of the applied magnetic field.

These dependencies can be described by mathematical function if one assumes that the material shows reversible properties:

$$\begin{aligned} \vec{S} &= \vec{S}(\vec{T}, \vec{H}) \\ \vec{B} &= \vec{B}(\vec{T}, \vec{H}) \end{aligned} \tag{A.14}$$

differentiation of the previous equations and using the previous defined notations give:

$$\begin{aligned} dS_i &= \left.\frac{\partial S_i}{\partial T_j}\right|_H dT_j + \left.\frac{\partial S_i}{\partial H_k}\right|_T dH_k \quad (i, j = 1, \ldots, 6) \\ dB_i &= \left.\frac{\partial B_m}{\partial T_j}\right|_H dT_j + \left.\frac{\partial B_m}{\partial H_k}\right|_T dH_k \quad (m, k = 1, 2, 3) \end{aligned} \tag{A.15}$$

In this equation system is possible to identify the magnetostrictive constant d_{mi} ($d_{mi} = d_{im}$ by symmetry).
More over, it is common to denote constants of compliances and permeabilities accordig to:

$$\begin{aligned} \left.\frac{\partial S_i}{\partial T_j}\right|_H &= s_{ij}^H \qquad \text{elastic compliances at constant H} \\ \left.\frac{\partial B_m}{\partial H_k}\right|_T &= \mu_{mk}^T \qquad \text{magnetic permeabilitis at constant T} \end{aligned} \tag{A.16}$$

For small variation in $d\vec{T}$ and $d\vec{H}$, the linearized constitutive equations A.15 can be formulated as:

$$\begin{aligned} S_i &= s_{ij}^H T_j + d_{ki} H_k \quad (i, j = 1, \ldots, 6) \\ B_m &= d_{mj} T_j + \mu_{mk}^T H_k \quad (m, k = 1, 2, 3) \end{aligned} \tag{A.17}$$

Several coefficient in equation A.17 may be zero, and some may have the same value due to symmetry. For a polycrystalline ferromagnetic material with x_3 chosen as the direction of magneetic and mechanical bias, equation A.17 turn out to be:

$$\begin{bmatrix} S_1 \\ S_2 \\ S_3 \\ S_4 \\ S_5 \\ S_6 \end{bmatrix} = \begin{bmatrix} S_{11}^H & S_{12}^H & S_{13}^H & 0 & 0 & 0 \\ S_{12}^H & S_{11}^H & S_{13}^H & 0 & 0 & 0 \\ S_{13}^H & S_{13}^H & S_{13}^H & 0 & 0 & 0 \\ 0 & 0 & 0 & S_{44}^H & 0 & 0 \\ 0 & 0 & 0 & 0 & S_{44}^H & 0 \\ 0 & 0 & 0 & 0 & 0 & S_{66}^H \end{bmatrix} \cdot \begin{bmatrix} T_1 \\ T_2 \\ T_3 \\ T_4 \\ T_5 \\ T_6 \end{bmatrix} + \begin{bmatrix} 0 & 0 & d_{31} \\ 0 & 0 & d_{31} \\ 0 & 0 & d_{33} \\ 0 & d_{15} & 0 \\ d_{15} & 0 & 0 \\ 0 & 0 & 0 \end{bmatrix} \cdot \begin{bmatrix} H_1 \\ H_2 \\ H_3 \end{bmatrix} \tag{A.18}$$

$$\begin{bmatrix} B_1 \\ B_2 \\ B_3 \end{bmatrix} = \begin{bmatrix} 0 & 0 & 0 & 0 & d_{15} & 0 \\ 0 & 0 & 0 & d_{15} & 0 & 0 \\ d_{31} & d_{31} & d_{33} & 0 & 0 & 0 \end{bmatrix} \cdot \begin{bmatrix} T_1 \\ T_2 \\ T_3 \\ T_4 \\ T_5 \\ T_6 \end{bmatrix} + \begin{bmatrix} \mu_{11}^T & 0 & 0 \\ 0 & \mu_{11}^T & 0 \\ 0 & 0 & \mu_{33}^T \end{bmatrix} \cdot \begin{bmatrix} H_1 \\ H_2 \\ H_3 \end{bmatrix} \tag{A.19}$$

Assumimng linear relationship between $\vec{B}$ and $\vec{H}$ and between $\vec{S}$ and $\vec{T}$ gives the internal nergy as:

$$U = \frac{1}{2} S_i T_i + \frac{1}{2} H_m B_m \tag{A.20}$$

If we now substitute S_i adn B_m by equation A.17, equation A.20 becames:

$$U = \underbrace{\frac{1}{2}T_i s_{ij} T_j}_{U_e} + \underbrace{\frac{1}{2}T_i d_{mi} H_m}_{U_me} + \underbrace{\frac{1}{2}H_m d_{mi} T_i}_{U_em} + \underbrace{\frac{1}{2}H_m \mu_{mk} H_k}_{U_m} \rightarrow \\ U_e + 2U_me + U_M \tag{A.21}$$

where U_e is the pure elastic energy, $U_{me} = U_{em}$ is the mutual magnetoelastic energy and U_m is the pure magnetic energy.

One important single figure of merit for magnetostrictive materials is the magnetomechanical coupling coefficient K, which is defined as the ratio of magnetelastic energy to the geometry mean of the elastic and magnetic energy:

$$K = \frac{U_{me}}{\sqrt{U_e U_m}} \tag{A.22}$$

In cases in which the applied magnetic field and the stress have components only in the direction of x_3, we would obtain that $H_1 = H_2 = 0$ while $H_3 \neq 0$ and $T_1 = T_2 = 0$ while only $T_3 \neq 0$. So, $B_1 = B_2 = 0$ while $B_3 \neq 0$ and $S_4 = S_5 = S_6 = 0$ with only $S_3 \neq 0$ (to be noted that also S_1 and S_2 are not zero, but thy can neglected since $T_1 = T_2 = 0 \rightarrow S_1 T_1 = S_2 T_2 = 0$).

So, the magnetomechanical coupling coefficent K can be written as:

$$K_{33}^2 = \frac{d_{33}^2}{\mu_{33}^T s_{33}^H} \tag{A.23}$$

Longitudinal Coupling In the case of operating magnetostrictive materials longitudinal, the constitutive linearized equations A.15 appear as follows:

$$\begin{cases} S = s^H T + dH \\ B = dT + \mu^T H \end{cases} \tag{A.24}$$

where the subscript 33 is omitted for simplicity. Is it possible to express the elastic compliance as function of B instead of H and the magnetic permeability as a function of S instead of T:

$$\begin{aligned} s^B &= \left.\frac{dS}{dT}\right|_B = s^H \left(1 - \frac{d^2}{s^H \mu^T}\right) = s^H \left(1 - k^2\right) \\ \mu^S &= \left.\frac{dB}{dH}\right|_S = \mu^T \left(1 - \frac{d^2}{s^H \mu^T}\right) = \mu^T \left(1 - k^2\right) \end{aligned} \tag{A.25}$$

Division of equation A.25 gives:

$$\mu^S s^H = \mu^T s^B = \lambda \tag{A.26}$$

where λ is the classical magnetostrictive constant. Using the transformation expressed in equation A.25, equation A.24 becames:

$$\begin{cases} S = s^B T + \frac{d}{\mu^T} B \\ B = \frac{d}{s^H} S + \mu^S H \end{cases} \tag{A.27}$$

Starting from equation A.27 we want to obtain the constitutive magnetostrictive equations. First of all we obtain:

$$\begin{cases} S = s^B T + \frac{d}{\mu^T} B \\ B = \frac{d}{s^H} S + \mu^S H \end{cases} \quad \rightarrow \begin{cases} T = \frac{1}{s^B} S - \frac{d}{\mu^T s^B} B \\ H = \frac{1}{\mu^S} B - \frac{d}{s^H \mu^S} S + \mu^S H \end{cases} \tag{A.28}$$

and finally:

$$\begin{cases} T = \frac{1}{s^B} S - \lambda B \\ H = -\lambda S + \nu^S B \end{cases} \tag{A.29}$$

where $\nu^s = \frac{1}{\mu^S}$.
The ratio of the cross-product of the coefficients now gives:

$$\lambda^2 \mu^s s^B = \frac{d^2}{\mu^T \mu^S s^B s^H} \mu^S s^B = \frac{d^2}{\mu^T s^H} = k^2 \tag{A.30}$$

Equation A.30 can be also written as:

$$\lambda d = \frac{k^2}{(1-k^2)} \qquad \text{or} \qquad k^2 = \frac{\lambda d}{1+\lambda d} \tag{A.31}$$

Bibliography

[1] L. Steve. *Big Data's impact in the World*. Feb. 2012.

[2] J. G. Haidar and J. I. Ghojel. "Waste heat recovery from the exhaust of low-power diesel engine using thermoelectric generators". In: *Proceedings ICT2001. 20 International Conference on Thermoelectrics (Cat. No.01TH8589)*. 2001, pp. 413–418.

[3] Chongfeng Wei and Xingjian Jing". "A comprehensive review on vibration energy harvesting: Modelling and realization". In: *Renewable and Sustainable Energy Reviews* 74 (2017), pp. 1–18. ISSN: 1364-0321. DOI: `https://doi.org/10.1016/j.rser.2017.01.073`. URL: `http://www.sciencedirect.com/science/article/pii/S1364032117300837`.

[4] L. Wang and F. G. Yuan. "Vibration energy harvesting by magnetostrictive material". In: *Smart Materials and Structures* 17 (2008), p. 045009.

[5] S. Boisseau, G. Despesse, and B. Ahmed Seddik. *Electrostatic Conversion for Vibration Energy Harvesting*. Mickael Lallart, 2012. DOI: `DOI:10.5772/51360`.

[6] Z. Deng and M.J. Dapino. "Review of magnetostrictive vibration energy harvesters". In: *Smart Materials and Structures* 26.10 (Sept. 2017), pp. 1189–1206. DOI: `https://doi.org/10.1088/1361-665X/aa8347`.

[7] M. Baldauf et al. "Method for application specific electrodynamic harvester design". In: *Eighth International Multi-Conference on Systems, Signals Devices*. Mar. 2011, pp. 1–2. DOI: `10.1109/SSD.2011.5767444`.

[8] S. Bradai et al. "Nonlinear analysis of an electrodynamic broadband energy harvester". In: *The European Physical Journal Special Topics* 224.14 (Nov. 2015), pp. 2919–2927. ISSN: 1951-6401. DOI: `10.1140/epjst/e2015-02598-0`.

[9] S. Beeby and N. White. *Energy Harvesting for autonomous system*. Artech House, 2010, pp. 103–108. ISBN: 159693719X, 9781596937192.

[10] S. Roundy, P.K. Wright, and K. S. J. Pister. "Micro-Electrostatic Vibration-to-Electricity Converters". In: *International Mechanical Engineering Congress and Exposition*. 2002, pp. 17–22.

[11] V. Berbyuk. “Vibration energy harvesting using Galfenol-based transducer”. In: *Active and Passive Smart Structures and Integrated Systems*. Vol. 8688. SPIE, Apr. 2013, pp. 17–22. DOI: 10.1117/12.2009812.

[12] S. Priya and D. J. Inman. Springer-Verlag, 2009. DOI: DOI:10.5772/51360.

[13] S. Roundy. “On the effectiveness of vibration-based energy harvesting”. In: *Journal of Intelligent Material Systems and Structures* 16.10 (2005), pp. 809–823.

[14] A. Lundgren et al. “Magnetostrictive Electric Generator”. In: *IEEE Transactions On Magnetics* 29.6 (1993), pp. 3150–3152.

[15] E. C. Stoner and E. P. Wohlfarth. “A mechanism of magnetic hysteresis in heterogeneous alloys”. In: *Philosophical Transactions of the Royal Society of London A: Mathematical, Physical and Engineering Sciences* 240.826 (1948), pp. 599–642. DOI: https://doi.org/10.1098/rsta.1948.0007.

[16] G. Dewar. “Magnetostriction and Terfenol-D”. In: *Complex Mediums*. 2000.

[17] R. Kellogg and A. Flatau. “Experimental Investigation of Terfenol-D’s Elastic Modulus”. In: *Journal of Intelligent Material Systems and Structures* 19 (2008). DOI: 10.1177/1045389X07077854.

[18] E.A. Lindgren, S. Haroush, and J.C. Poret. “Development of Terfenol-D transducer material”. In: *Journal of Applied Physics* 83.11 (1998), pp. 7282–7284.

[19] J.B. Restorff, M. Wun-Fogle, and A.E. Clark. “Piezomagnetic properties, saturation magnetostriction, and Delta E effect in DyZn at 77 K”. In: *Journal of Applied Physics* 83.11 (1998), p. 7288.

[20] J.B. Restorff, M. Wun-Fogle, and A.E. Clark. “Temperature and stress dependences of the magnetostriction in ternary and quaternary Terfenol alloys”. In: *Journal of Applied Physics* 87.9 (2000), pp. 5786–5788.

[21] D. Davino, A. Giustiniani, and C. Visone. “The piezo-magnetic parameters of Terfenol-D: An experimental viewpoint”. In: *Physica B* 407 (2012), pp. 1427–1432.

[22] K. P. Mohanchandra et al. “Sputter deposited Terfenol-D thin films for multiferroic applications”. In: *AIP Advances* 5 (2015), p. 097119. DOI: 10.1063/1.4930602.

[23] L. Wang, B.-W. Wang, and Z.-H. Wang. “Magneto-thermo-mechanical characterization of giant magnetostrictive materials”. In: *Rare Metals* 32.5 (2013), pp. 486–489.

[24] J. Zhang et al. “Experimental Investigation of the Magnetoelectric Effect in NdFeB-Driven A-Line Shape Terfenol-D/PZT-5A Structures”. In: *Materials* 12 (2019), p. 1055. DOI: 10.3390/ma12071055.

[25] O. Bottauscio et al. “Modelling and experimental analysis of magnetostrictive devices: from the material characterisation to their dynamic behaviour”. In: *IEEE Transactions on Magnetics* 44 (2008), pp. 3009–3012.

[26] C. Visone D. Davino A. Giustiniani. “Capacitive Load Effects on a magnetostrictive Fully Coupled Energy Harvesting Device”. In: *IEEE Transactions On Magnetics* 45.10 (2009), pp. 4108–4111.

[27] W. Huang et al. “Dynamic strain model with eddy current effects for giant magnetostrictive transducer”. In: *IEEE Transactions on Magnetics* 43.4 (2007), pp. 1381–1384.

[28] P. G. Evans and M. J. Dapino. “Dynamic model for 3-D magnetostrictive transducers”. In: *IEEE Transactions on Magnetics* 47.1 (2011), pp. 221–230.

[29] O. Bottauscio, P. E. Roccato, and M. Zucca. “Modeling the dynamic behavior of magnetostrictive actuators”. In: *IEEE Transactions on Magnetics* 46.8 (2010), pp. 3022–3028.

[30] D. Davino et al. “Stress-Induced Eddy Currents in Magnetostrictive Energy Harvesting Device”. In: *IEEE Transactions on Magnetics* 48.1 (2012), pp. 18–25.

[31] M. B. Moffett et al. “Characterization of Terfenol-D for magnetostrictive transducers”. In: *The Journal of the Acoustical Society of America* 89.3 (1991).

[32] A.A. Adly et al. “Exploiting Magnetostrictive Materials for Vibration Energy Harvesting”. In: *Proceedings ICSV17, 17th International Congress on Sound and Vibration. Cairo, Egypt.* 2010.

[33] F. Stillesjo and G. Engdahl. “Performance studies of a magnetostrictive actuator with varying mechanical and magnetic bias levels by dynamic simulations”. In: *Journal de Physique IV* 8.PR2 (1998), pp. 771–775.

[34] X. Zhao and D. G. Lord. “Application of the Villari effect to electric power harvesting”. In: *Journal Of Applied Physics* 99 (2006), pp. 1–3.

[35] M. Zucca, A. Hadadian, and O. Bottauscio. “Quantities Affecting the Behavior of Vibrational Magnetostrictive Transducers”. In: *IEEE Transactions on Magnetics* 51.1 (Jan. 2015), pp. 1–4. ISSN: 0018-9464. DOI: `10.1109/TMAG.2014.2359248`.

[36] D. Davino et al. “Stress-induced eddy currents in magnetostrictive energy harvesting devices”. In: *IEEE Transactions on Magnets* 48.1 (Jan. 2012), pp. 18–25.

[37] M. Zucca et al. “A study on energy harvesting by amorphous strips”. In: *IEEE Transactions on Magnets* 50.11 (2014), p. 8002104.

[38] A.E. Clark. “Chapter 7 Magnetostrictive rare earth-Fe2 compounds”. In: vol. 1. Handbook of Ferromagnetic Materials. Elsevier, 1980, pp. 531–589. DOI: https://doi.org/10.1016/S1574-9304(05)80122-1. URL: http://www.sciencedirect.com/science/article/pii/S1574930405801221.

[39] R.A. Kellogg. “Development and Modeling of Iron-Gallium alloys”. PhD thesis. Iowa State University, Department of Engineering Mechanics, 2003.

[40] O. Kubaschewski. *IRON—Binary Phase Diagrams*. Springer-Verlag Berlin Heidelberg, 1982.

[41] B. D. Cullity. “Chapter 8 Magnetostriction and effects of stress”. In: Introduction to Magnetic Materials. Addison-Wesly Publishing Co.

[42] V. Berbyuk and J. Sodhani. “Towards modelling and design of magnetostrictive electric generators”. In: *Computers and Structures* 86 (2008), pp. 307–313.

[43] M.J. Sablik and D.C. Jiles. “Coupled magnetoelastic theory of magnetic and magnetostrictive hysteresis”. In: *IEEE Transactions on Magnetics* 29 (1993), pp. 2113–2123.

[44] F.T. Calkins, R.C. Smith, and A.B. Flatau. “Energy-based hysteresis model for magnetostrictive transducers”. In: *IEEE Transactions on Magnetics* 36 (2000), pp. 429–439.

[45] F.C. Graham et al. “Modeling of a Galfenol transducer using the bidirectionally coupled magnetoelastic model”. In: *Smart Materials and Structures* 18.10 (2009), p. 104013.

[46] Y. Tan, Z. Zhang, and J. Zu. “Generalized Dynamic Modeling of Iron-Gallium Alloy (Galfenol) for Transducers”. In: *Journal of Applied Mathematics and Physics* 3 (2015), pp. 980–988.

[47] T. Ueno, E. M. Summers, and T. Higuchi. “Smart Structures and Materials 2005: Active Materials: Behavior and Mechanics”. In: *Computers and Structures*. 2005, p. 200.

[48] J. B. Restorff et al. “Induced tetragonal magnetic anisotropy in stress annealed Galfenol alloys”. In: *IEEE Transactions on Magnetics* 42.10 (2006), pp. 3087–3089.

[49] S. Datta, J. Atulasimha, and A. B. Flatau. “Figures of merit of magnetostrictive single crystal iron–gallium alloys for actuator and sensor applications”. In: *Journal of Magnetism and Magnetic Materials* 321.24 (2009).

[50] J. Atulasimha and A. Flatau. “A review of magnetostrictive iron-gallium alloys”. In: *Smart Materials and Structures* 20.4 (2011), p. 043001.

[51] L. Weng et al. “Major and minor stress-magnetization loops in textured polycrystalline Fe81.6Ga18.4, Galfenol”. In: 113 (2013), p. 024508.

[52] L. Weng et al. “Relationships between magnetization and dynamic stress for Galfenol rod alloy and its application in force sensor”. In: *Journal of Applied Physics* 113 (2013), 17A917.

[53] Q. Zhang. “Experimental characterization of Galfenol (Fe-Ga) alloys”. MA thesis. Ohio State University, 2014.

[54] J. J. Scheidler et al. “Dynamic characterization of Galfenol”. In: *SPIE Conference Proceedings* 9432 (2015), 94320J.

[55] Y.Y. Lo, S.U. Jen, and L.W. Pai. “Temperature dependence of mechanical properties of the Fe81Ga19 (Galfenol) alloy”. In: *Journal of Physics D: Applied Physics* 49.14 (2016).

[56] T. Christen and M.W. Carlen. “Theory of Ragone plots”. In: *Journal of Power Sources* 91.2 (2000), pp. 210–215. DOI: `10.1016/S0378-7753(00)00474-2`.

[57] A. Pandolfo and A. Hollenkamp. “Carbon properties and their role in supercapacitors”. In: *Journal of Power Sources* 157.1 (2006), pp. 11–27. DOI: `10.1016/j.jpowsour.2006.02.065`.

[58] J. R. Miller and P. Simon. “Electrochemical capacitors for energy management”. In: *Science* 321.5889 (2008), pp. 651–652. DOI: `ttps://dx.doi.org/10.1126/science.1158736URL`.

[59] P. Sharma and T. Bhatti. “A review on electrochemical double-layer capacitors”. In: *Energy Conversion and Management* 51.12 (2010), pp. 2901–12. DOI: `http://dx.doi.org/10.1016/j`.

[60] A. González et al. “Review on supercapacitors: Technologies and materials”. In: *Renewable and Sustainable Energy Reviews* 58 (2016), pp. 1189–1206. DOI: `http://dx.doi.org/10.1016/j.rser.2015.12.249`.

[61] K. Naoi and P. Simon. “New materials and new configurations for advanced electrochemical capacitors.” In: *The Electrochemical Society Interface* 17.1 (2008), pp. 34–37.

[62] G. Wang, L. Zhang, and J. Zhang. “A review on electrochemical double-layer capacitors”. In: *Chemical Society Reviews* 41.2 (2012), pp. 797–828. DOI: `http://dx.doi.org/10.1039/c1cs15060j`.

[63] C.M. Chuang et al. “Effects of carbon nanotube grafting on the performance of electric double layer capacitors”. In: *Energy Fuels* 24.12 (2010), pp. 6476–82. DOI: `http://dx.doi.org/10.1021/ef101208x`.

[64] Z.Z. Zhu et al. “Fabrication and electrochemical characterization of polyaniline nanorods modified with sulfonated carbon nanotubes for supercapacitor applications”. In: *Electrochimica Acta* 56.3 (2011), pp. 1366–72. DOI: `http://dx.doi.org/10.1016/j.electacta.2010.10.070`.

[65] D. Cericola and R. Kotz. “Hybridization of rechargeable batteries and electrochemical capacitors: principles and limits”. In: *Electrochimica Acta* 72 (2012), pp. 1–17. DOI: `http://dx.doi.org/10.1016/j.electacta.2012.03.151`.

[66] P. Simon and A. Burke. “Fabrication and electrochemical characterization of polyaniline nanorods modified with sulfonated carbon nanotubes for supercapacitor applications”. In: *The Electrochemical Society Interface* 17.1 (2008), pp. 38–44. URL: `http://www.electrochem.org/dl/interface/spr/spr08/spr08_p38-43.pdfS`.

[67] C. Portet et al. “Modification of Al current collector surface by sol–gel deposit for carbon–carbon supercapacitor applications”. In: *Electrochimica Acta* 49.6 (2004), pp. 905–12. DOI: `http://dx.doi.org/10.1016/j.electacta.2003.09.043`.

[68] Y. Gogotsi Y and V. Presser. CRCPress, 2013.

[69] B.E. Conway BE and W.G. Pell. “Double-layer and pseudocapacitance types of electrochemical capacitors and their applications to the development of hybrid devices”. In: *Journal of Solid State Electrochemistry* 7.9 (2003), pp. 637–644. DOI: `http://dx.doi.org/10.1007/s10008-003-0395-7`.

[70] V. Augustyn, P. Simon, and B. Dunn. “Pseudocapacitive oxide materials for high-rate electrochemical energy storage”. In: *Energy and Environmental Science* 7.5 (2014), pp. 1597–614. DOI: `http://dx.doi.org/10.1039/C3EE44164D.`.

[71] W. S. Harris. “Stability of nonaqueous electrolytes for ambient temperature rechargeable lithium cells”. PhD thesis. Universty of California, Berkley, 1985.

[72] D. Deng et al. “Green energy storage materials: Nanostructured TiO2 and Sn-based anodes for lithium-ion batteries”. In: *Energy and Environmental Science* 2 (2009), pp. 818–837.

[73] M. Armand and J.M. Tarascon. “Building Better Batteries”. In: *Nature* 451 (2008), pp. 652–657.

[74] B. Scrosati and J. Garche. “Lithium Batteries: Status, Prospects and Future”. In: *Journal of Power Sources* 195 (2010), pp. 2419–2430.

[75] A. Yoshino, K. Sanechika, and T. Nakajima. “Secondary Battery”. Japanese Patent 989. 1985.

[76] J.M. Tarascon and M. Armand. “Issues and Challenges Facing Rechargeable Lithium Batteries”. In: *Nature* 414 (2001), pp. 359–367.

[77] E. C. Evarts. “Lithium Batteries: To the Limits of Lithium”. In: *Nature* 526 (2015), S93–S95.

[78] K. Brandt. “Historical development of secondary lithium batteries”. In: *Solid State Ionics* 69 (1994), pp. 173–183.

[79] “Foundations for the future”. In: *Nature Energy* 1.9 (Sept. 2016), pp. 2058–7546. DOI: 10.1038/nenergy.2016.147.

[80] J. Janek and W. G. Zeier. “A Solid Future for Battery Development”. In: *Nature Energy* 500 (2016), p. 16141.

[81] J. B. Goodenough and Y. Kim. “Challenges for Rechargeable Li Batteries”. In: *Chemistry of Materials* 22 (2010), pp. 587–603.

[82] Y. Zhang et al. “Composite Anode Material of Silicon/Graphite/Carbon Nanotubes for Li-Ion Batteries”. In: *Electrochimica Acta* 51 (2006), pp. 4994–5000.

[83] P. G. Bruce, B. Scrosati, and J.M. Tarascon. “Nanomaterials for Rechargeable Lithium Batteries”. In: *Angewandte Chemie International Edition* 47 (2008), pp. 2930–2946.

[84] A. S. Arico et al. “Nanostructured Materials for Advanced Energy Conversion and Storage Devices”. In: *Nature Materials* 4 (2005), pp. 366–377.

[85] M. N. Obrovac and V. L. Chevrier. “Alloy Negative Electrodes for Li-Ion Batteries”. In: *Chemical Reviews* 114 (2014), pp. 11444–11502.

[86] P. Poizot et al. “Nano-Sized Transition-Metal Oxides as Negative-Electrode Materials for Lithium-Ion Batteries”. In: *Nature* 407 (2000), pp. 496–499.

[87] V. Etacheri et al. “Challenges in the Development of Advanced Li-Ion Batteries: A Review”. In: *Energy and Environmental Science* 4 (2011), pp. 3243–3262.

[88] J.W. Choi and D. Aurbach. “Promise and Reality of Post-Lithium-Ion Batteries with High Energy Densities”. In: *Nature Reviews Materials* 1 (2016), p. 16013.

[89] Da Deng. “Li-ion batteries: basics, progress, and challenges”. In: *Energy Science and Engineering* 3.5 (2015). DOI: doi:10.1002/ese3.95.

[90] Y. J. Cho et al. “Nitrogen-Doped Graphitic Layers Deposited on Silicon Nanowires for Efficient Lithium-Ion Battery Anodes”. In: *Journal of Physical Chemistry C* 115 (2011), pp. 9451–9457.

[91] Y. P. Wu et al. “Nitrogen-Containing Polymeric Carbon as Anode Material for Lithium Ion Secondary Battery”. In: *Journal of Applied Polymer Science* 77 (2000), pp. 1735–1741.

[92] A. L. M. Reddy et al. “Synthesis of Nitrogen-Doped Graphene Films for Lithium Battery Application”. In: *ACS Nano* 4 (2010), pp. 6337–6342.

[93] D. Wei et al. “Synthesis of N-Doped Graphene by Chemical Vapor Deposition and Its Electrical Properties”. In: *Nano Letters* 9 (2009), pp. 1752–1758.

[94] S. Hussain et al. “Physical and Electrical Properties of Graphene Grown under Different Hydrogen Flow in Low Pressure Chemical Vapor Deposition”. In: *Nanoscale Research Letters* 9 (2014), p. 546.

[95] T. O. Wehling et al. “Molecular Doping of Graphene.” In: *Nano Letters* 8 (2008), pp. 173–177.

[96] D. W. Boukhvalov and M. I. Katsnelson. “Chemical Functionalization of Graphene with Defects”. In: *Nano Letters* 8 (2008), pp. 4374–4379.

[97] F. Banhart, J. Kotakoski, and A. V. Krasheninnikov. “Structural Defects in Graphene”. In: *ACS Nano* 5 (2011), pp. 26–41.

[98] K. S. Novoselov et al. “Electric Field in Atomically Thin Carbon Films”. In: *Science* 306 (2004), pp. 666–669.

[99] Y. Zhu et al. “Graphene and Graphene Oxide: Synthesis, Properties, and Applications”. In: *Advanced Materials* 22 (2010), pp. 3906–3924.

[100] M. J. Allen, V. C. Tung, and R. B. Kaner. “Honeycomb Carbon: A Review of Graphene.” In: *Chemical Reviews* 110 (2010), pp. 132–145.

[101] R. Raccichini et al. “The Role of Graphene for Electrochemical Energy Storage”. In: *Nature Materials* 14 (2015), pp. 271–279.

[102] X. Cai et al. “Graphene and Graphene-Based Composites as Li-Ion Battery Electrode Materials and Their Application in Full Cells”. In: *Journal of Materials Chemistry A* 5 (2017), pp. 15423–15446.

[103] W. Do Diamond. “Mass production of high quality graphene: An analysis of worldwide patents”. In: (2012). DOI: `https://www.nanowerk.com/spotlight/spotid=25744.php.`.

[104] F. Bonaccorso et al. “Graphene, Related Two-Dimensional Crystals, and Hybrid Systems for Energy Conversion and Storage”. In: *Science* 347 (2015), p. 1246501.

[105] D. G. Papageorgiou, I. A. Kinloch, and R. J. Young. “Mechanical Properties of Graphene and Graphene-Based Nanocomposites”. In: *Progress in Materials Science* 90 (2017), pp. 75–127.

[106] B. A. Boukamp. “All-Solid Lithium Electrodes with Mixed-Conductor Matrix”. In: *Journal of The Electrochemical Society* 128.4 (1981), p. 725.

[107] I. Levchenko et al. “Scalable Graphene Production: Perspectives and Challenges of Plasma Applications”. In: *Nanoscale* 8 (2016), pp. 10511–10527.

[108] F. Bonaccorso et al. “Production and processing of graphene and 2d crystals”. In: *Materials Today* 15 (2012), pp. 564–589.

[109] A. Tranchot et al. “Influence of the Si Particle Size on the Mechanical Stability of Si-Based Electrodes Evaluated by in-Operando Dilatometry and Acoustic Emission”. In: *Journal of Power Sources* 330 (2016), pp. 253–260.

[110] S. Mandayam et al. “A fast iterative finite element modelfor electrodynamic and magnetostrictive vibration adsorbers”. In: *IEEE Transactions on magnetics* 30 (1994), pp. 3300–3303.

[111] L. Gros et al. “Strong coupling magneto mechanical methods applied to model heavy magnetostrictive actuators”. In: *IEEE Transactions on magnetics* 34 (1998), pp. 3150–3153.

[112] A.G. Olabi and A. Grunwald. “Computation of magnetic field in an actuator”. In: *Simulation Modelling Practice and Theory* 16 (2008), pp. 1728–1736.

[113] F. Stillesjo, G. Engdahl, and A. Bergqvist. “A design technique for magnetostrictive actuators with laminated active materials”. In: *IEEE Transactions on magnetics* 32 (1998), pp. 2141–2143.

[114] M. Besbes, Z. Ren, and A. Razek. “A generalized finite element mode of magnetostriction phenomena”. In: *IEEE Transactions on magnetics* 37 (2001), pp. 3324–3328.

[115] J. L. Pèrez-Aparicio and H. Sosa. “A continuum three-dimensional, fully coupled, dynamic, non-linear finite element formulation for magnetostrictive materials”. In: *Smart Material and Structures* 13 (2004), pp. 493–502.

[116] D. Davino et al. “Rate-dependent losses modeling for magnetostrictive actuators”. In: *Journal of Magnetism and Magnetic Materials* 272.276 (2004), pp. 1781–1782.

[117] O. Bottauscio et al. “Dynamic modelling and experimental analysis of Terfenol-D rods for magnetostrictive actuator”. In: *Journal of Applied Physics* 103 (2008), pp. 121–123.

[118] M. Stuebner, J. Atulasimha, and R. C. Smith. “Quantification of hysteresis and nonlinear effects on the frequency response of ferroelectric and ferromagnetic materials”. In: *Smart Material and Structures* 18 (2009), p. 104019.

[119] M. Kaltenbacher, M. Meiler, and M. Ertl. “Physical modeling and numerical computation of magnetostriction”. In: *COMPEL: The Int. J. Comp. Math. in Electrical and Electronic Eng.* 28 (2009), pp. 819–832.

[120] O. Bottauscio et al. “Modeling and Experimental Analysis of Magnetostrictive Devices: From the Material Characterization to Their Dynamic Behavior”. In: *IEEE Transactions on magnetics* 44 (2008), pp. 3009–3012.

[121] M. Zucca and O. Bottauscio. “Hysteretic Modeling of Electrical Micro-Power Generators Based on Villari Effect”. In: *IEEE Transactions on Magnetics* 48.11 (Nov. 2012), pp. 3092–3095. ISSN: 0018-9464. DOI: `10.1109/TMAG.2012.2206373`.

[122] A.A. Adly, I.D. Mayergoyz, and A. Bergqvist. “Utilizing anisotropic Preisach-type models in the accurate simulation of magnetostriction”. In: *IEEE Transactions on magnetics* 33 (1997), pp. 3931–3933.

[123] M.J. Sablik and D.C. Jiles. “Coupled magnetoelastic theory of magnetic and magnetostrictive hysteresis”. In: *IEEE Transactions on magnetics* 29 (1993), pp. 2113–2123.

[124] F.T. Calkins, R.C. Smith, and A.B. Flatau. “Energy-based hysteresis model for magnetostrictive transducers”. In: *IEEE Transactions on magnetics* 36 (2000), pp. 429–439.

[125] L.A.L. Almeida, G.S. Deepcand A.M.N. Lima, and H. Neff. “Modeling a magnetostrictive transducer using genetic algorithm”. In: *Journal of Magnetism and Magnetic Materials* 266 (2001), pp. 1262–1264.

[126] S.C. Cao et al. “Modeling dynamic hysteresis for giant magnetostrictive actuator using hybrid genetic algorithm”. In: *IEEE Transactions on magnetics* 42 (2006), pp. 911–914.

[127] M. Zucca and O. Bottauscio. “Hysteretic Modeling of Electrical Micro-Power Generators Based on Villari Effect”. In: *IEEE Transactions on Magnetics* 48.11 (Nov. 2012), pp. 3092–3095. ISSN: 0018-9464. DOI: `10.1109/TMAG.2012.2206373`.

[128] G. Kadar. “On the Preisach function of ferromagnetic hysteresis”. In: *Journal of Applied Physics* 61 (1987), pp. 4013–4015.

[129] S. Palumbo et al. “Dynamic Simulation of a Fe-Ga Energy Harvester Prototype Through a Preisach-Type Hysteresis Model”. In: *Materials* 12.3384 (2019). DOI: `10.3390/ma12203384`.

[130] S. Palumbo, P. Rasilo, and M. Zucca. “Experimental investigation on a Fe-Ga close yoke vibrational harvester by matching magnetic and mechanical biases”. In: *Journal of Magnetism and Magnetic Materials* 469 (2019), pp. 354–363. DOI: `https://doi.org/10.1016/j.jmmm.2018.08.085`.

[131] U. Ahmed et al. “Finite element analysis of magnetostrictive energy harvesting concept device utilizing thermodynamic magneto-mechanical model”. In: *Journal of Magnetism and Magnetic Materials* 486 (2019). DOI: `https://doi.org/10.1016/j.jmmm.2019.165275`.

[132] M. Zucca et al. “Sensing Dynamic Forces by Fe–Ga in Compression”. In: *IEEE Transactions on Magnetics* 53.11 (2017). DOI: `DOI:10.1109/TMAG.2017.2701859`.

[133] ISO 7500-1:2016. "Metallic materials – Verification of static uniaxial testing machines". In: (2016).

[134] UNI EN ISO 376. "Metallic materials – Calibration of force-proving instruments used for the verification of uniaxial testing machines". In: (2011).

[135] S. W. Lee et al. "Anomalous shape changes of silicon nanopillars by electrochemical lithiation." In: *Nano Letters* 11.7 (2011), pp. 3034–3039. DOI: 10.1021/nl201787r.

[136] M. N. Obrovac and V. L. Chevrier. "Alloy Negative Electrodes for Li-Ion Batteries". In: *Chemical Reviews. American Chemical Society* 10 (2014), pp. 11444–11502.

[137] W. Li, X. Sun, and Y. Yu. "Si-, Ge-, Sn-Based Anode Materials for Lithium-Ion Batteries: From Structure Design to Electrochemical Performance". In: *Small Methods* 1.3 (2017), p. 1600037.

[138] A. Casimir et al. "Silicon-Based Anodes for Lithium-Ion Batteries: Effectiveness of Materials Synthesis and Electrode Preparation". In: *Nano Energy* (2016), pp. 359–376.

[139] B. Liang, Y. Liu, and Y. Xu. "Silicon-Based Materials as High Capacity Anodes for next Generation Lithium Ion Batteries". In: *Journal of Power Sources* (2014), pp. 469–490.

[140] M .Winter and J. O. Besenhard. "Electrochemical Lithiation of Tin and Tin-Based Intermetallics and Composites". In: *Electrochimica Acta* 45.1 (1999), pp. 31–50.

[141] M. Winter et al. "Insertion Electrode Materials for Rechargeable Lithium Batteries". In: *Advanced Materials* 01.10 (1998), pp. 725–763.

[142] M. T. McDowell et al. "25th Anniversary Article: Understanding the Lithiation of Silicon and Other Alloying Anodes for Lithium-Ion Batteries". In: *Advanced Materials* (2013), pp. 4966–4985.

[143] A. N. Dey. "Electrochemical Alloying of Lithium in Organic Electrolytes". In: *Journal of The Electrochemical Society* 118.10 (1971), p. 1547.

[144] W. Wan and Q. Zhang. "First principles study of lithium insertion in bulk silicon". In: *Journal of Physics: Condensed Matter* 9.22 (2010).

[145] J. Yang. "Small Particle Size Multiphase Li-Alloy Anodes for Lithium-Ion batteries". In: *Solid State Ionics* 90 (1996), pp. 281–287.

[146] P. Limthongkul et al. "Electrochemically-driven solid-state amorphization in lithium-metal anodes". In: *Journal of Power Sources* 119.121 (2003), pp. 604–609. DOI: https://doi.org/10.1016/S0378-7753(03)00303-3.

[147] X. H. Liu et al. "Size-Dependent Fracture of Silicon Nanoparticles during Lithiation". In: *ACS Nano* 6 (2012), pp. 1522–1531.

[148] T. Schott et al. “Cycling Behavior of Silicon-Containing Graphite Electrodes, Part B: Effect of the Silicon Source”. In: *Journal of Physical Chemistry C* 121 (2017), pp. 25718–25728.

[149] Y. Kwon et al. “Sn0.9Si0.1/Carbon Core-Shell Nanoparticles for High-Density Lithium Storage Materials”. In: *Chemistry of Materials* 19 (2007), pp. 982–986.

[150] Y. Kwon and J. Cho. “High Capacity Carbon-Coated Si70Sn30 Nanoalloys for Lithium Battery Anode Material”. In: *Chemical Communications* (2008), pp. 1109–1111.

[151] K. Peng et al. “Silicon Nanowires for Rechargeable Lithium-Ion Battery Anodes.” In: *Applied Physics Letters* 93 (2008), p. 033105.

[152] H. Wu et al. “Stable Cycling of Double-Walled Silicon Nanotube Battery Anodes through Solid-Electrolyte Interphase Control”. In: *Nature Nanotechnology* 7 (2012), pp. 310–315.

[153] C. K. Chan et al. “High-performance lithium battery anodes using silicon nanowires.” In: *Nature Nanotechnology* 3 (2008), pp. 31–35.

[154] T. D. Bogart et al. “Lithium Ion Battery Peformance of Silicon Nanowires with Carbon Skin”. In: *ACS Nano* 8 (2013), pp. 915–922.

[155] N. Dimov, S. Kugino, and M. Yoshio. “Carbon-Coated Silicon as Anode Material for Lithium Ion Batteries: Advantages and Limitations”. In: *Electrochimica Acta* 48 (2003), pp. 1579–1587.

[156] H. Y. Lee and S. M. Lee. “Carbon-Coated Nano-Si Dispersed Oxides/Graphite Composites as Anode Material for Lithium Ion Batteries”. In: *Electrochemistry Communications* 6 (2004), pp. 465–469.

[157] J. K. Lee et al. “Rational Design of Silicon-Based Composites for High-Energy Storage Devices”. In: *Journal of Materials Chemistry A* 4 (2016), pp. 5366–5384.

[158] B. Hertzberg, A. Alexeev, and G. Yushin. “Deformations in Si-Li Anodes upon Electrochemical Alloying in Nano-Confined Space.” In: *American Chemical Society* 132 (2010), pp. 8548–8549.

[159] E. Quesnel et al. “Graphene-Based Technologies for Energy Applications, Challenges and Perspectives.” In: *2D Materials* 2 (2015), p. 030204.

[160] M. Zhang et al. “Latest Development of Nanostructured Si/C Materials for Lithium Anode Studies and Applications”. In: *Energy Storage Materials* 4 (2016), pp. 1–14.

[161] P. T. Araujo, M. Terrones, and M. S. Dresselhaus. “Defects and Impurities in Graphene-like Materials”. In: *Materials Today* 15 (2012), pp. 98–109.

[162] K. Chen et al. “Structural Design of Graphene for Use in Electrochemical Energy Storage Devices”. In: *Chemical Society Reviews* 44 (2015), pp. 6230–6257.

[163] L. Ji et al. “Graphene-Based Nanocomposites for Energy Storage”. In: *Advanced Energy Materials* 6 (2016), p. 1502159.

[164] C. Xu et al. “Graphene-Based Electrodes for Electrochemical Energy Storage”. In: *Energy and Environmental Science* 6.5 (2013), p. 388.

[165] W. Lv et al. “Graphene-Based Materials for Electrochemical Energy Storage Devices: Opportunities and Challenges”. In: *Energy Storage Materials* 2 (2016), pp. 107–138.

[166] Y. Yang et al. “Graphene-Based Materials with Tailored Nanostructures for Energy Conversion and Storage”. In: *Materials Science and Engineering: R: Reports* 102 (2016), pp. 1–72.

[167] S. Wu et al. “Graphene-Containing Nanomaterials for Lithium-Ion Batteries”. In: *Advanced Energy Materials* 5 (2015), pp. 1–40.

[168] F. Bonaccorso et al. “2DCrystal-Based Functional Inks”. In: *Advanced Materials* 28 (2016), pp. 6136–6166.

[169] D. Ji et al. “Effect of Si Content on Structure and Electrochemical Performance of Ternary Nanohybrids Integrating Si Nanoparticles, N-Doped Carbon Shell, and Nitrogen-Doped Graphene”. In: *RSC Advances* 7 (2017), pp. 4209–4215.

[170] Y. Wu, S. Fang, and Y. Jiang. “Effects of Nitrogen on the Carbon Anode of a Lithium Secondary Battery”. In: *Solid State Ionics* 120 (1999), pp. 117–123.

[171] H. Wang et al. “Nitrogen-Doped Graphene Nanosheets with Excellent Lithium Storage Properties”. In: *Journal of Materials Chemistry* 21 (2011), pp. 5430–5434.

[172] J. Lin et al. “Pomegranate-Like Silicon/Nitrogen-Doped Graphene Microspheres as Superior-Capacity Anode for Lithium-Ion Batteries”. In: *Electrochimica Acta* 215 (2016), pp. 667–673.

[173] X. Tang et al. “Novel Silicon Nanoparticles with Nitrogen-Doped Carbon Shell Dispersed in Nitrogen-Doped Graphene and CNTs Hybrid Electrode for Lithium Ion Battery”. In: *Applied Surface Science* 425 (2017), pp. 742–749.

[174] X. Tang, G. Wen, and Y. Song. “Stable Silicon/3D Porous NDoped Graphene Composite for Lithium-Ion Battery Anodes with Self-Assembly”. In: *Applied Surface Science* 436 (2018), pp. 398–404.

[175] S. Suresh et al. “Protecting Silicon Film Anodes in Lithium-Ion Batteries Using an Atomically Thin Graphene Drape”. In: *ACS Nano* 11 (2017), pp. 5051–5061.

[176] X. Ding et al. “Enhanced Electrochemical Performance Promoted by Monolayer Graphene and Void Space in Silicon Composite Anode Materials”. In: *Nano Energy* 27 (2016), pp. 647–657.

[177] A. E. Del Rio Castillo et al. “High-Yield Production of 2D Crystals by Wet-Jet Milling.” In: *Materials Horizons* 5 (2018), pp. 890–904.

[178] E. Greco et al. “Few-Layer Graphene Improves Silicon Performance in Li-Ion Battery Anodes.” In: *Journal of Materials Chemistry A* 5 (2017), pp. 19306–19315.

[179] “NIST X-ray Photoelectron Spectroscopy Database v 4.1”. In: *National Institute of Standards and Technology, Gaithersburg* (2012). DOI: `http://srdata.nist.gov/xps/`.

[180] A. C. Ferrari and D. M. Basko. “Raman spectroscopy as a versatile tool for studying the properties of graphene”. In: *Nature Nanotechnology* 8 (2013), p. 235.

[181] S. Palumbo et al. “Silicon Few-Layer Graphene Nanocomposite as High-Capacity and High-Rate Anode in Lithium-Ion Batteries”. In: *ACS Applied Energy Materials* 2.3 (2019), pp. 1793–1802. DOI: `DOI:10.1021/acsaem.8b01927`.

[182] A. W. Coats and J. P. Redfern. “Thermogravimetric Analysis: A Review”. In: *Analyst* 88.1053 (1963), pp. 906–924. DOI: `10.1039/AN9638800906`.

[183] C.J. Wen et al. In: *Journal of The Electrochemical Society* 126 (179), p. 2258.

[184] A.H. Thompson. In: *Journal of The Electrochemical Society* 126 (1979), p. 608.

[185] B. Key et al. “Pair Distribution Function Analysis and Solid State NMR Studies of Silicon Electrodes for Lithium Ion Batteries: Understanding the (De)lithiation Mechanisms”. In: *Journal of the American Chemical Society* 133 (2010), pp. 503–512.

[186] K. Ogata et al. “Revealing lithium-silicide phase transformations in nano-structured silicon-based lithium ion batteries via in situ NMR spectroscopy”. In: *Nature Communications* 5 (2014), p. 3217.

[187] M. N. Obrovac and L. Christensen. “Structural Changes in Silicon Anodes during Lithium Insertion/Extraction”. In: *Electrochemical and Solid State Letters* 7 (204), A93.

[188] M. T. McDowell et al. “Studying the kinetics of crystalline silicon nanoparticle lithiation with in situ transmission electron microscopy”. In: *Advanced Materials* 24 (2012), pp. 6034–41.

[189] L. Y. Beaulieu et al. “Colossal Reversible Volume Changes in Lithium Alloys”. In: *Electrochemical and Solid State Letters* 4.9 (2001), A137.

[190] L. Y. Beaulieu et al. “Reaction of Li with Alloy Thin Films Studied by In Situ AFM”. In: *Journal of The Electrochemical Society* 150.11 (2003), A1457.

[191] M. N. Obrovac and L. Christensen. “Structural Changes in Silicon Anodes during Lithium Insertion/Extraction”. In: *Electrochemical and Solid State Letters* 7.5 (2004), A93.

[192] M. N. Obrovac and L. J. Krause. “Reversible Cycling of Crystalline Silicon Powder”. In: *Journal of The Electrochemical Society* 154.2 (2007), A103.

[193] C. Guo et al. “A SiO/graphene Nanocomposite as a High Stability Anode Material for Lithium-Ion Batteries”. In: *International Journal of Electrochemical Science* 7 (2012), pp. 8745–8752.

[194] G. Engdahl. *Handbook of Giant Magnetostrictive Materials.* Electromagnetism. Oxford: Academic Press, 2000, pp. 127–205.

[195] S. Butterworth and F. D. Smith. “The equivalent circuit of the magnetostriction oscillator”. In: *Proceedings of the Physical Society* 43.2 (1931), p. 166.

[196] J. F. Nye. *Physical Properties of Crystals.* Oxford University Press, 1957.

This Ph.D. thesis has been typeset by means of the TEX-system facilities. The typesetting engine was pdfLATEX. The document class was `toptesi`, by Claudio Beccari, with option `tipotesi=scudo`. This class is available in every up-to-date and complete TEX-system installation.